INFORMATION TO USERS

This manuscript has been reproduced from the microfilm master. UMI films the text directly from the original or copy submitted. Thus, some thesis and dissertation copies are in typewriter face, while others may be from any type of computer printer.

The quality of this reproduction is dependent upon the quality of the copy submitted. Broken or indistinct print, colored or poor quality illustrations and photographs, print bleedthrough, substandard margins, and improper alignment can adversely affect reproduction.

In the unlikely event that the author did not send UMI a complete manuscript and there are missing pages, these will be noted. Also, if unauthorized copyright material had to be removed, a note will indicate the deletion.

Oversize materials (e.g., maps, drawings, charts) are reproduced by sectioning the original, beginning at the upper left-hand corner and continuing from left to right in equal sections with small overlaps. Each original is also photographed in one exposure and is included in reduced form at the back of the book.

Photographs included in the original manuscript have been reproduced xerographically in this copy. Higher quality 6" x 9" black and white photographic prints are available for any photographs or illustrations appearing in this copy for an additional charge. Contact UMI directly to order.

UMI®

Bell & Howell Information and Learning
300 North Zeeb Road, Ann Arbor, MI 48106-1346 USA
800-521-0600

NMR STUDIES OF RAT LIVER FATTY ACID-BINDING PROTEIN (LFABP)

by

YAN HE

A dissertation submitted to the Graduate Faculty in Chemistry in partial fulfillment of the requirements for the degree of Doctor of Philosophy, The City University of New York.

2000

This manuscript has been read and accepted for the Graduate Faculty in Chemistry in satisfaction of the dissertation requirement for the degree of Doctor of Philosophy.

6/18/00
Date

(signature) Ruth E. Stark
Chair of Examining Committee

6/21/2000
Date

(signature) Gerald Koser
Executive Officer

Fred Naider

William J. Freeney

Hsin Wang
Supervisory Committee

THE CITY UNIVERSITY OF NEW YORK

ABSTRACT

NMR STUDIES OF RAT LIVER FATTY ACID-BINDING PROTEIN (LFABP)

by

YAN HE

Advisor: Professor Ruth E. Stark

Rat liver fatty acid-binding protein (LFABP) exhibits unique properties compared with other FABPs: it binds diverse ligands; has more than one binding site; and transfers fatty acids to membranes via aqueous diffusion rather than via direct collisional interactions. This work seeks to understand the protein functions through a study of its solution-state molecular structure and dynamics.

Sequence-specific ^{1}H, ^{13}C, and ^{15}N resonance assignments were established for apo and oleate-bound holo-LFABP using multidimensional triple-resonance nuclear magnetic resonance (NMR) methods. Its secondary structural elements were determined from the consensus $^{1}H/^{13}C$ chemical shift indices. The tertiary structure of oleate-bound holo-LFABP was calculated based on 2421 unique NMR distance constraints, yielding a family of 20 optimized structures with an average backbone RMSD of 1.05 Å. The LFABP conformation consists of 10 antiparallel β-strands that form two nearly orthogonal β-sheets of five strands each, and two short α-helices that connect β-strands A and B. The NMR solution structure agrees substantially with the 2.3Å X-ray crystal structure.

An oleate titration of ^{15}N-LFABP, monitored by amide chemical shifts and linewidths in ^{1}H-^{15}N correlation spectra, was used to locate changes in protein structure

that accompany the addition of each oleate molecule. At least two oleates (or palmitates) were bound within the LFABP cavity, based on the observation of two sets of ω-CH_3 and α-CH_2 peaks in ^{1}H-^{13}C correlation spectra. The observation of significant linewidth differences between the spectra of holo-LFABPs with two and three equivalents of fatty acid suggested that a third oleate may also be bound to the periphery of LFABP.

H_2O/D_2O exchange was carried out to evaluate the solvent accessibility of apo- and holo-LFABP, revealing more extensive hydrogen bonding with ligand present. The backbone dynamics of apo- and oleate-bound holo-LFABP were compared using amide ^{15}N relaxation measurements, the *Modelfree* program was used to deduce dynamic parameters in holo-LFABP. Shorter relaxation rates, higher order parameters, and reduced solvent accessibility were found in the holo-protein, indicating less flexibility, more order, and a more stable hydrogen-bonding network than the apo-protein.

ACKNOWLEDGEMENTS

I would like to express my sincere gratitude to my mentor, Prof. Ruth E. Stark, who gave me the wonderful opportunity to be involved in the field of protein structure determination by NMR and guided me patiently in my every growth step.

I would like to extend my thanks to Dr. Hsin Wang, who brought me to the entrance of the NMR field and always gave me every detailed help.

I thank all my committee members, Prof. Fred Naider and Prof. William Sweeney, for their sound advice and strong support.

I would like to give my special thanks to: Prof. Judith Storch and her group, for their kind contribution of the protein samples; and Prof. Arthur G. Palmer and his graduate student, Mr. Christopher D. Kroenke, for their great help in the dynamics calculation.

Finally, I thank Lewis Kay for his pulse programs, Frank Delaglio for NMRPipe, Bruce Johnson for NMRView, Peter Güntert for DYANA, Reto Koradi in Kurt Wüthrich's group for MOLMOL, Tripos Company for SYBYL, and Arthur Palmer for *Modelfree*.

With my special love to:

My husband, Shu-Ren Ma

My son, Yue Ma

My mother, Lian-Ying Xu

My sister, Hong He, and her family

In loving memory of my father

Contents of Text

List of Figures

List of Tables

CHAPTER 1

INTRODUCTION

1.1 What Are Fatty Acid-Binding Proteins (FABPs)?

Cytosolic fatty acid-binding proteins (FABPs) belong to a gene family of which eight members have been conclusively identified. They have been isolated from intestine, liver, heart, adipose tissue, myelin, brain, muscle, and epidermis, respectively. These 14-15 kDa proteins are abundantly expressed in a highly tissue-specific manner that is essential to lipid metabolism. In these tissues FABPs constitute between 2 and 5% of soluble proteins, with estimated cellular concentrations in the 0.2-0.4 mM range[1]. FABPs are thought to enhance the transfer of long-chain fatty acid (FA) between artificial and native lipid membranes, and also to have a stimulatory effect on a number of enzymes that control FA metabolism *in vitro*. The amino acid sequence of rat liver FABP is only 22-27% homologous with FABPs from heart, adipose tissue and myelin sheath, whereas these other proteins are 60-65% homologous with each other. The intestinal FABP is 29% homologous to liver FABP and 30-33% homologous to the above three FABPs.

FABPs bind a variety of hydrophobic and amphipathic ligands with varying degrees of affinity. The differences that exist in the primary structures of the FABPs could account for the different binding properties exhibited among the members of the gene family. Recent crystallographic evidence, on the other hand, suggests that in spite of disparate primary sequences, the tertiary structures of FABPs exhibit overall similarity and a "clam shell-like" configuration, with two parallel β-sheets orthogonally oriented to

each other and with the hydrophobic ligand bound within a pocket formed by the β-clam[2,3].

1.2 Application of Multidimensional NMR Techniques to Proteins[4-7]

Nuclear magnetic resonance (NMR) spectroscopy is based on the fact that atomic nuclei oriented by a strong magnetic field (2-18 Tesla) absorb radiation at characteristic frequencies (typically a few hundred megahertz, in the radiofrequency part of the spectrum). The fact that nuclei of the same element in different environments give rise to distinct spectral lines makes it possible to observe signals from individual atoms even for complex biological macromolecules in solution. The parameters that can be measured from the resulting spectra can be interpreted in terms of molecular structure, conformation, and dynamics.

The first published NMR spectrum of a biological macromolecule, consisting of four broad peaks, was the 40 MHz ^{1}H spectrum of pancreatic ribonuclease reported in 1957[8]. Soon thereafter, Jardetzky *et al.* analyzed the intensity of each peak in this low resolution spectrum and concluded that the most that could be deduced was that the spectrum was consistent with the amino acid composition of the protein[9,10]. In subsequent years, the power of NMR instrumentation and methodology has increased dramatically, notably in its application to studies of the conformations and interactions of biological macromolecules. The majority of modern applications of NMR to the study of biological macromolecules involve the analysis of two-, three-, or even four- dimensional NMR spectra. The assignment of resonance to individual nuclei is an essential first step in any NMR study, and this has been made very much easier with the advent of

multidimensional NMR experiments. The structural information is then obtained principally from measurements of the nuclear Overhauser effect (NOE), which provide constraints on internuclear distances.

To extend the usefulness of NMR to larger molecules, the most powerful approach is isotope labeling with ^{13}C and ^{15}N in conjunction with three- and four-dimensional (3D and 4D) NMR experiments. In 3D and 4D NMR the two-dimensional ^{1}H spectra are, in effect, "spread out" in a third or fourth dimension by the ^{13}C or/and ^{15}N chemical shift. Individual "slices" at a particular ^{13}C or ^{15}N chemical shift are thus much less crowded and easier to analyze. The combination of isotope labeling and multidimensional NMR has been used for the determination of three-dimensional structures of proteins of around 170 residues, and extended in favorable cases up to 300 residues.

NMR spectroscopy (in solution) and X-ray crystallography (in the solid state) are currently the only techniques capable of determining the three-dimensional structures of macromolecules at atomic resolution. In addition, NMR spectroscopy is a powerful technique for investigating time-dependent phenomena. NMR can provide valuable information on local structure, on conformational dynamics, and on both structural and kinetic aspects of interactions with small molecules. NMR can be used to characterize the charge site, conformation, binding site, and dissociation rates of bound ligands, and to identify contacts between individual atoms of the ligand and individual atoms of the protein. Most importantly, NMR can be applied to molecules for which no single crystals are available.

1.3 Why Study Rat Liver Fatty Acid-Binding Protein (LFABP)?

LFABP, which is expressed at high levels in both intestinal absorptive cells and liver hepatocytes, is particularly important for dealing with increased levels of fatty-acid flux that may occur in the enterocyte on high fat diets or, in the hepatocyte, during starvation or uncontrolled diabetes. The reason we study LFABP is due to its unique functional properties:

Firstly, LFABP binds diverse ligands relative to other FABPs. LFABP binds fatty acids and a number of endogenous hydrophobic ligands such as lysophospholipids, bile salts and monoacylglycerol[11,12], whereas other FABPs appear to have high-affinity binding for long-chain FA only[13].

Secondly, LFABP has more than one binding site. LFABP possesses a very hydrophobic binding site compared with the other FABPs[14]. It has been reported variously that LFABP may have one, two or even three FA binding sites[15,16], whereas all other FABPs have been found to possess a single binding site for long-chain FA[17].

Thirdly, LFABP has unique FA transport properties compared with other FABPs. Fatty acid transfer from LFABP occurs at a slower rate than that from intestinal FABP, heart FABP or adipocyte FABP, respectively. Moreover, transfer of FA's from the adipocyte, heart and intestinal FABPs to the vesicles appears to occur via direct collisional interactions between the FABPs and the "acceptor" bilayer[18,19]. However, FA transfer from LFABP to vesicles occurs via aqueous diffusion, with the dissociation of the FA from the protein-binding site into the aqueous milieu as the rate-determining step[20].

In order to understand these unusual functional properties, molecular-level structural and dynamic information is essential. High-resolution tertiary structures have been obtained for several FABPs in apo and holo forms by X-ray crystallography, and more recently by NMR spectroscopy. For instance, one or both forms have been examined for IFABP (intestine FABP)[3,21,22], CRBPII (cellular retinoic acid-binding protein)[23] and HFABP (heart FABP)[24]. The X-ray structure of oleate-bound holo-LFABP has been reported[25], but the tertiary structure of apo-LFABP has remained unsolved because LFABP does not form suitable crystals. Molecular dynamics studied by NMR have offered time-dependent structural information on proteins, permitted identification of the binding site through changes in flexibility and order upon ligation, and probed motions on a time scale ranging from ps to ms[26] that are likely to be functionally significant. For instance, the dynamics of palmitate complexed with rat IFABP have been reported[27,28] to implicate a mechanism of ligand entry.

The goal of this study, therefore, is to apply high resolution multidimensional solution NMR techniques on rat LFABP to: (1) make complete ^{1}H, ^{15}N, and ^{13}C resonance assignments on both apo- and holo-LFABP and derive their secondary structures based on the sequential assignments; (2) determine the tertiary structure of holo- and apo-LFABP based on NOE constraints and derived secondary structural elements; (3) analyze the stoichiometry of fatty-acid binding to the protein by titration and explore the binding site(s) of the protein-ligand interaction; and (4) develop an understanding of the dynamics of the protein by H/D exchange and ^{15}N relaxation studies.

CHAPTER 2

NMR ASSIGNMENTS OF APO-LFABP

[Published in modified form as Wang, H.; He, Y.; Hsu, K. T.; Magliocca, J. F.; Storch, J.; Stark, R. E. *J. Biomolecular NMR* **1998**, *12*, 197-199.]

2.1 Introduction

LFABP is composed of 127 amino acid residues. The primary structure, i.e., amino acid sequence of LFABP, is known from cloned cDNA sequences. The single-letter sequence of LFABP is listed below.

MNFSGKYQVQ SQENFEPFMK AMGLPEDLIQ KGKDIKGVSE
IVHEGKKVKL TITYGSKVIH NEFTLGEECE LETMTGEKVK
AVVKMEGDNK MVTTFKGIKS VTEFNGDTIT NTMTLGDIVY
KRVSKRI

In order to define the three-dimensional structure of a protein or determine how it interacts with ligands, it is first necessary to assign as many of its NMR resonances as possible to specific nuclei of individual amino acid residues. NMR resonance assignment is facilitated by isotopic labeling of the protein with NMR active heteronuclei (^{13}C, ^{15}N, and ^{2}H) and by the use of multinuclear 3D and 4D experiments. Once the sequence-specific assignments are made, the secondary structural elements can be derived and further the tertiary structure can be determined.

2.2 Sample Preparation

All apo forms of ^{15}N-labeled and $^{13}C/^{15}N$-labeled LFABP samples were provided through a collaborative arrangement with Prof. Judith Storch's group (Rutgers

University, NJ). The procedures of protein purification and isotopic labeling were as follows. Rat liver FABP cDNA subcloned into the pET-11d expression vector (Novagen, Madison, WI) using the *Nco*I-*Eco*RI restriction sites was generously provided by Drs. Alan Kleinfeld and Ron Ogata (Medical Biology Institute, La Jolla, CA). *E. coli* host strain BL21(DE3)pLysS was transformed and protein expression induced by addition of 0.5 mM IPTG to the growing culture at 37 °C. The cells were harvested after 3 h, resuspended in pH 8.3 Tris buffer, and sonicated to release soluble proteins; the LFABP was purified and delipidated[18,29] and stored at 4 °C. A similar procedure was used for the growth and expression of LFABP on M9 minimal media consisting of glucose and ammonium chloride as the sole carbon and nitrogen sources; $[^{15}N]H_4Cl$ and $[U\text{-}^{13}C_6]$-glucose (both from Isotec, Miamisburg, OH) were used to produce uniformly ^{15}N- and $^{13}C/^{15}N$-enriched protein samples. Typical protein yields from minimal media were 10-15 mg per liter of culture. Gel filtration was used to verify that LFABP was present in monomeric form at concentrations up to 2.0 mM at pH 6.5. Protein purity (>98%) was verified by methods of SDS polyacrylamide gel electrophoresis (15%) and Coomassie staining[18].

For NMR studies, the protein solutions were dialyzed against a 50 mM pH 6.0 phosphate buffer containing 100 mM sodium chloride, 50 μM EDTA, and 0.02% sodium azide, and then concentrated with an Amicon ultrafiltration system (Beverly, MA). The final LFABP concentrations for making resonance assignments of apo-LFABP were 1.3 mM for the dual-labeled sample and 1.0 mM for the ^{15}N-labeled sample, respectively, as determined by a Lowry protein assay[30,31]. After addition of 5% D_2O by volume (Isotec,

Miamisburg, OH), the solutions were transferred to 5-mm Shigemi NMR tubes (Shigemi, Allison Park, PA), and stored at 4 °C until use.

2.3 NMR Experiments

2.3.1 NMR spectroscopy and chemical-shift references

All the NMR experiments on apo-LFABP were carried out at pH 6.0 and 30 °C on a three-channel Varian Unity*plus*-600 spectrometer (Varian NMR Instruments, Palo Alto, CA) equipped with a pulsed-field-gradient (PFG) driver, two waveform generators, and a Varian 5-mm $^{1}H/^{13}C/^{15}N$ triple resonance probe with actively shielded Z gradients (maximum strength: 33 G/cm). In all experiments, the H_2O signal was set on resonance in the proton dimension and ^{15}N carrier was set at 120.54 ppm.

Chemical-shift referencing conformed to published standards as follows[32]: the DSS (sodium 2,2-Dimethyl-2-Silapentane-5-Sulfonate) peak was set to 0 ppm for ^{1}H and ^{13}C nuclei, and the ^{15}N peak of 2.9 M $^{15}NH_4Cl$ in 1 M HCl was referenced to 24.9 ppm.

2.3.2 One-dimensional proton experiment

All high-resolution NMR studies on LFABP were performed in aqueous solution. The concentration of protons in water is approximately 110 M. Thus, the equilibrium magnetization of the water protons is approximately 10^4-10^5 greater than the equilibrium magnetization of a single proton in a macromolecule with its typical concentrations of 1-2 mM, making it necessary to reduce the resonance signal from water before the detection of the solute signals from protein.

The most commonly used solvent-suppression technique is presaturation of the solvent signal during the recycle delay using a weak radio-frequency (rf) field. Presaturation is very simple to implement and is very effective. The main disadvantages are that signals that resonate very close to the solvent signal (principally the α-protons in the protein) may be partially saturated by the rf field and that saturation transfer may partially saturate exchangeable protons. For the purpose of obtaining a general picture of the one-dimensional proton spectrum of the protein, presaturation is a good technique to use. As shown in **Fig. 2.1**, an irradiation time on the order of 2 s using a weak rf field is used for saturating the water signal before applying a 90° pulse to all protons. The experimental 1D ^{1}H spectrum of dual-labeled apo-LFABP at 1.3 mM, pH 6.0, and 30 °C (**Fig. 2.2**) shows the chemical shifts of backbone amide protons, side-chain amide protons, aromatic protons, aliphatic protons, methyl protons and water protons designated as HN (bb), HN (sc), ring, H1, CH_3, and H_2O, respectively. The quality of the water suppression obtained by presaturation depends very critically on the homogeneity of the magnetic field and hence on the quality of the shimming.

2.3.3 Two-dimensional ^{1}H-^{15}N HSQC experiments

^{1}H-^{15}N HSQC (Heteronuclear Single Quantum Coherence) is a two-dimensional one-bond heteronuclear correlation experiment in which the two frequency coordinates of a resonance are the chemical shifts of a heteronucleus (^{15}N) and a proton that is directly scalar coupled through one bond. In principle, the cross-peaks in ^{1}H-^{15}N HSQC spectrum can be assigned as backbone NH, side-chain NH_2 (a pair) from Asn and Gln residues, and side-chain NH from Arg, Trp, and His residues.

2.3.3.1 The conventional HSQC experiment[33]. Two INEPT sequences (Insensitive Nuclei Enhanced by Polarization Transfer) are used in the HSQC experiment. The first INEPT sequence is used to transfer I spin polarization (I_z) into antiphase heteronuclear single-quantum (SQ) coherence ($2I_zS_y$). The antiphase heteronuclear SQ coherence evolves during the subsequent t_1 evolution period. A second INEPT sequence, which is also called reverse INEPT, is used to transfer the frequency-labeled heteronuclear SQ coherence back to proton magnetization for detection. For a heteronuclear IS spin system, a conventional HSQC pulse sequence and detailed vector diagram are shown in **Fig. 2.3**, in which the delay $2\tau = 1/(2J_{IS})$ and evolution of the homonuclear ^{1}H scalar coupling interaction during the INEPT sequences has been ignored. The resultant term proportional to I_yS_x is unobservable multiple-quantum coherence.

2.3.3.2 Pulsed-field-gradient (PFG) with sensitivity-enhanced HSQC experiment[34]. In the conventional HSQC experiment (**Fig. 2.3**), heteronuclear SQ coherence evolves under the influence of the S spin chemical-shift Hamiltonian during the t_1 evolution period to yield two orthogonal terms proportional to $2I_zS_y$ and $2I_zS_x$. The second term is not refocused by the reverse INEPT sequence and does not contribute to the final observed magnetization. Therefore, on average, one-half of the initial I spin polarization does not contribute to the detected signal. To overcome this drawback, two improvements have been proposed and used together for acquiring HSQC spectra on our LFABP sample. (1) Sensitivity-enhanced technology, which has been denoted "preservation of equivalent pathways" (PEP-HSQC)[35], uses more pulses with a phase cycle to permit refocusing and detection of both orthogonal transverse magnetization

components and thus can provide sensitivity improvements by factors of up to $2^{1/2}$ relative to the conventional HSQC experiment. (2) Gradient-enhanced technology is used for coherence selection without sacrificing sensitivity to compensate the gain loss due to the increased number of pulses and delays in a PEP-HSQC experiment. A pulsed-field-gradient (PFG) HSQC experiment with sensitivity-enhancement is shown in **Fig. 2.4**. Both resultant magnetization terms, I_y and I_x, are detectable during t_2. Coherence selection is obtained using gradient pulses g_3 and g_8; the other gradient pulses are used to suppress artifacts associated with the 180° pulses. All gradient pulses also serve to effectively suppress water. For acquiring data on a dual-labeled protein, a 180° pulse is applied on the ^{13}C channel to decouple ^{13}C nuclei from the dual-labeled sample. The contour plot from the ^{1}H-^{15}N HSQC experiment on 1.3 mM recombinant $^{13}C/^{15}N$ double-labeled rat apo-LFABP, conducted at 30 °C and pH 6.0 on a three-channel Varian Unity*plus*-600 spectrometer, is shown in **Fig. 2.5**.

Running a ^{1}H-^{15}N HSQC experiment is also a simple and efficient way to check the condition of the sample. Changes in peak position or linewidth indicate sample condition changes, which may result from pH variation, concentration change, or sample denaturation.

2.3.4 A series of three-dimensional NMR experiments for resonance assignments

In all multidimensional NMR experiments, quadrature detection in the indirectly-detected dimensions was achieved using the States-TPPI method[36] because of its superior aliasing and axial peak suppression characteristics. Evolution beginning at half-dwell[37]

was utilized in several experiments in order to code aliased peaks with negative sign. Off-resonance carbon pulses were generated with a waveform generator[38], and the SEDUCE-1 method[39] was used to generate the soft pulses and decoupling pulses. Isotropic mixing (^{1}H and ^{13}C) was accomplished with the DIPSI-3 sequence[40]. Broadband ^{15}N and ^{13}C decoupling were applied during signal acquisition using the GARP1[41] and the WURST[42] methods, respectively. Efficient water-signal suppression was achieved by the use of gradients, and no presaturation was applied during the 1-s relaxation delays. Moreover, the water signal was flipped back to the +z axis prior to proton spin-lock and decoupling pulses, gradient pulses, and signal acquisition whenever possible [43;44], in order to minimize the attenuation of NH signal intensities through exchange with water.

Three-dimensional NMR experiments used for making resonance assignments of apo-LFABP included: (1) 3D heteronuclear triple-resonance experiments which correlate backbone $^{1}H^{N}$, ^{15}N, $^{1}H^{\alpha}$, $^{13}C^{\alpha}$, and ^{13}CO (and side-chain ^{1}H and ^{13}C) spins using one-bond and two-bond scalar coupling interactions, such as CBCA(CO)NH[45,46], HNCACB[47], HNCO[48], CBCACOHA[49], C(CO)NH-TOCSY[50] and H(CCO)NH-TOCSY[51]; (2) 3D ^{15}N-edited experiments which resolve cross-peaks between ^{1}H spins according to the chemical shift of ^{15}N bonded directly to the ^{1}H spins, such as TOCSY-HSQC and NOESY-HSQC[52]; and (3) 3D ^{13}C-^{13}C correlated experiments which are used in the assignment of aliphatic ^{1}H and ^{13}C resonances, such as HCCH-TOCSY[53]. Enhanced-sensitivity pulsed-field-gradient technology was employed in all of the 3D experiments. A combination of water-selective pulses and gradients was used to minimize saturation of water. A schematic representation of the nine 3D experiments is shown in **Fig. 2.6.**

The basic principle of triple-resonance NMR spectroscopy is to use magnetization transfer via heteronuclear couplings with a delay of the order of $1/J$. The typical range of those couplings is: $^1J_{NH}$ ~ 91 Hz, $^1J_{NC\alpha}$ ~ 7-11 Hz, $^2J_{NC\alpha}$ ~ 4-9 Hz, $^1J_{NC'}$ ~ 15 Hz, $^1J_{C\alpha C'}$ ~ 55 Hz, $^1J_{CH}$ ~ 140 Hz, and $^1J_{CC}$ ~ 35 Hz. Although different methods for magnetization transfer between nuclei are used, there are three methods in common use for the magnetization transfer steps: Insensitive Nuclei Enhanced by Polarization Transfer (INEPT, as used in the HSQC experiment), Heteronuclear Multiple Quantum Coherence (HMQC transfer), and Cross-Polarization (as used in TOCSY/HOHAHA). A generalized 3D multinuclear NMR experiment[7] is shown in **Fig. 2.7**. This experiment starts by generating transverse proton magnetization, which is transferred to the heteronuclei for the indirectly detected dimensions, and is transferred back to protons for detection at the end of the experiment.

2.3.4.1 CBCA(CO)NH and HNCACB. The CBCA(CO)NH experiment provides a sensitive and straightforward means for correlating the amide ^1H and ^{15}N resonances in a protein with both the $^{13}C^{\alpha}$ and $^{13}C^{\beta}$ resonances of the preceding residue. It relies on COSY-type magnetization transfer via the $^1J_{C\alpha C\beta}$ coupling, followed by magnetization relay from $^{13}C^{\alpha}$ via the carbonyl to the ^{15}N of the following residue, and is applicable to uniformly $^{13}C/^{15}N$-enriched proteins with a size up to 30 kDa. The HNCACB experiment primarily uses magnetization transfer via the $^1J_{NC\alpha}$ coupling to correlate the amide ^1H and ^{15}N resonances with those of the intra-residue $^{13}C^{\alpha}$ and $^{13}C^{\beta}$ resonances. However, since $^2J_{NC\alpha}$ (through carbonyl ^{13}C) is comparable to $^1J_{NC\alpha}$ in magnitude, the inter-residue $^{13}C^{\alpha}$ and $^{13}C^{\beta}$ resonances are also observed with weaker intensities. The $^{13}C^{\alpha}$ and $^{13}C^{\beta}$

resonances have different phase based on phase cycling design. The magnetization transfer pathway in HNCACB is illustrated as follows:

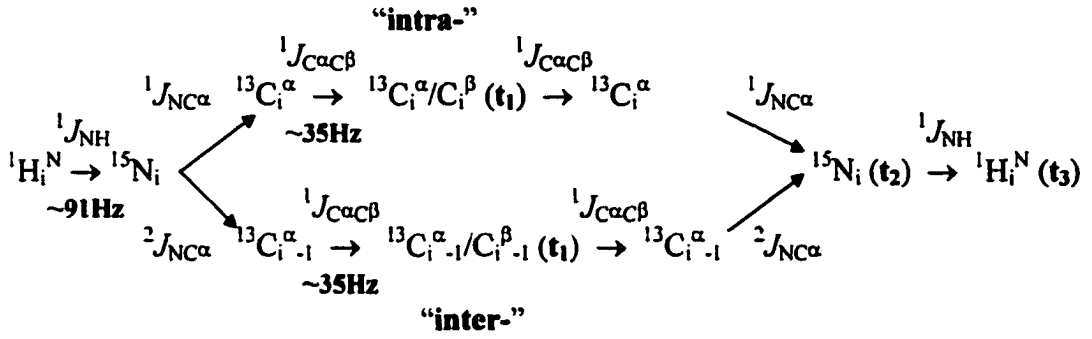

All $^{13}C^{\alpha/\beta}$ pulses in the CBCA(CO)NH and HNCACB experiments are applied near the center of the $^{13}C^\alpha$ and $^{13}C^\beta$ chemical-shift range in order to maximize excitation of the $^{13}C^\alpha$ and $^{13}C^\beta$ spins, and the power of these pulses is adjusted in order to minimize their effect on the carbonyl ^{13}C spins. Shaped selective 180° (carbonyl ^{13}C) pulses are applied to eliminate phase error induced by the off-resonance effects on the transverse ^{13}C magnetization. By combining the results of CBCA(CO)NH with HNCACB, the backbone amide ^1H and ^{15}N resonances can be correlated simultaneously with both the intra- and inter-residual $^{13}C^{\alpha/\beta}$ resonances, i.e., sequential assignments can be obtained.

2.3.4.2 HNCO experiment. The HNCO experiment correlates the amide ^1H and ^{15}N chemical shifts of one amino acid with the carbonyl ^{13}C chemical shift of the preceding residue, by using the one-bond ^{15}N-^{13}CO *J* coupling (~15 Hz) to establish the sequential correlation. Briefly, the magnetization-transfer pathway is

$$^1H_i^N \xrightarrow{^1J_{NH}} {}^{15}N_i \xrightarrow{^1J_{NC'}} {}^{13}C_i'{}_{-1}\,(t_1) \xrightarrow{^1J_{NC'}} {}^{15}N_i\,(t_2) \xrightarrow{^1J_{NH}} {}^1H_i^N\,(t_3),$$

where the active couplings involved in each transfer process are indicated above each arrow and t_i (i = 1-3) indicates that magnetization is observed during this time. **Fig. 2.8** illustrates a sensitivity-enhanced pulsed-field-gradient constant-time HNCO experiment

with selection of ^{15}N magnetization using a gradient applied during the ^{15}N evolution delay. The constant-time scheme here (a → c) inserts the ^{15}N evolution time t_2 in the required delay time 2T, which is used to refocus the anti-phase $^{15}N_x{}^{13}C_z$ magnetization into in-phase $^{15}N_y$ magnetization by the refocused INEPT (Insensitive Nuclei Enhanced by Polarization Transfer) sequence. Therefore, ^{15}N evolution is achieved without spending additional time that would lead to signal loses. The non-decaying signal during the constant-time 2T here is most useful in the linear prediction, which is important in the multidimensional experiments. In addition, the constant-time method can be used to minimize unwanted J-coupling in particular experiments. In this sequence, g_3 and g_8 are used to select the desired coherence-transfer pathway.

2.3.4.3 CBCACOHA experiment. CBCACOHA, a pulsed-field gradient experiment, correlates $^{13}C^{\beta/\alpha}$, $^{13}C'$, and $^{1}H^{\alpha}$ chemical shifts of a single residue with high sensitivity. Gradients are used to suppress the intense water signal that would otherwise obscure cross-peaks involving α protons near the water. The path of magnetization transfer is described concisely as

$$^{1}H_i^{\beta/\alpha} \xrightarrow{^{1}J_{CH}} {}^{13}C_i^{\beta/\alpha}(t_1) \xrightarrow{^{1}J_{C\alpha C\beta}} {}^{13}C_i^{\alpha} \xrightarrow{^{1}J_{C\alpha C'}} {}^{13}C_i'(t_2) \xrightarrow{^{1}J_{C\alpha C'}} {}^{13}C_i^{\alpha} \xrightarrow{^{1}J_{CH}} {}^{1}H_i^{\alpha}(t_3),$$

where the active couplings involved in each magnetization-transfer step are indicated above each arrow. No presaturation of the water signal was used.

2.3.4.4 Other 3D experiments. In theory, the experiments discussed above (HSQC, CBCA(CO)NH, HNCACB, HNCO, and CBCACOHA) are sufficient to make sequential backbone assignments. Nevertheless, the other 3D experiments presented below are not only used for establishing side-chain assignments and NOE's constraints, but are also helpful in checking the backbone assignments in the case of overlapped

chemical shifts of HN, CA, and CB nuclei. In that situation, side-chain information is really helpful for making unambiguous assignments.

C(CO)NH-TOCSY and *H(CCO)NH-TOCSY* experiments correlate all the aliphatic ^{13}C and ^{1}H resonances of an amino acid residue with the amide ^{1}H and ^{15}N resonances of the following residue. They are typically useful for making assignments of those residues with long side-chains, such as Leu, Ile, Val, and Lys. 3D ^{1}H-^{15}N *TOCSY-HSQC* and *NOESY-HSQC* spectra give the same information obtained from the F_1 (^{1}H)-F_2 ($^{1}H^{N}$) region of 2D ^{1}H-^{1}H NOESY and TOCSY spectra, but they are edited in a third dimension according to the ^{15}N chemical shift associated with the amide $^{1}H^{N}$. Their complete magnetization transfer pathways are

$$\text{TOCSY-HSQC:} \quad {}^{1}H_i(t_1) \xrightarrow{\text{TOCSY}} {}^{1}H_j \xrightarrow{{}^{1}J_{NH}} {}^{15}N_j(t_2) \xrightarrow{{}^{1}J_{NH}} {}^{1}H_j(t_3)$$

$$\text{NOESY-HSQC:} \quad {}^{1}H_i(t_1) \xrightarrow{\text{NOE}} {}^{1}H_j \xrightarrow{{}^{1}J_{NH}} {}^{15}N_j(t_2) \xrightarrow{{}^{1}J_{NH}} {}^{1}H_j(t_3).$$

The combination of H(CCO)NH-TOCSY and TOCSY-HSQC spectra is used for making sequential assignments for both backbone and side-chain protons. The last 3D experiment we present here is *HCCH-TOCSY*, which is the most commonly useful experiment for side-chain assignment ($H_i^x\ C_i^x\ H_i^{yz\cdots}$). It essentially provides the same information as the 2D TOCSY experiment, but the TOCSY transfer is among carbon rather than proton nuclei. The third dimension correlating the shifts of the ^{13}C nuclei attached to the diagonal protons (diagonal proton peaks in the 2D ^{1}H-^{1}H planes) reduces the overlap considerably. The flow of magnetization in this experiment can be described briefly by

$${}^{1}H_i(t_1) \xrightarrow{{}^{1}J_{CH}} {}^{13}C_i(t_2) \xrightarrow{{}^{1}J_{CC}} {}^{13}C_j \xrightarrow{{}^{1}J_{CH}} {}^{1}H_j(t_3),$$

where $^{1}H_{i(j)}$, $^{13}C_{i(j)}$ are one-bond coupled nuclei, $^{13}C_i$, $^{13}C_j$ are part of the same side-chain spin network, and the active couplings involved in each transfer step are indicated above each arrow.

2.3.4.5 Acquisition parameters for nD NMR experiments. The sensitivity-enhanced protocol[54,55] was employed for 2D HSQC and all of the NH-detected 3D experiments. The ^{15}N evolution was carried out in a constant-time manner[56], using a total delay of 24.8 ms in all experiments except the two ^{15}N-edited spectra. The two ^{15}N-edited experiments, TOCSY-HSQC and NOESY-HSQC, were acquired on a ^{15}N-labeled sample, whereas all other experiments were done with a $^{13}C/^{15}N$ dual-labeled sample. Constant-time $^{13}C^{\alpha/\beta}$ evolution[57] (for the purpose of scalar decoupling in ^{13}C dimension) was used in CBCA(CO)NH and CBCACOHA experiments with a total delay of 7.2 ms. The "shared-time" evolution method, in which the $^{1}H/^{13}C$ (scalar coupling) transfer time is used as part of the ^{1}H (chemical shift) evolution time to shorten this period by 3 ms [58,59], was used to acquire H(CCO)NH-TOCSY and C(CO)NH-TOCSY data and thus reduce the time required for the pulse sequences by 6 ms. Because all data were acquired in H_2O solution, additional water suppression by a pair of orthogonal ^{1}H purge pulses[60] was used in the CH-detected experiments, i.e., CBCACOHA and HCCH-TOCSY. The acquisition parameters (spectral width in each dimension, data points, experiment running time, etc.) of 2D ^{1}H-^{15}N HSQC and nine 3D experiments are listed in **Table 2.1**.

2.3.5 Experiments for assignments of aromatic (His, Phe, and Tyr) residues

In many proteins, aromatic residues (His, Phe, and Tyr in LFABP, no Trp) are involved in the construction of the hydrophobic core and thus a large number of relevant

long-range NOE contacts can be identified. A wealth of triple-resonance methods has been developed which allow establishment of sequential connectivities via the scalar coupling network. In contrast, the assignment of aromatic ^{1}H and ^{13}C resonances traditionally relies on the establishment of NOE connectivities between the H^{β} and H^{α} protons of the aromatic residue and its associated ring protons. Two-dimensional (HB)CB(CGCD)HD and (HB)CB(CGCDCE)HE experiments[61], based exclusively on the transfer of magnetization via scalar couplings, provide correlations between the side-chain $^{13}C^{\beta}$ and ring $^{1}H^{\delta}/^{1}H^{\varepsilon}$ chemical shifts. The path of magnetization transfer can be described concisely as follows:

(HB)CB(CGCD)HD: $\overset{{}^{1}J_{CH}}{\rightarrow}\ {}^{1}H^{\beta} \overset{{}^{1}J_{CC}}{\rightarrow}\ {}^{13}C^{\beta}(t_1) \overset{{}^{1}J_{CC}}{\rightarrow}\ {}^{13}C^{\gamma} \overset{{}^{1}J_{CH}}{\rightarrow}\ {}^{13}C^{\delta} \rightarrow\ {}^{1}H^{\delta}(t_2)$

(HB)CB(CGCDCE)HE: $\overset{{}^{1}J_{CH}}{\rightarrow}\ {}^{1}H^{\beta} \overset{{}^{1}J_{CC}}{\rightarrow}\ {}^{13}C^{\beta}(t_1) \overset{{}^{1}J_{CC}}{\rightarrow}\ {}^{13}C^{\gamma} \overset{{}^{1}J_{CC}}{\rightarrow}\ {}^{13}C^{\delta} \overset{{}^{1}J_{CH}}{\rightarrow}\ {}^{13}C^{\varepsilon} \rightarrow\ {}^{1}H^{\varepsilon}(t_2).$

Gradients are used in the sequence to suppress artifacts, aid in the removal of water, and minimize the phase cycling required. The ^{13}C carrier is positioned in the center of the $^{13}C^{\beta}$ chemical shift range (35 ppm), and the carbon frequency is jumped from 35 to 125 ppm (aromatic range). **Fig. 2.9** shows 2D spectra for both the $^{13}C^{\beta}$-$^{1}H^{\delta}$ and $^{13}C^{\beta}$-$^{1}H^{\varepsilon}$ correlation maps for the apo-protein. The experimental measuring times for (HB)CB(CGCD)HD and (HB)CB(CGCDCE)HE were 18 h and 24 h, respectively.

2.4 NMR Data Processing

2.4.1 NMRPipe

NMRPipe[62] is a multidimensional NMR spectral processing system written by Frank Delaglio at the National Institutes of Health. It is based on UNIX pipes

implemented in the C programming language, allowing programs running simultaneously to exchange streams of data under user control. The central module of the NMRPipe system is called **nmrPipe**, which applies a given processing function (**-fn**) to a stream of spectral data.

The first step is to establish the conversion of data from the spectrometer format to the NMRPipe format, which includes the acquisition modes, data sizes and chemical shift calibration information for each dimension. A 2D conversion script used for a ^{1}H-^{15}N pulsed-field-gradient HSQC FID acquired on a Varian Unity*plus* 600 spectrometer is given in **Fig. 2.10**. The FID file named as "oct2495yh_apolfabp_pfg_hsqc.fid" under /apo directory is converted to "oct2495_pfg_hsqc_pipe.fid" under FID directory. With the NMRDraw program, we can inspect the raw FID data and correct the phase of the data in the detected dimension.

The second step is to process the nD spectrum via pipelines using the processing script. **Fig. 2.11** gives a processing script used for the above 2D HSQC data. The output file named as "oct2495_pfg_hsqc_proc.dat" can be opened in NMRDraw to adjust the phases in both dimensions and used directly by the NMRView program (Section 2.4.2). For the 3D and 4D data, the processing script is written by the use of a 2D in-memory transpose called **xyz2pipe**.

All the multidimensional NMR data were processed with the NMRPipe program on a Sun workstation (SunSparc MP670, NMR). In all of the NH-detected data sets, the amide proton signal of residue Phe3 (at 11.46 ppm) that resonated just outside of the spectral width was retrieved with a small circular shift (128 data points) to the right. The right half of these data sets was then discarded to conserve disk space. Similarly, the

acquisition dimension of H(CCO)NH-TOCSY data was shifted to the left by SW/4, and the right half of the data set was then discarded. The indirect ^{1}H dimension of the H(CCO)NH-TOCSY experiment covered only 5 ppm, but aliasing was detected through negative peaks and corrected with a left circular shift. The NMRPipe program tracked all operations and produced correct chemical shifts after complicated maneuvers. The processing parameters for 2D pulsed-field-gradient HSQC and nine 3D data are summarized in **Table 2.2**.

2.4.2 NMRView

NMRView, a computer program for the visualization and analysis of NMR data, is written by Bruce A. Johnson at Merck Research Laboratories[63]. The 'nv' file of NMRView is created directly by converting NMRPipe-processed data to NMRView format. For example, to convert the NMRPipe file of "oct2495_pfg_hsqc_proc.dat" (Section 2.4.1) to NMRView format and generate an output file as "oct2495_pfg_hsqc.nv", the following simple script must be run:

```
nmrPipe -in DATA/oct2495_pfg_hsqc_proc.dat   \
| pipe2xyz -nv -out MAT/oct2495_pfg_hsqc.nv -verb
```

Then, the 2D pfg-HSQC spectrum can be displayed by opening "oct2495_pfg_hsqc.nv" in NMRView and doing further analysis, such as peak picking, getting intensities, and so on.

NMRView is designed to visualize multiple files at one time. Any number of spectral windows can be displayed on the screen with any size and location. Thus, each window could be displaying a different file, or different regions of the same file, or any

combination thereof. Data from 2D, 3D or 4D data sets can be displayed as 1D vectors or as 2D contour plots. With the benefit of the Tcl scripting language and Tk toolkit[64], multiple sets of multidimensional NMR data can be examined with tracking cursors and it is possible to find chemical-shift matches for sequential linkages in an interactive manner. In addition to making sequential assignments, the advantages from NMRView are the ability to derive secondary structure, conduct kinetic analysis, and make NOE identifications for structure calculation. **Fig. 2.12** shows an image of the computer screen during an NMRView session. Two windows are opened to display 2D HSQC spectra and 2D contour strips from 3D CBCA(CO)NH and HNCACB experiments in a particular ^{15}N plane. This example makes clear the $^{13}C^{\alpha/\beta}$ connectivity pathway between CBCA(CO)NH and HNCACB experiments.

2.5 ^{1}H, ^{13}C and ^{15}N Resonance Assignments

2.5.1 Strategy

In the initial stage of any structural investigation by NMR spectroscopy, each resonance must be associated with a specific nucleus in the molecule under investigation. Resonance assignments must be *sequence-specific*: each resonance must be assigned to a spin in a particular amino acid residue in the protein sequence. Information on amino acid type can be obtained from ^{13}C chemical-shift data. The distributions of $^{13}C^{\alpha}$ and $^{13}C^{\beta}$ chemical shifts for different amino acid residues from a database of 13 proteins[65] are plotted in **Fig. 2.13**. The characteristic $^{13}C^{\alpha}$ and $^{13}C^{\beta}$ chemical shifts of alanine, valine, threonine, serine, and glycine residues allow ready identification of these amino acid types from CBCA(CO)NH and HNCACB data. This information, coupled with the

alignment of sequentially connected spin systems with the known amino acid sequence and the knowledge of other aliphatic ^{13}C chemical shifts, leads to unambiguous sequential assignments.

Thus, our strategy is to start the assignments by looking for the 'special pairs' of amino acid residues in the sequence with distinctive and unique $^{13}C^{\alpha}$ and $^{13}C^{\beta}$ chemical shifts, such as Gly, Ser, Thr, and Val (**Fig 2.13**). The consecutive two amino acids fragment constituted by one or two of the above four residues is considered as a 'special pair' to start to deal with. In our case, $Ser^{4}Gly^{5}$, $Gly^{37}Val^{38}$, $Gly^{55}Ser^{56}$, $Thr^{75}Gly^{76}$, and $Thr^{93}Thr^{94}$ sequence pairs are readily identifiable in LFABP. For example, if we choose $Gly^{37}Val^{38}$ to begin and complete the assignments after Val^{38}, the following steps are needed:

(1) Load HNCACB experiment in NMRView and go through the ^{1}H-^{13}C planes to find three cross peaks at the NH resonance frequency of Val^{38} (one weak cross peak is inter-residual Gly^{37}, two strong cross peaks are intra-residual Val^{38}, and the negative one is $^{13}C^{\beta}$);

(2) Use the NMRView Tcl command "find" to find two cross peaks of Val^{38} in the ^{1}H-^{13}C plane of the CBCA(CO)NH experiment *at the NH resonance frequency of* Ser^{39};

(3) Load the ^{1}H-^{13}C plane of HNCACB at the NH resonance of Ser^{39}, which has two pairs of $^{13}C^{\alpha/\beta}$ cross peaks, the inter-residual Val^{38} (weak) and the intra-residual Ser^{39} (strong);

(4) Use the command "find" again to find the inter-residual Ser^{39} in CBCA(CO)NH *at NH resonance of* Glu^{40}.

Thus, HNCACB and CBCA(CO)NH are used alternately to make the forward resonance assignments until a "blockage" is encountered in any one of the following situations: the next residue is proline (no NH resonance), the next residue is unobservable in the ^{1}H-^{15}N HSQC spectrum due to rapid exchange with solvent, or $^{13}C^{\alpha/\beta}$ chemical shifts of the next residue are overlapped. Under these circumstances, it is necessary to choose another typical sequence pair to begin with.

2.5.2 Backbone resonance assignments

There are two sequential connections available to make the backbone assignments: (1) through the $^{13}C^{\alpha/\beta}$ connectivity pathway by using CBCA(CO)NH and HNCACB data sets as described above; and (2) through the aliphatic ^{1}H connectivity pathway by finding ^{1}H resonance matches in H(CCO)NH-TOCSY and TOCSY-HSQC data sets. As an example, connectivity patterns of both pathways for the region G76-V82 of apo-LFABP are illustrated in **Fig. 2.14**. In principle, 2D ^{1}H-^{15}N HSQC combined with 3D CBCA(CO)NH and HNCACB data sets are enough to make sequence-specific assignments via the $^{13}C^{\alpha/\beta}$ connectivity pathway except for those $^{13}C^{\alpha/\beta}$ chemical-shift overlapped residues which need be identified by side-chain ^{13}C shift information obtained in the C(CO)NH-TOCSY experiment. For complete backbone assignments, HNCO and CBCACOHA are also needed to get ^{13}CO and $^{1}H^{\alpha}$ assignments.

2.5.3 Side-chain resonance assignments

Side-chain aliphatic ^{1}H and ^{13}C assignments are made using H(CCO)NH-TOCSY, TOCSY-HSQC, and C(CO)NH-TOCSY data sets. The HCCH-TOCSY experiment was

not only used for checking the aliphatic ^{1}H and ^{13}C assignments, but also for getting new assignments for the residues with very weak NH resonances. Occasionally the connectivity pathways were interrupted because of the low signal-to-noise ratio of signals in NH-detected experiments. It was possible, however, to identify the amino acid type first from CH-based experiments and confirm the connectivity subsequently. For example, the identification strategy for K121 is shown in **Fig. 2.15**. A Lys ^{1}H trace was initially located in the HCCH-TOCSY data at a ^{13}C shift of 54.4 ppm, which allowed us to find its $^{1}H^{\alpha}$ trace in HCCH-TOCSY and NH trace in TOCSY-HSQC, respectively. Once the NH strip was found, its connection to Y120 was made through the $^{13}C^{\alpha/\beta}$ pathway and confirmed by the ^{13}CO shift from CBCACOHA and HNCO experiments. Finally, the K121 $^{13}C^{\beta}$ resonance found in the HNCACB data corroborated the $^{13}C^{\beta}$ trace found from HCCH-TOCSY. Detailed analysis of the HCCH-TOCSY spectrum yielded complete assignment of K121 (with the exception of the ammonium group) and revealed magnetic inequivalences for the two $^{1}H^{\beta}$ and two $^{1}H^{\gamma}$ nuclei. This highly interactive procedure also illustrates how the validity of our LFABP assignments was established by cross checking the results of many independent experiments.

2.6 Results and Discussion

2.6.1 Completion of assignments

Table 2.3 summarizes the sequential resonance assignments obtained for the apo form of rat LFABP at 30 °C and pH 6.0. For this protein, it was possible to make backbone amide (^{1}H and ^{15}N) assignments for 109 of 127 residues. Taking into account the two prolines and the terminal residue, this result amounted to a 87.9 % success rate,

limited primarily by our ability to detect the NH resonances. A larger percentage of the resonances was assigned for other nuclei: 94.5 % for $^{13}C^{\alpha}$, 93.9 % for $^{13}C^{\beta}$, 92.9 % for ^{13}CO, 93.5 % for $^{1}H^{\alpha}$, 84.8 % for the side-chain ^{13}C, and 89.8 % for the side-chain ^{1}H, respectively.

There are 6 Asn and 4 Gln in LFABP, producing 10 pairs of side-chain NH_2 signals in the ^{1}H-^{15}N HSQC spectrum (see **Fig. 2.5**). The side-chain NH_2 resonance assignments can be made by running an edited CBCA(CO)NH experiment with a delay of $1/4J_{NH}$ instead of $1/2J_{NH}$. The side-chain ^{13}CO resonance assignments of Asn, Gln, Asp, and Glu residues can be made by running an edited CBCACOHA experiment with a delay of $1/4J_{CH}$ instead of $1/2J_{CH}$. For Glu and Gln residues, the edited CBCACOHA crosspeaks of the side-chain ^{13}CO resonance (~180 ppm) allowed for unambiguous differentiation of $^{1}H^{\beta}$ and $^{1}H^{\gamma}$ resonances. For other long side-chain amino acids, the ^{1}H assignments were confirmed through the HCCH-TOCSY crosspeaks of the respective ^{13}C resonances.

It was possible to both corroborate and extend the ^{1}H side-chain connections using $d_{\alpha N}$ crosspeaks from a NOESY-HSQC data set. For instance, the K90 $^{1}H^{\alpha}$ shift at 5.95 ppm was not located in the first search because we had circular-shifted our H(CCO)NH-TOCSY data to cover the region 5.49-0.51 ppm in the ω_1 (^{1}H) dimension. A $d_{\alpha N}$ peak from the M91 NOESY-HSQC strip suggested a sequential assignment to K90 at 5.95 ppm, and in fact the corresponding H(CCO)NH-TOCSY peak was found to be aliased at 0.95 ppm. Because we began the ω_1 evolution with a half-dwell delay, the sign of the crosspeaks was coded with respect to the spectral width of the experiment.

Therefore, the identification of this resonance was unambiguous and the assignment withstood all crosschecks mentioned previously.

Many of the observed NH signals were quite broad (35-40 Hz) for a protein of this size, suggesting an unusually flexible internal structure and/or rapid exchange with solvent for apo-LFABP. This feature will be discussed further in Chapter 3. Moreover, 33 of the NH resonances had a doubled appearance in ^{1}H-^{15}N HSQC, CBCA(CO)NH, and HNCACB spectra of apo-LFABP. Both effects contributed to spectral crowding in certain areas of the HSQC spectrum. For example, the strip chart in **Fig. 2.14** displays duplicate NH resonances for G76, V79, and V82. Their side-chain ^{13}C and ^{1}H shifts were identical, and their backbone ^{15}N and ^{13}CO positions agreed to within fractions of a part per million. The doubling effect has been reported previously in the ^{1}H-^{15}N HSQC spectra of bovine HFABP and attributed to multiple local conformations[24]. When oleate was bound to ^{15}N-labeled LFABP, the anomalously broad NH signals sharpened considerably and many more of the missing peaks became visible in the ^{1}H-^{15}N HSQC spectrum (to be presented in Chapter 4). This last observation can be explained if backbone flexibility and disorders, which may be substantial in the apo protein, are diminished dramatically upon binding of the FA ligand.

2.6.2 Secondary structure derived from sequential assignments (CSI)

The chemical-shift indices (CSI)[66] provides a simple algorithm for identifying protein secondary structures based on the independent chemical-shift measurements of backbone ^{13}C and $^{1}H^{\alpha}$ nuclei. It is well known that both $^{13}C^{\alpha}$ and ^{13}CO experience a downfield shift when they are located in helices and an upfield shift when they are

located in β-strands[67,68]; both $^{13}C^{\beta}$ and $^{1}H^{\alpha}$ resonances experience an upfield shift when located in helices and a downfield shift when located in β-strands[69]. Given the strong correlation between chemical shift and secondary structure and additional chemical shift information for 'random coil' states, a chemical-shift index is assigned to all identifiable residues on the basis of their observed chemical shifts. A value of -1 represents an upfield shift, a value of +1 represents a downfield shift, and a value of 0 represents no shift with respect to the random coil value. By combining ^{1}H and ^{13}C chemical-shift indices, a consensus secondary structure assignment is made using values of -1 and +1 to represent helices and β-strands, respectively.

The sequential assignments of the ^{1}H and ^{13}C backbone nuclei for the apo form of rat LFABP were used along with chemical-shift indices program to provisionally identify its secondary structural elements. The result revealed 10 β-strands and 2 α-helices intervening between β-strands A and B (**Fig. 2.16**). In many cases, the loop junctures between secondary structural elements appeared to coincide with missing amide proton resonances in the ^{1}H-^{15}N HSQC spectrum (**Fig. 2.5**). Despite significant functional differences between LFABP and other FABPs in terms of binding and FA transport (Section 1.3), a remarkably similar pattern of β-strand structures and α-helical motifs is shared by apo-LFABP with an IFABP-palmitate complex[70], CRABP[71], and HFABP[24]. Additional support for the CSI results comes from the NOESY-HSQC (^{15}N) data (**Fig. 2.17**), which displayed strong d_{NN} (i, i±1) as well as weak $d_{\alpha N}$ (i, i+1) and $d_{\alpha N}$ (i, i+3) connectivities that identify α-helices. Strong $d_{\alpha N}$ (i, i+1) connecivities and weak d_{NN} (i, i+1) connectivities, which are predominant throughout the rat LFABP amino acid sequence, indicate β-strands.

The work of NMR assignments and secondary structure determination on the apo form of rat LFABP was presented on the 26th Keystone Symposium on Molecular and Cellular Biology in 1997 and published on the Journal of Biomolecular NMR in 1998[72].

Figure 2.1 Pulse sequence of 1D proton presaturation experiment. A long, weak pulse is applied before the 90° pulse to suppress the protons from water.

Figure 2.2 1D ^{1}H spectrum of 1.3 mM $^{13}C/^{15}N$ apo-LFABP at pH 6.0 and 30 °C. The Chemical shift ranges of backbone amide protons, side-chain amide protons, aromatic protons, aliphatic protons, methyl protons, and protons from water are indicated by HN (bb), HN (sc), ring, H1, CH_3, and H_2O, respectively. The strong peaks around 3.5-3.8 ppm are impurities that are glycerol from a Centricon membrane.

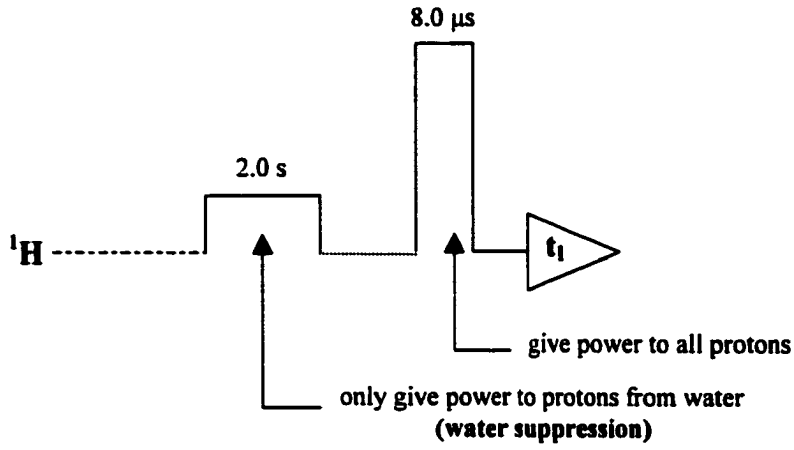

Figure 2.1

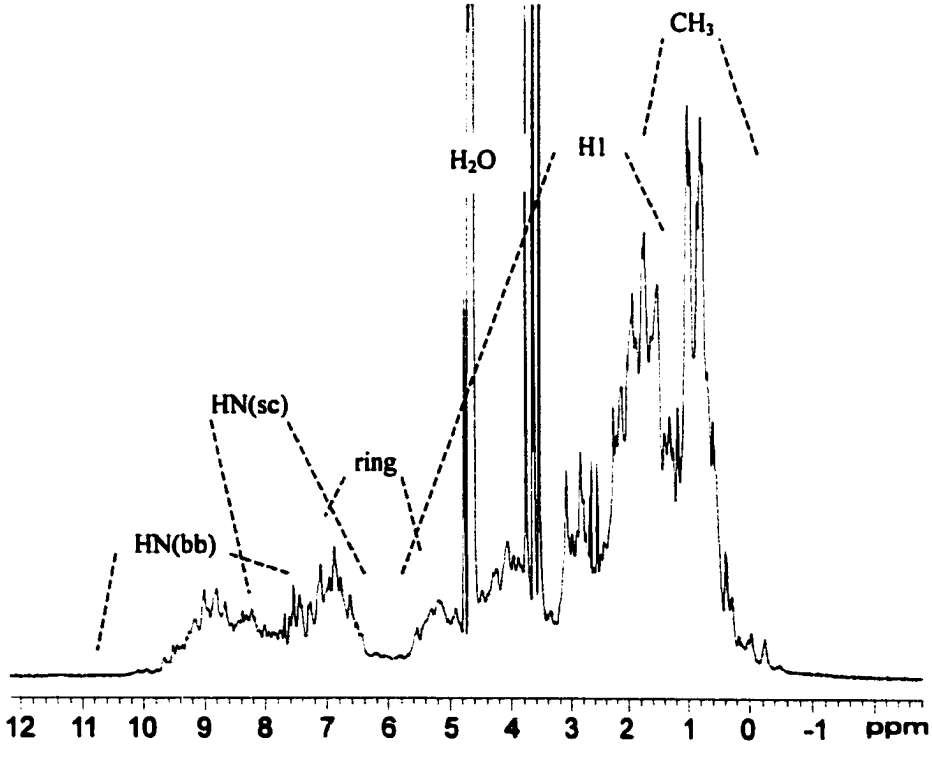

Figure 2.2

Figure 2.3 (a) Pulse sequence for conventional HSQC experiment[33]. Thin bars represent 90° pulses and thick bars represent 180° pulses. The phase of each pulse is indicated above the bar. (b) Detailed illustration of (a) by vectors and spin operators.

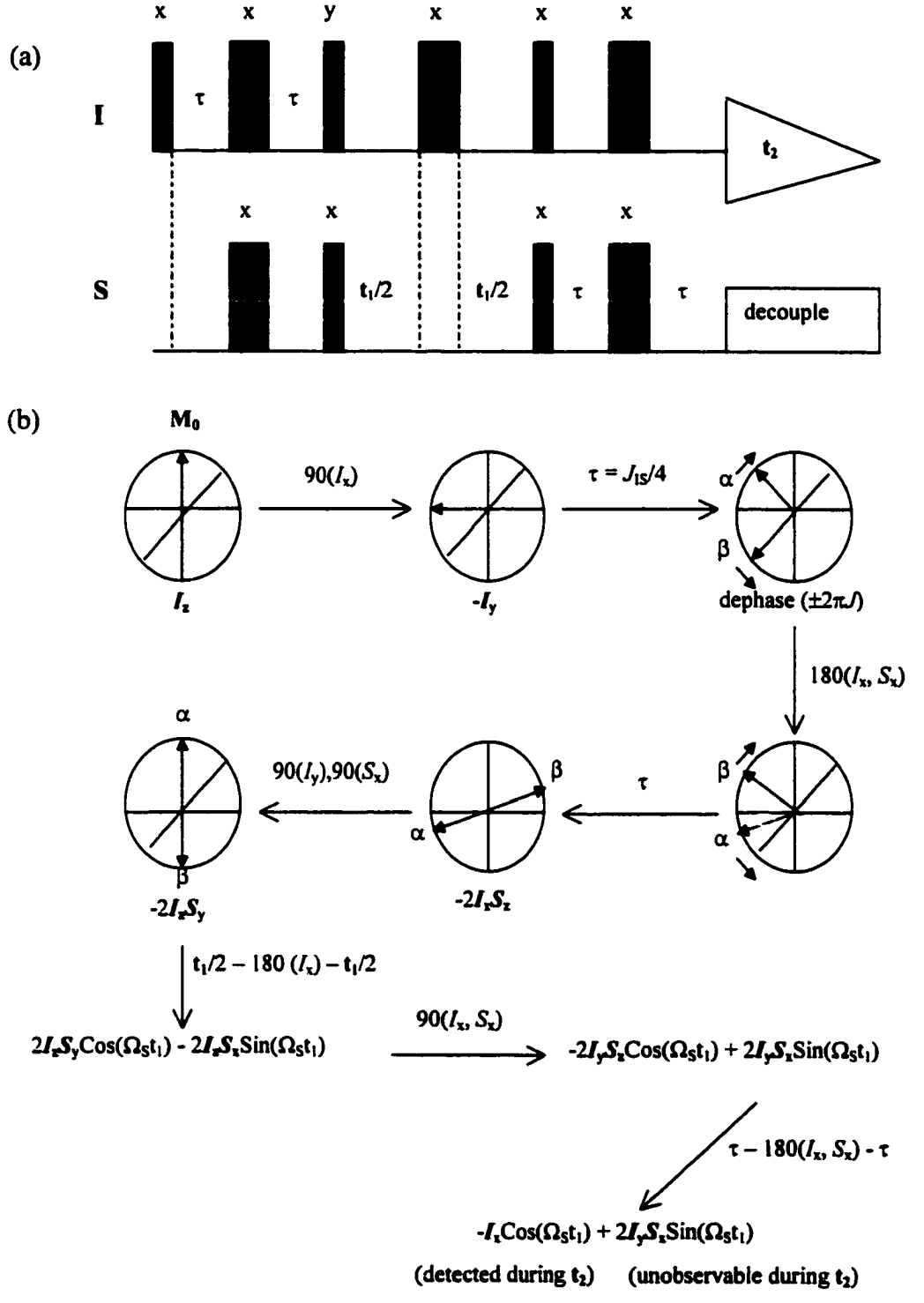

Figure 2.3

Figure 2.4 Pulse sequence of the pulsed-field-gradient with sensitivity-enhanced ^{1}H-^{15}N HSQC experiment[34]. The delays, 2τ, are set to $1/(2J_{IS})$. Gradient pulses g_3 and g_8 are for coherence selection, are applied with a strength of 30 G/cm and duration of 2.5 ms and 0.25 ms, respectively. All gradient pulses are rectangular and applied along the z-axis. Decoupling is achieved with the use of the GARP decoupling sequence using a 1.1 kHz radio frequency field. Water suppression is achieved solely with the use of the gradient pulses.

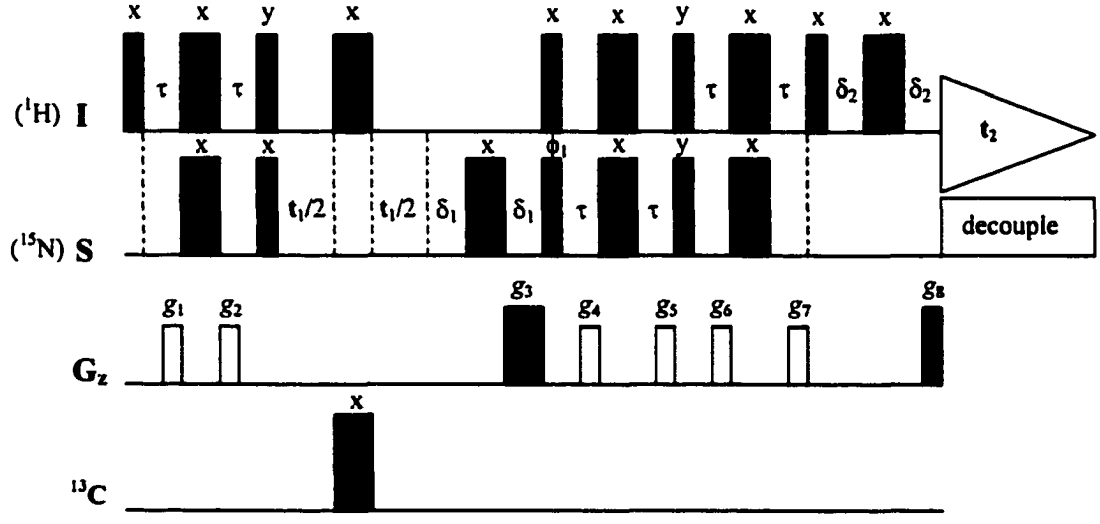

Figure 2.4

Figure 2.5 ^{1}H-^{15}N pulsed-field-gradient HSQC spectrum of 1.3 mM $^{13}C/^{15}N$ double-labeled apo rat LFABP at 30 °C and pH 6.0. Assigned correlations are labeled according to amino acid codes and residue numbers for the backbone amides; horizontal lines link side-chain NH_2's of the Asn and Gln residues. Assignment methods are described in Sections 2.3.4-2.3.5.

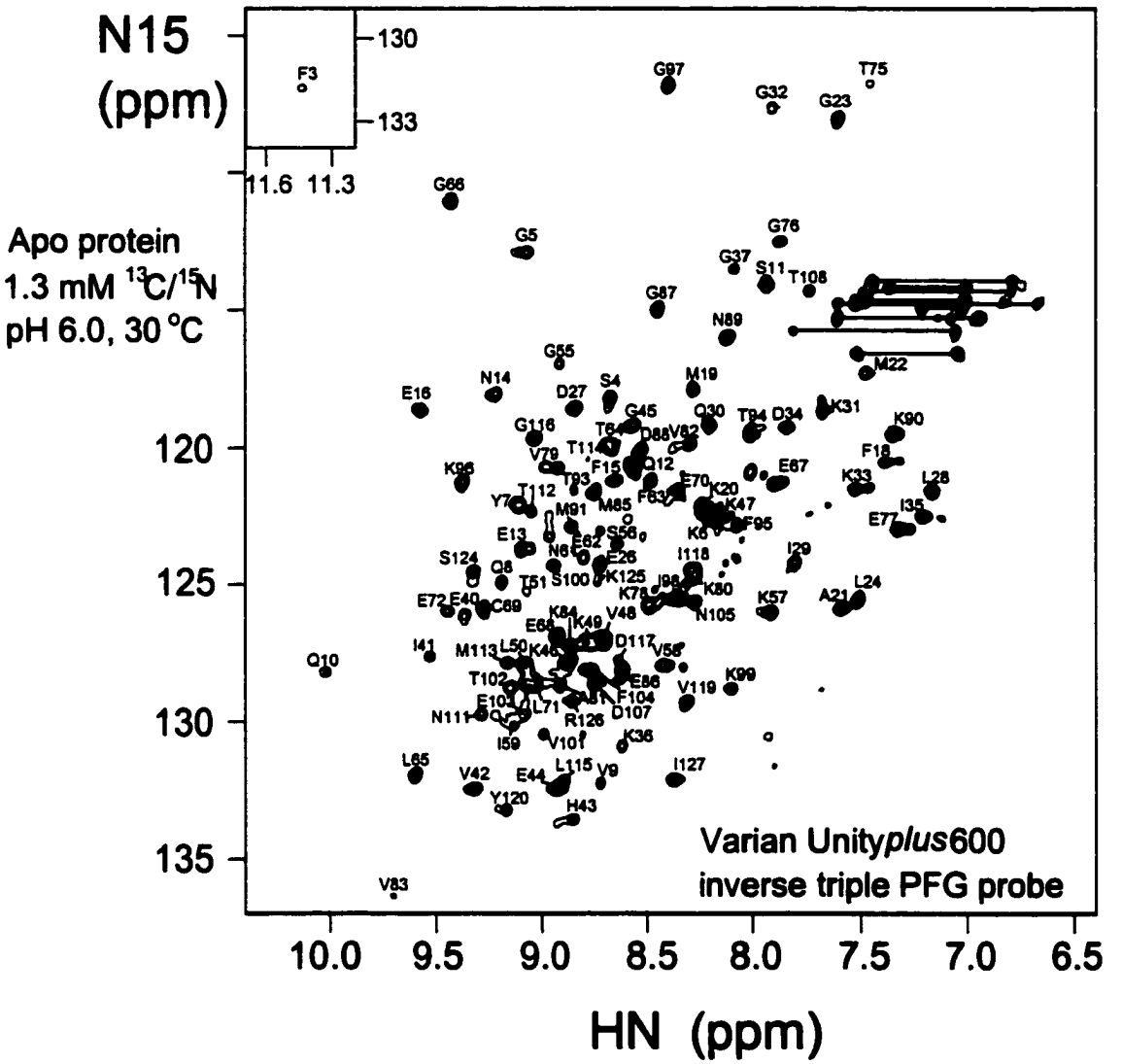

Figure 2.5

Figure 2.6 Schematic representation of nine 3D experiments used for protein resonance assignments. The nuclear spins of the *i*th amino acid residue are designated H_i^N for the amide proton spin, N_i for the amide ^{15}N spin, H_i^κ and C_i^κ for aliphatic proton and ^{13}C spins ($\kappa = \alpha, \beta, \gamma$, etc.), and C_i' for the carbonyl ^{13}C spin.

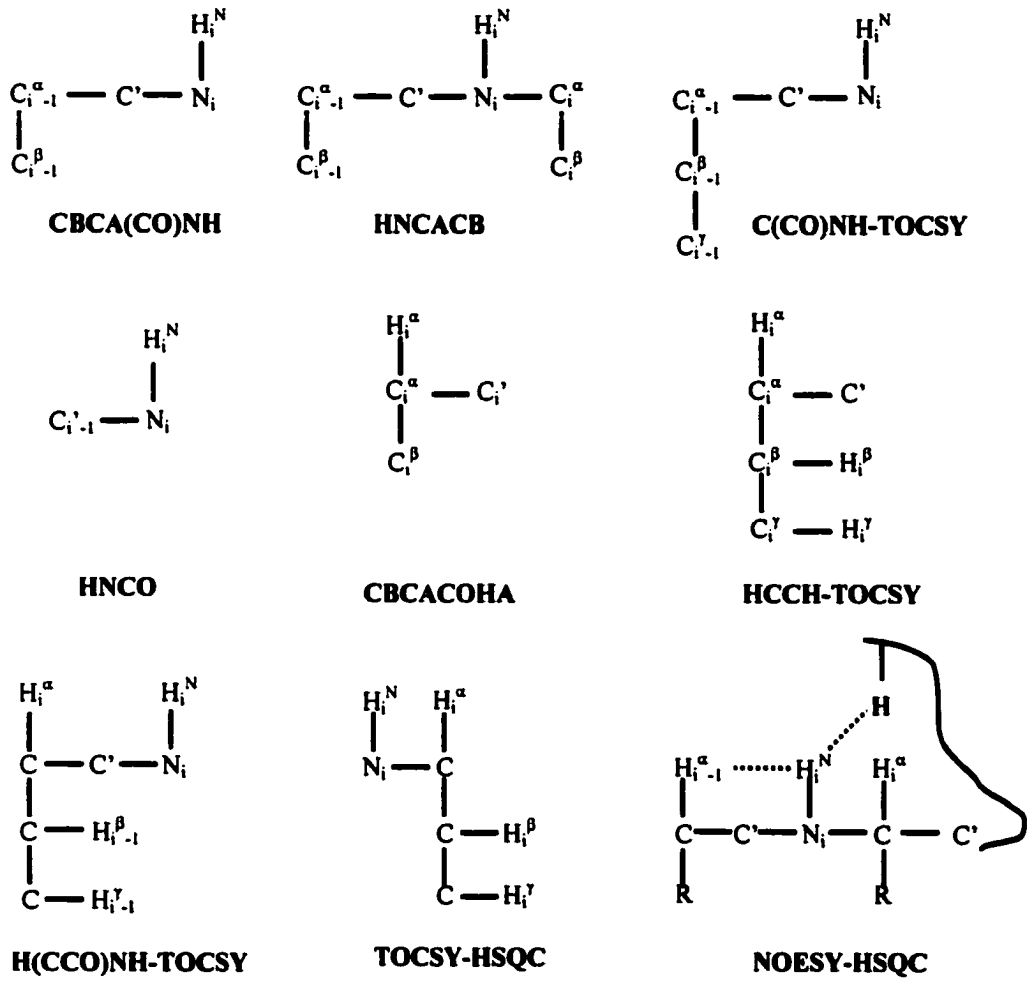

Figure 2.6

Figure 2.7 A general 3D multinuclear NMR experiment[7]. 1. Transverse proton magnetization is generated. 2. Magnetization transferred to first heteronucleus (^{15}N). 3. First indirectly detected dimension. 4. Magnetization transferred to second heteronucleus (^{13}C). 5. Second indirectly detected dimension. 6. Magnetization returned to protons. 7. Acquisition on protons.

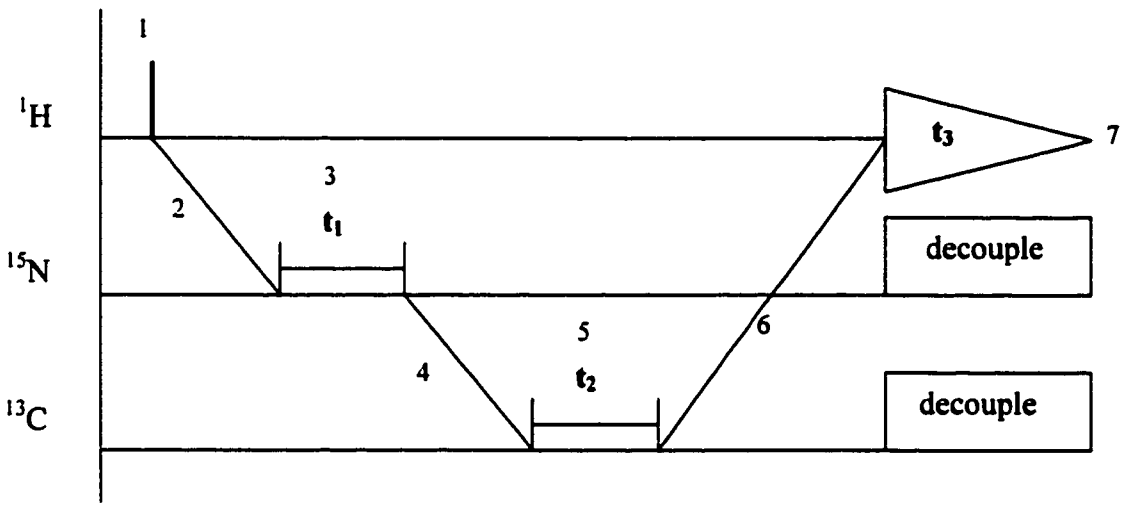

Figure 2.7

Figure 2.8 Sensitivity-enhanced constant-time HNCO experiment[48] with selection of ^{15}N magnetization using a gradient applied during the ^{15}N evolution delay. The values of τ_a, τ_b, and τ_c are set to $1/(4J_{NH})$, $1/(2J_{NH})$, and $1/(4J_{NH})$, respectively. The values of T_N, T, and ζ are set to 12.4 ms, 12.4 ms, and 300 μs, respectively. WALTZ decoupling is achieved using a 5.3 kHz field on the ^1H channel, and GARP decoupling is achieved using a 625 Hz field on the ^{15}N channel. SEDUCE-1 decoupling, centered at 54 ppm and using a 825 Hz field, ensures that ^{15}N magnetization does not evolve due to scalar coupling to $^{13}C^{\alpha}$ during the constant-time t_2 evolution period. All $^{13}C'$ pulses are applied at a field strength of 4.8 kHz so that minimal excitation occurs in the C^{α} region. The $^{13}C^{\alpha}$ 180° pulse is applied with field strength of 9.0 kHz, which minimizes the perturbation of the C' spins. In the gradient sequences, the shaded gradients are used to select for a particular coherence-transfer pathway. The strengths and durations of g_3 and g_8 are 30 G/cm, 2.5 ms and ±29.1 G/cm, 0.25 ms, respectively. In contrast, the other gradients at a strength of 5 G/cm and duration of 500 μs are inserted to aid in the suppression of artifacts caused by pulse imperfections. Water suppression is achieved via the combined action of gradients g_3 and g_8. All gradients are in the z direction. Pulses applied along the x-axis have no designations on the timing diagram. The phase cycling employed is as follows: ϕ_1 = y, -y; ϕ_2 = x, -x; ϕ_3 = 2(x), 2(-x); ϕ_4 = x; ϕ_5 = 4(x), 4(y), 4(-x), 4(-y); ϕ_6 = x and -x; Acq = 2(x), 4(-x), 2(x).

Figure 2.9 2D spectra showing a portion of the $^{13}C^{\beta}$, $^1H^{\delta}$ correlation map (A) and a portion of the $^{13}C^{\beta}$, $^1H^{\varepsilon}$ correlation map (B) for the 1.3 mM apo-$^{13}C/^{15}N$ dual-labeled LFABP sample at 30 °C and pH 6.0. Both data sets were recorded with acquisition times of 8 ms in t_1, 1024 scans per complex t_1 point, and relaxation delays of 0.9 s to give measuring times of 18 h and 24 h, respectively.

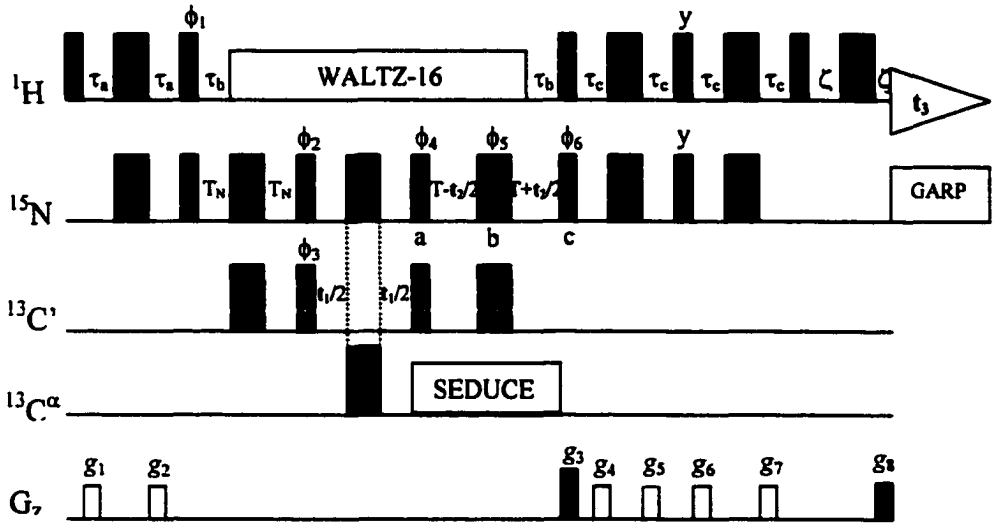

Figure 2.8

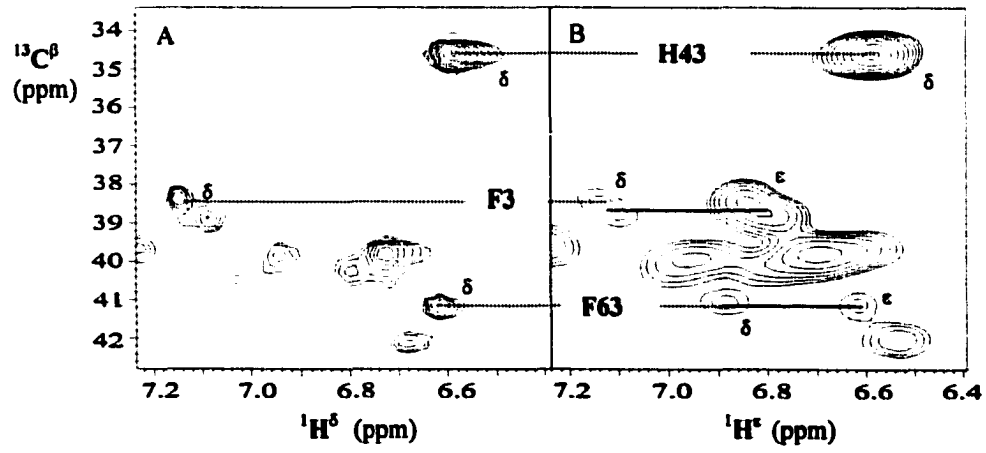

Figure 2.9

Figure 2.10 *Annotated* format conversion script used for a 2D ^{1}H-^{15}N pulsed-field-gradient HSQC FID acquired on a Varian Unity*plus* 600 spectrometer with a 1.3 mM $^{13}C/^{15}N$ dual-labeled apo-LFABP at 30 °C and pH 6.0.

Figure 2.11 *Annotated* processing script for 2D ^{1}H-^{15}N pulsed-field-gradient HSQC data. The input and output files are specified by the template arguments **-in** and **-out.**

```
var2pipe -in /apo/oct2495yh_apolfabp_pfg_hsqc.fid/fid      \   Spectrometer -Format Input
 -xN              2048          -yN              512       \   Total points in file
 -xT              1024          -yT              256       \   Complex points acquired
 -xMODE        Complex          -yMODE        Complex      \   Acquisition mode
 -xSW           8000.0          -ySW           2000.0      \   Spectral width, Hz
 -xOBS           599.95         -yOBS            60.80      \   Observe frequency, MHz
 -xCAR             4.69         -yCAR           120.54      \   Carrier position, ppm
 -xLAB               HN         -yLAB                N      \   Axis labels
 -ndim                2         -aq2D           States      \   Dimension count, 2D mode
| nmrPipe -fn MAC -macro $NMRTXT/ranceY.M -noRd -noWr \       pulsed-field-gradient
 -out FID/oct2495_pfg_hsqc_pipe.fid -verb -ov       \        Output file
```

Figure 2.10

```
nmrPipe -in FID/oct2495_pfg_hsqc_pipe.fid          \   -Format Input
| nmrPipe -fn SOL -fl 64                           \   Solvent filter
| nmrPipe -fn SP -off 0.45 -end 1.00 -pow 2 -c 0.5 \   Window
| nmrPipe -fn ZF -auto                             \   Zero fill
| nmrPipe -fn FT -auto                             \   Fourier transform
| nmrPipe -fn PS -p0 -118.2 -p1 0.0 -di -verb      \   Phase, delete imaginaries
| nmrPipe -fn CS -rs 128 -sw                       \   Circular shift to the right
| nmrPipe -fn POLY -auto -ord 0                    \   Auto baseline correct
| nmrPipe -fn EXT -left -sw                        \   Extract the left half
| nmrPipe -fn TP                                   \   Transpose X/Y
| nmrPipe -fn SP -off 0.5 -end 1.00 -pow 2 -c 1.0  \   Window
| nmrPipe -fn ZF -auto                             \   Zero fill
| nmrPipe -fn FT -auto                             \   Fourier transform
| nmrPipe -fn PS -p0 -90 -p1 180 -di -verb         \   Phase correct
```

Figure 2.11

Figure 2.12 An image of the computer screen during an NMRView session. The session illustrated has two open screen windows displaying a region of the ^{1}H-^{15}N HSQC experiment (window with header 'a') and four strips of ^{1}H-^{13}C planes from 3D CBCA(CO)NH and HNCACB experiments (window with header 'b'). The cursors are placed on the amide proton resonances of Leu65 and Gly66, respectively, showing the $^{13}C^{\alpha/\beta}$ connectivity pathway (Thr64 → Leu65 → Gly66) between CBCA(CO)NH and HNCACB data sets. In the HNCACB strips, both inter- and intra- $^{13}C^{\alpha/\beta}$ pairs are shown. To find the amide resonance of Gly66 from Leu65, the command 'find cbcaconh 57.0 42.3' (on the left-top corner of the screen) based on the intra-pair of Leu65 at peak number {45,51} in the second strip results in a pair at peak number {400,401} in the third strip.

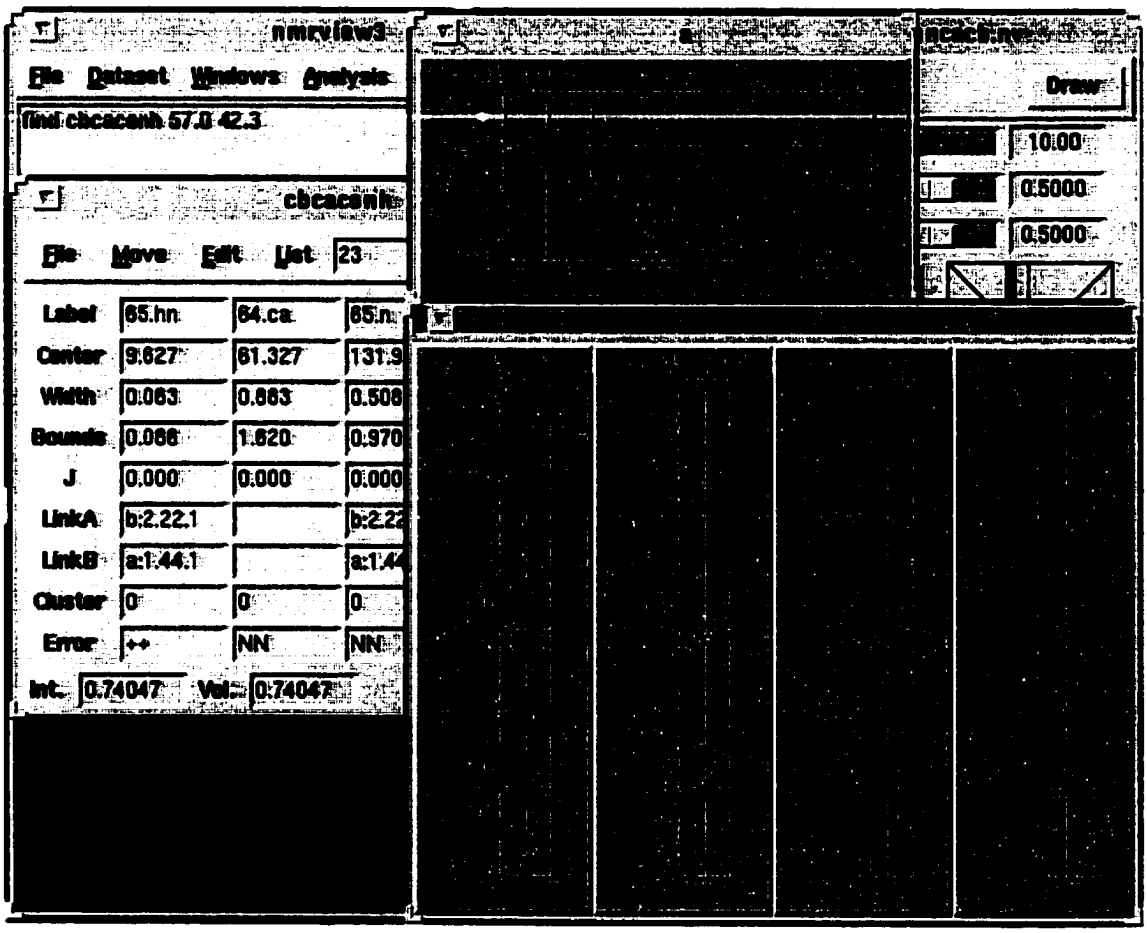

Figure 2.12

Figure 2.13 Plot of $^{13}C^{\alpha}$ and $^{13}C^{\beta}$ chemical shifts for 19 amino acids excluding glycine. The $^{13}C^{\alpha}$ chemical shift of glycine is around 45 ppm. The data source is from database of 13 proteins[65].

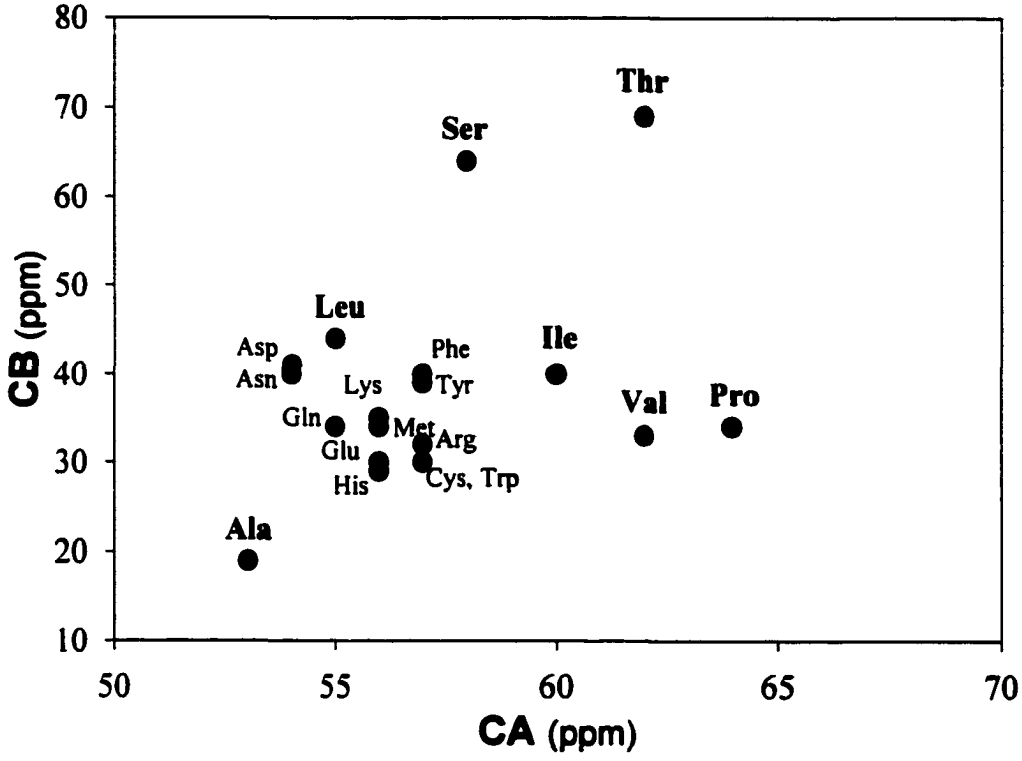

Figure 2.13

Figure 2.14 Sequential through-bond connections in the region G76-V82, made by the $^{13}C^{\alpha/\beta}$ connectivity pathway (top panel) and the aliphatic ^{1}H connectivity pathway (bottom panel)[72]. Each strip is a plot from the ^{15}N plane (ω_3) centered at the NH shift (ω_1) of the indicated residue. The respective pairs of experiments used to establish the connectivities are noted at the right-hand side of each panel. Connections made at the same NH chemical shift are denoted by dotted lines, and the connections made by side-chain matchup of different residues are marked by solid lines.

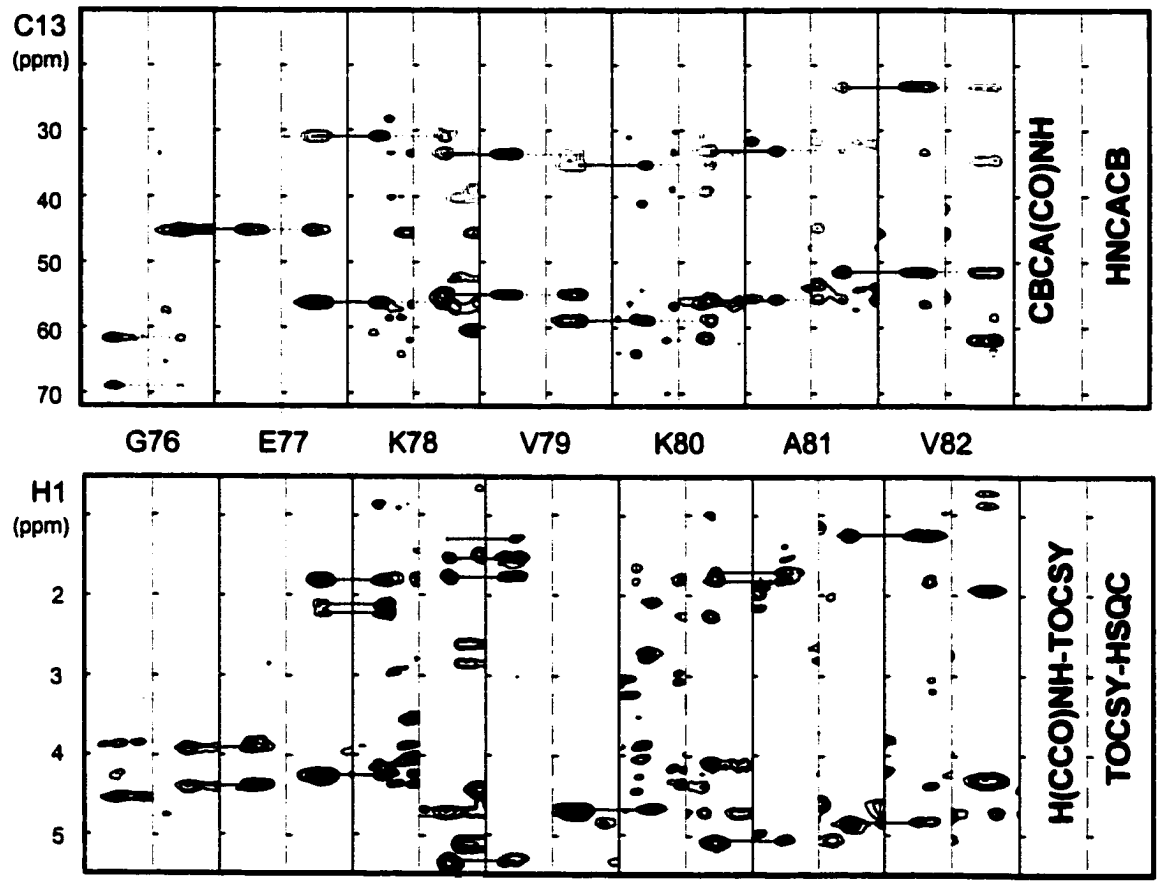

Figure 2.14

Figure 2.15 The identification of K121 spin systems using a scheme of six double- and triple- resonance NMR experiments. Details of the strategy are provided in the text.

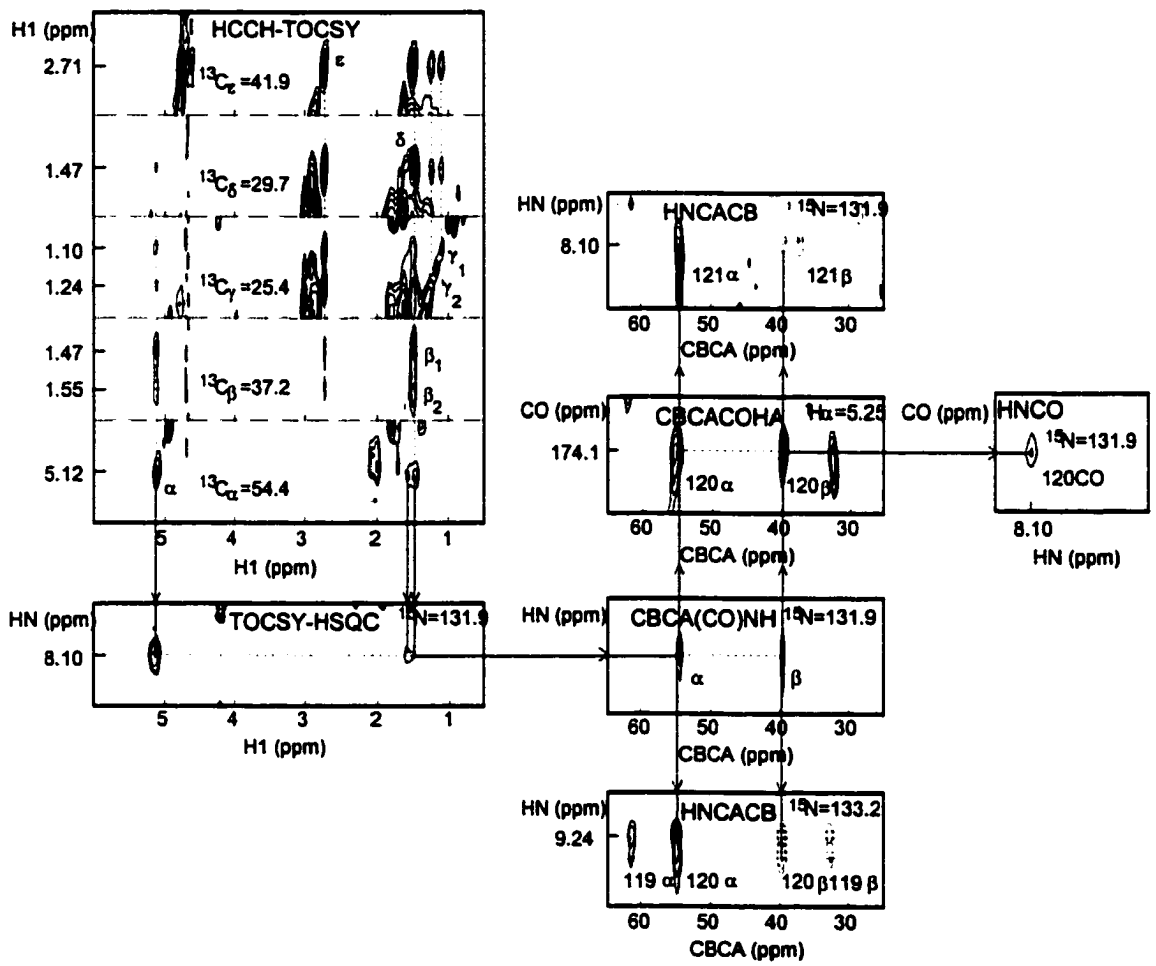

Figure 2.15

Figure 2.16 Chemical-shift indices (CSI) for the prediction of solution-state secondary structure in the apo form of rat LFABP.

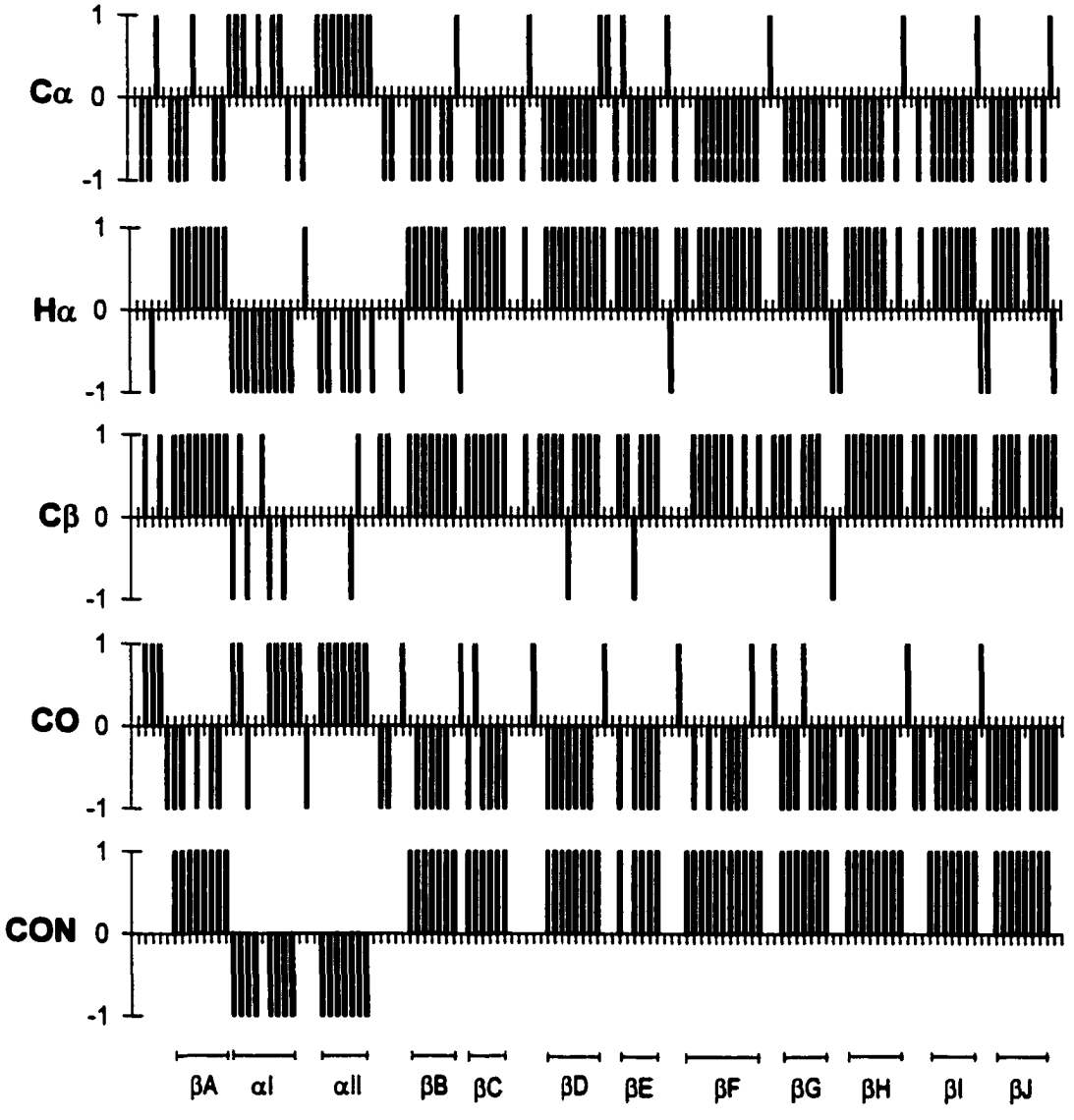

Figure 2.16

Figure 2.17 NOE connectivities observed in a NOESY-HSQC (^{15}N) spectrum measured with a mixing time of 100 ms. The top panel represents a strip plot for the α-helical region E26-I35. The lines denote d_{NN} (i, i±1) and $d_{\alpha N}$ (i, i+3) connectivities. The bottom panel represents an interstrand β-sheet (βG-βJ) hydrogen-bonding pattern between pairs of proton spins.

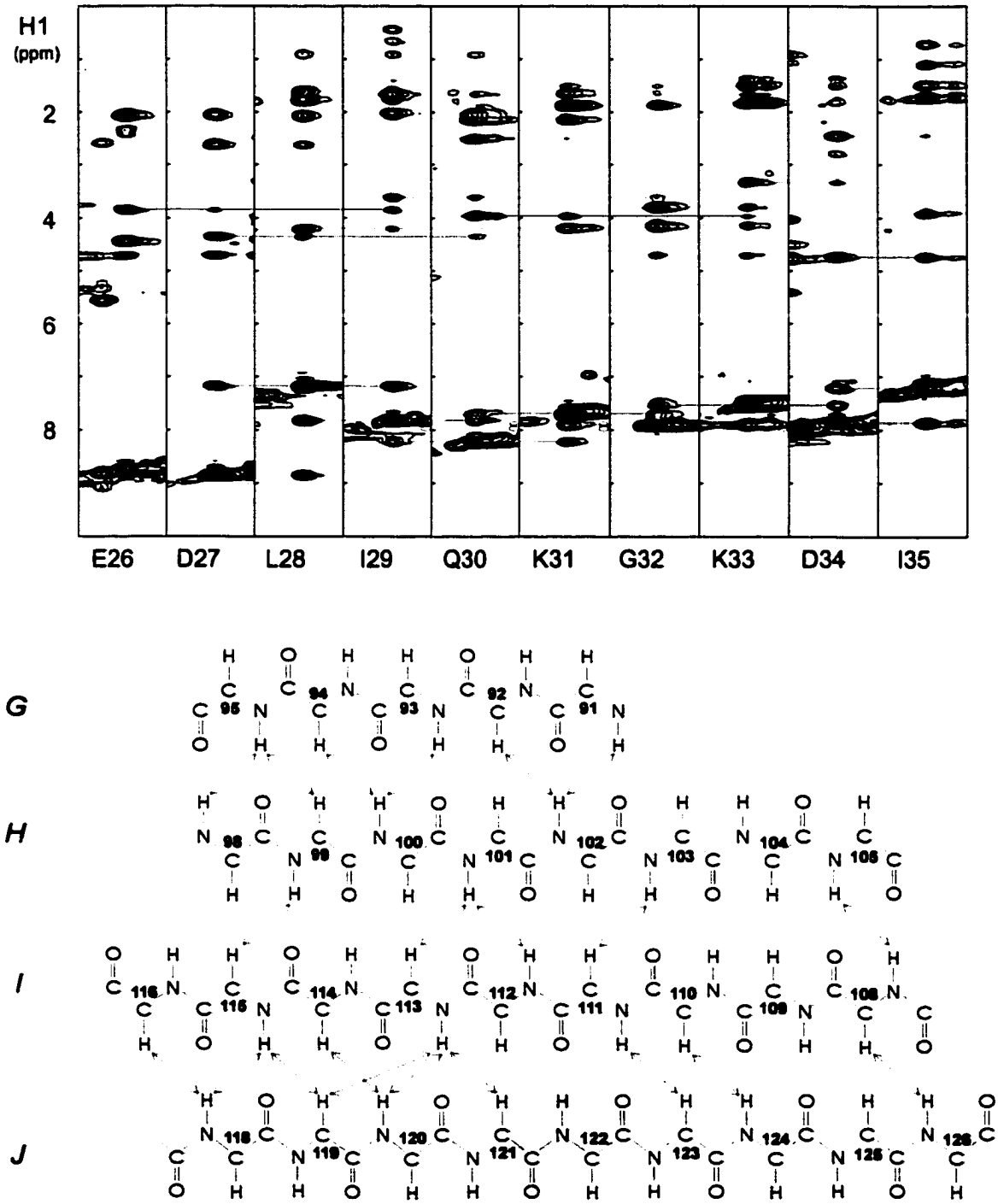

Figure 2.17

Table 2.1 Acquisition parameters for nD NMR experiments on apo-LFABP at 30 °C and pH 6.0.

Table 2.2 Processing parameters for nD NMR experiments on apo-LFABP.

Table 2.1

Experiment	Axes f1/f2/f3	Spectral Widths (kHz) SW1/SW2/SW3	Complex Data Points	Mixing Time (ms)	Half-Dwell Evolution	Scans	Time (h)
pfg – HSQC	$^{15}N/^{1}HN$	2.0/8.0	160/1024		yes/-	16	1.7
CBCA(CO)NH	$^{13}C_{\alpha,\beta}/^{15}N/^{1}HN$	9.2/2.0/8.0	54/32/512		no/no/-	16	35.6
HNCACB	$^{13}C_{\alpha,\beta}/^{15}N/^{1}HN$	9.2/2.0/8.0	32/36/512		yes/no/-	32	47.5
HNCO	$^{13}CO/^{15}N/^{1}HN$	2.0/2.4/8.0	48/36/512		yes/no/-	16	35.6
CBCACOHA	$^{13}C_{\alpha,\beta}/^{13}CO/^{1}H$	8.8/1.8/8.0	52/64/512		no/yes/-	16	68.1
H(CCO)NH-TOCSY	$^{1}H/^{15}N/^{1}HN$	3.0/2.0/8.0	72/36/512	12.6	yes/no/-	32	108.1
C(CO)NH-TOCSY	$^{13}C/^{15}N/^{1}HN$	9.2/2.0/8.0	50/32/512	12.6	no/no/-	32	66.2
TOCSY-HSQC(^{15}N)[a]	$^{1}H/^{15}N/^{1}HN$	8.0/2.0/8.0	120/36/512	45	no/no/-	16	89.1
NOESY-HSQC(^{15}N)[a]	$^{1}H/^{15}N/^{1}HN$	8.0/2.0/8.0	112/36/512	100	no/no/-	16	87.0
HCCH-TOCSY	$^{1}H/^{13}C/^{1}H$	4.2/3.6/8.0	128/31/512	14.1	no/no/-	16	67.5

[a] These experiments were conducted with ^{15}N-labeled LFABP rather than $^{13}C/^{15}N$ dual-labeled protein samples.

Table 2.2

Experiment[a]	Axes f1/f2/f3	Linear Prediction (forward)	Zero Fill	Windows	Matrix Size
pfg - HSQC	$^{15}N/^{1}HN$	0/0	512/2048	$\sin(90°,180°)/\sin^2(81°,180°)$	512/1024
CBCA(CO)NH	$^{13}C_{\alpha,\beta}/^{15}N/^{1}HN$	10/0/0	128/64/1024	$\sin(90°,176°)/\sin^2(90°,176°)/\sin^2(81°,176°)$	128/64/1024
HNCACB	$^{13}C_{\alpha,\beta}/^{15}N/^{1}HN$	16/28/0	128/128/1024	$\sin(90°,176°)/\sin^2(90°,176°)/\sin^2(81°,176°)$	128/128/1024
HNCO	$^{13}CO/^{15}N/^{1}HN$	16/28/0	128/128/1024	$\sin(90°,176°)/\sin^2(90°,176°)/\sin^2(81°,176°)$	128/128/1024
CBCACOHA	$^{13}C_{\alpha,\beta}/^{13}CO/^{1}H$	12/0/0	128/128/1024	$\sin(90°,176°)/\sin(90°,176°)/\sin^2(81°,176°)$	128/128/1024
H(CCO)NH-TOCSY	$^{1}H/^{15}N/^{1}HN$	56/28/0	256/128/1024	$\sin^2(90°,176°)/\sin^2(90°,176°)/\sin^2(81°,176°)$	256/128/1024
C(CO)NH-TOCSY	$^{13}C/^{15}N/^{1}HN$	14/0/0	128/64/1024	$\sin(90°,176°)/\sin^2(90°,176°)/\sin^2(81°,176°)$	128/64/1024
TOCSY-HSQC(^{15}N)[b]	$^{1}H/^{15}N/^{1}HN$	8/28/0	256/128/1024	$\sin(90°,176°)/\sin^2(90°,176°)/\sin^2(81°,176°)$	256/128/1024
NOESY-HSQC(^{15}N)[b]	$^{1}H/^{15}N/^{1}HN$	16/28/0	256/128/1024	$\sin(90°,176°)/\sin^2(90°,176°)/\sin^2(81°,176°)$	256/128/1024
HCCH-TOCSY	$^{1}H/^{13}C/^{1}H$	0/23/0	256/128/1024	$\sin(90°,176°)/\sin^2(90°,176°)/\sin^2(81°,176°)$	256/128/1024

[a] All experiments are correspond to those listed in **Table 2.1.**
[b] These experiments were conducted with ^{15}N-labeled LFABP rather than with $^{13}C/^{15}N$ dual-labeled protein samples.

Table 2.3 ^{1}H, ^{13}C and ^{15}N chemical shifts for apo form of rat LFABP at pH 6.0 and 30 °C.

Table 2.3

Spin	^{15}N	^{1}HN	^{13}CO	$^{1}H^{\alpha}$	$^{13}C^{\alpha}$	$^{1}H^{\beta}$	$^{13}C^{\beta}$	Other ^{1}H	Other ^{13}C
Asn[2]			176.0	4.81	52.3	2.83,2.57	40.4		
Phe[3]	131.8	11.5	177.0	4.53	56.9	3.07,2.45	38.7		
Ser[4]	118.3	8.70	174.2	4.43	61.1	4.13,4.00	64.4		
Gly[5]	113.0	9.10	170.1	3.96,3.78	45.4				
Lys[6]	122.5	8.19	174.8	5.20	55.5	1.64	34.9	H^{γ} 1.44,1.25; H^{δ} 1.64; H^{ε} 2.89	C^{γ}26.2; C^{δ}29.8; C^{ε}42.3
Tyr[7]	122.2	9.13	174.8	5.23	56.0	2.68,2.48	42.1		
Gln[8]	125.0	9.22	176.2	5.21	54.3	2.04	32.6	H^{γ} 2.38,2.24	C^{γ} 33.9
Val[9]	132.3	8.75	175.3	4.10	65.2	1.93	33.0	$H^{\gamma 1}$ 0.98; $H^{\gamma 2}$ 0.86	$C^{\gamma 1}$ 23.2; $C^{\gamma 2}$ 21.4
Gln[10]	128.3	10.1	176.0	4.53	56.0	2.19,1.97	32.1	H^{γ} 2.41	C^{γ} 34.5
Ser[11]	114.1	7.96	172.2	4.75	57.6	3.85	65.3		
Gln[12]	120.8	8.59	174.4	5.46	54.9	2.24	33.5	H^{γ} 2.48,2.40	C^{γ} 34.4
Glu[13]	123.8	9.12	175.7	4.88	55.2	2.13,1.91	33.9	H^{γ} 2.30	C^{γ} 36.3
Asn[14]	118.1	9.24	174.6	4.55	55.0	3.73,3.13	36.2		
Phe[15]	121.3	8.68	176.3	3.86	62.7	3.17,2.33	40.5		
Glu[16]	118.7	9.60	175.3	3.86	62.4	2.24	27.0	H^{γ} 2.31	C^{γ} 37.7
Pro[17]			179.6	4.25	65.6	2.35,1.77	31.0	H^{γ} 2.14; H^{δ} 3.74, 3.66	C^{γ} 28.2; C^{δ} 49.7
Phe[18]	120.5	7.41	176.1	3.96	62.4	3.04,2.89	40.6		
Met[19]	117.8	8.31	179.5	3.95	56.8	1.40	31.6	H^{γ} 1.86, 1.49	C^{γ} 32.9
Lys[20]	122.2	8.27	180.7	3.97	59.5	1.79	32.4	H^{γ} 1.49,1.34; H^{δ} 1.65; H^{ε} 2.94	C^{γ}25.6;C^{δ}29.4;C^{ε}42.2
Ala[21]	125.9	7.62	179.5	4.04	54.7	1.33	18.1		
Met[22]	117.4	7.51	176.5	4.16	55.5	1.87	33.2	H^{γ} 2.05	C^{γ} 32.5
Gly[23]	108.1	7.63	175.0	4.15,3.69	45.3				
Leu[24]	125.6	7.54	174.3	4.40	53.8	1.41,1.20	41.9	H^{γ} 1.66; $H^{\delta 1}$ 0.85; $H^{\delta 2}$ 0.77	C^{γ}28.4;$C^{\delta 1}$25.2;$C^{\delta 2}$25.2
Pro[25]			177.9	4.47	62.8	2.45, 2.08	32.9	H^{γ} 2.13; H^{δ} 4.00,3.52	C^{γ} 28.1; C^{δ} 51.0
Glu[26]	124.3	8.75	178.3	3.87	60.1	2.07	30.0	H^{γ} 2.35	C^{γ} 36.3
Asp[27]	118.6	8.87	178.5	4.38	57.1	2.66	40.1		
Leu[28]	121.7	7.19	180.3	4.24	57.2	1.81, 1.62	42.0	H^{γ} 1.75; $H^{\delta 1}$ 0.99; $H^{\delta 2}$ 0.91	C^{γ}27.4;$C^{\delta 1}$25.1;$C^{\delta 2}$23.8
Ile[29]	124.2	7.83	177.8	3.65	66.1	2.04	38.0	$H^{\gamma 1}$ 1.70,0.46; $H^{\gamma 2}$ 0.94; H^{δ} 0.67	$C^{\gamma 1}$29.5;$C^{\gamma 2}$18.1;C^{δ}13.7
Gln[30]	119.3	8.23	178.7	4.00	58.7	2.16	28.3	H^{γ} 2.52	C^{γ} 33.8
Lys[31]	118.8	7.70	178.6	4.22	58.5	1.90	33.3	H^{γ} 1.65,1.53; H^{δ} 1.69; H^{ε} 3.00	C^{γ}25.8; C^{δ}29.3; C^{ε}42.4
Gly[32]	107.7	7.93	175.5	4.15,3.81	46.2				
Lys[33]	121.6	7.55	176.1	3.37	58.9	1.86	32.4	H^{γ} 1.51; H^{δ} 1.43; H^{ε} 3.06	C^{γ} 24.3; C^{δ} 29.8
Asp[34]	119.3	7.87	176.0	4.79	54.4	2.83,2.50	41.8		
Ile[35]	122.6	7.23	176.3	3.95	61.5	1.76	38.3	$H^{\gamma 1}$ 1.52,1.12; $H^{\gamma 2}$ 0.74; H^{δ} 0.77	$C^{\gamma 1}$27.6;$C^{\gamma 2}$17.3;C^{δ}13.0
Lys[36]	130.9	8.65	176.1	4.30	55.7	1.82	32.0	H^{γ} 1.28; H^{δ} 1.65; H^{ε} 3.01	C^{γ} 24.9; C^{δ} 29.3
Gly[37]	113.6	8.11	174.3	3.97,3.67	45.6				
Val[38]									
Ser[39]			172.9	5.37	57.2	3.76	65.7		
Glu[40]	126.2	9.39	175.1	5.33	55.4	1.94	33.0	H^{γ} 2.22,2.07	C^{γ} 37.0
Ile[41]	127.7	9.56	176.3	5.07	60.6	2.26	40.9	$H^{\gamma 1}$ 1.74,1.07; $H^{\gamma 2}$ 0.81; H^{δ} 0.87	$C^{\gamma 1}$27.8;$C^{\gamma 2}$17.8;C^{δ}13.6
Val[42]	132.5	9.35	173.8	4.23	63.1	2.09	33.5	$H^{\gamma 1}$ 0.97; $H^{\gamma 2}$ 0.83	$C^{\gamma 1}$ 20.8; $C^{\gamma 2}$ 20.8
His[43]	133.7	8.95	174.1	5.53	53.0	3.34,2.53	34.7		
Glu[44]	132.5	8.95	175.8	4.38	54.8	1.90,1.85	31.9	H^{γ} 2.07	C^{γ} 36.2
Gly[45]	119.3	8.59	174.4	4.01,3.56	47.4				
Lys[46]	127.9	8.89	175.1	4.60	56.5	2.27, 1.87	33.7	H^{γ} 1.62,1.57; H^{δ} 1.79; H^{ε} 3.05	C^{γ}25.8;C^{δ}29.8; C^{ε} 42.8
Lys[47]	122.5	8.19	177.9	4.79	56.2	1.94, 1.69	33.7	H^{γ} 1.45,1.29; H^{δ} 1.68; H^{ε} 2.96	C^{γ}25.2; C^{δ}29.2; C^{ε}41.0
Val[48]	127.0	8.74	174.2	4.59	61.1	1.80	33.9	$H^{\gamma 1}$ 0.67; $H^{\gamma 2}$ 0.48	$C^{\gamma 1}$ 22.0; $C^{\gamma 2}$ 22.0
Lys[49]	127.2	8.80	174.9	4.81	55.3	2.17	34.4	H^{γ} 1.79; H^{δ} 1.98,1.90; H^{ε} 3.83	C^{γ}25.0; C^{δ}31.8; C^{ε}42.1
Leu[50]	128.0	9.11	175.8	5.34	53.4	1.68,1.49	46.7	H^{γ} 1.17; $H^{\delta 1}$ 0.94	C^{γ} 27.3
Thr[51]	125.3	9.10	173.6	5.27	62.1	4.12	71.0	H^{γ} 1.09	C^{γ} 22.1
Ile[52]									
Thr[53]									
Tyr[54]			176.1	4.77	56.7	2.97,2.82	39.9		
Gly[55]	117.0	8.94	174.1	4.12,3.68	47.5				
Ser[56]	123.6	8.67	173.8	4.41	58.7	4.07,3.82	63.9		
Lys[57]	126.1	7.94	174.3	4.56	55.6	2.05,1.89	34.1	H^{γ} 1.45; H^{δ} 1.76; H^{ε} 2.94	C^{γ}25.0; C^{δ}29.2; C^{ε}42.4
Val[58]	128.0	8.45	175.8	4.11	61.7	1.92	33.7	$H^{\gamma 1}$ 0.93; $H^{\gamma 2}$ 0.68	$C^{\gamma 1}$ 21.5; $C^{\gamma 2}$ 21.5
Ile[59]	130.1	9.16			60.0		40.5		
His[60]			173.4	5.60	54.8	3.28,3.06	31.0		
Asn[61]	124.1	8.83	173.5	5.34	52.8	2.60,2.49	44.5		
Glu[62]	123.0	8.88	174.3	5.19	55.2	2.04	32.4	H^{γ} 2.26,2.11	C^{γ} 36.2
Phe[63]	121.3	8.51	173.2	5.13	55.8	3.32,3.25	41.2		
Thr[64]	119.9	8.70	175.5	5.03	61.4	3.94	70.4	H^{γ} 1.24	C^{γ} 22.5

Table 2.3 --- *continued*

Spin	^{15}N	^{1}HN	^{13}CO	$^{1}H^{\alpha}$	$^{13}C^{\alpha}$	$^{1}H^{\beta}$	$^{13}C^{\beta}$	Other ^{1}H	Other ^{13}C
Leu^{65}	131.9	9.62	178.0	4.43	57.0	1.90,1.63	42.3	H^{γ} 0.95; $H^{\delta1}$ 0.94; $H^{\delta2}$ 0.94	C^{γ}26.4;$C^{\delta1}$25.0;$C^{\delta2}$24.0
Gly^{66}	111.1	9.45	173.6	4.42,3.46	45.8				
Glu^{67}	121.4	7.91	175.5	4.83	54.3	2.18, 1.92	32.5	H^{γ} 2.26	C^{γ} 36.1
Glu^{68}	126.9	8.94	175.9	4.43	58.0	2.03,1.98	30.5	H^{γ} 2.16	C^{γ} 37.7
Cys^{69}	126.0	9.30	172.4	5.17	56.4	3.45,3.09	32.5		
Glu^{70}	121.6	8.38	175.4	5.00	55.8	1.92	32.0	H^{γ} 2.17,1.99	C^{γ} 37.8
Leu^{71}	128.7	9.06	175.6	4.59	53.4	1.15,1.05	44.7	H^{γ} 1.33; $H^{\delta1}$ 0.30; $H^{\delta2}$ 0.42	C^{γ}26.5;$C^{\delta1}$25.2;$C^{\delta2}$23.8
Glu^{72}	126.0	9.47			55.8		31.1		
Thr^{73}									
Met^{74}			175.9	3.93	58.7	2.39	32.4		C^{γ} 32.8
Thr^{75}	106.8	7.48	175.8	4.25	61.6	3.87	68.7	H^{γ} 1.11	
Gly^{76}	112.6	7.90	173.9	4.39,3.91	45.2				
Glu^{77}	123.0	7.35	175.5	4.25	56.2	1.82	30.9	H^{γ} 2.23,2.12	C^{γ} 36.4
Lys^{78}	125.8	8.51	176.5	5.31	54.9	1.75,1.53	33.5	H^{γ} 1.51,1.29; H^{δ} 1.61; H^{ε} 3.01	C^{γ}25.5; C^{δ}29.1; C^{ε}42.5
Val^{79}	120.8	8.95	174.2	4.68	58.9	2.08	35.3	$H^{\gamma1}$ 0.80; $H^{\gamma2}$ 0.52	$C^{\gamma1}$ 22.1; $C^{\gamma2}$ 19.9
Lys^{80}	124.8	8.30	176.4	5.07	55.7	1.81,1.71	33.0	H^{γ} 1.40; H^{δ} 1.63; H^{ε} 2.99	C^{γ}25.3; C^{δ}29.1; C^{ε}41.7
Ala^{81}	128.7	8.94	174.9	4.84	51.5	1.25	23.4		
Val^{82}	120.1	8.39	176.1	4.29	61.9	1.93	34.4	$H^{\gamma1}$ 0.88; $H^{\gamma2}$ 0.72	$C^{\gamma1}$ 21.0; $C^{\gamma2}$ 20.8
Val^{83}	136.4	9.74	174.9	4.50	61.5	1.57	31.5	$H^{\gamma1}$ 0.59; $H^{\gamma2}$ -0.10	$C^{\gamma1}$ 22.0; $C^{\gamma2}$ 18.7
Lys^{84}	127.3	8.89	175.6	4.94	54.6	1.79,1.70	36.6	H^{γ} 1.36; H^{δ} 1.70; H^{ε} 2.96	C^{γ}25.3;C^{δ}29.7;C^{ε} 42.3
Met^{85}	121.7	8.77	177.3	5.49	54.2	2.38,2.02	32.3	H^{γ} 2.80,2.62	C^{γ} 32.4
Glu^{86}	128.5	8.66	175.9	4.61	55.9	1.92,1.76	32.3	H^{γ} 2.18,2.12	C^{γ} 36.8
Gly^{87}	115.0	8.47	173.9	4.22,3.82	45.7				
Asp^{88}	120.2	8.56	178.0	4.75	55.3	2.73	42.0		
Asn^{89}	116.0	8.15	174.3	5.17	53.3	3.80,2.85	40.0		
Lys^{90}	119.6	7.37	175.5	5.95	55.0	2.15,1.59	36.5	H^{γ}1.19;H^{δ}1.56;H^{ε}2.89	C^{γ}25.3;C^{δ}29.7;C^{ε}44.7
Met^{91}	122.5	8.89	175.1	5.29	55.3	2.12,2.05	32.5	H^{γ}1.74	
Val^{92}			178.3	5.30	60.6	2.03	35.8	$H^{\gamma1}$0.95	$C^{\gamma1}$ 21.1
Thr^{93}	121.6	8.87	172.0	4.84	61.3	4.10	69.3	H^{γ}0.95	C^{γ} 18.2
Thr^{94}	119.6	8.03	173.2	5.46	59.8	4.04	71.5	H^{γ} 1.10	C^{γ} 21.1
Phe^{95}	122.9	8.09	173.6	4.86	56.1	3.28,2.74	39.9		
Lys^{96}	121.3	9.40	175.7	3.93	56.5	2.18,1.87	30.4	H^{γ}1.67,1.59;H^{δ}1.79,1.71;H^{ε}3.03	C^{γ}25.4;C^{δ}28.9;C^{ε}41.7
Gly^{97}	106.9	8.43	173.7	4.04,3.54	45.5				
Ile^{98}	125.5	8.38	175.9	4.42	60.4	1.50	39.2	$H^{\gamma1}$1.48; $H^{\gamma2}$ 0.77; H^{δ} 0.68	$C^{\gamma1}$28.0;$C^{\gamma2}$18.2;C^{δ}18.0
Lys^{99}	128.8	8.12	175.7	4.76	55.5	1.84,1.71	34.1	H^{γ}1.44,1.30;H^{δ}1.63; H^{ε}2.84	C^{γ}25.4;C^{δ}29.5;C^{ε}42.4
Ser^{100}	124.4	8.97	173.6	5.47	55.8	3.80,3.42	64.4		
Val^{101}	130.5	9.02	175.8	4.71	61.7	2.00	35.0	$H^{\gamma1}$ 0.89; $H^{\gamma2}$ 0.73	$C^{\gamma1}$21.1; $C^{\gamma2}$ 21.2
Thr^{102}	128.8	9.18	172.2	5.01	61.9	3.83	69.9	H^{γ} 0.99	C^{γ} 25.5
Glu^{103}	129.8	9.11	174.4	5.06	54.4	1.71	33.4	H^{γ} 2.08,2.01	C^{γ} 37.0
Phe^{104}	128.2	8.79	175.1	4.58	57.3	2.93,2.77	40.4		
Asn^{105}	125.7	8.29	175.3	5.04	52.4	2.84,2.58	40.4		
Gly^{106}			174.4	4.23,3.60	47.8				
Asp^{107}	128.7	8.77	175.2	4.82	54.5	2.98,2.91	41.7		
Thr^{108}	114.3	7.77	173.6	5.37	61.0	4.12	71.9	H^{γ} 1.17	C^{γ} 21.3
Ile^{109}									
Thr^{110}			173.8	5.04	61.6	3.93	70.6	H^{γ} 1.05	C^{γ} 21.4
Asn^{111}	129.8	9.31	173.6	5.72	52.0	2.59,2.49	43.0		
Thr^{112}	122.4	9.08	174.1	5.09	60.8	3.86	70.4	H^{γ} 1.00	C^{γ} 22.1
Met^{113}	127.9	9.19	174.0	5.45	54.8	1.90,1.76	37.3	H^{γ} 2.56,2.36	C^{γ} 33.2
Thr^{114}	120.5	8.81	173.6	5.31	61.6	4.00	70.8	H^{γ} 1.20	C^{γ} 22.3
Leu^{115}	132.2	8.92	176.2	4.69	54.2	1.73,1.30	44.9	H^{γ} 1.41; $H^{\delta1}$ 0.53; $H^{\delta2}$ 0.70	C^{γ}27.7;$C^{\delta1}$26.0;$C^{\delta2}$23.2
Gly^{116}	119.7	9.06	174.4	3.96,3.63	47.6				
Asp^{117}	128.2	8.64	175.8	4.64	54.1	2.72,2.62	41.1		
Ile^{118}	124.5	8.31	174.4	4.09	61.7	2.26	39.1	$H^{\gamma1}$1.72,1.09;$H^{\gamma2}$1.00;H^{δ}0.82	$C^{\gamma1}$27.3;$C^{\gamma2}$18.1;C^{δ}13.8
Val^{119}	129.3	8.34	176.2	4.69	61.5	2.00	32.7	$H^{\gamma1}$ 0.89; $H^{\gamma2}$ 0.74	$C^{\gamma1}$ 20.2; $C^{\gamma2}$ 21.5
Tyr^{120}	133.2	9.24	174.1	5.25	54.8	2.58,2.10	39.8		
Lys^{121}	131.9	8.10	174.4	5.12	54.6	1.55,1.47	37.2	H^{γ}1.24,1.10;H^{δ}1.47;H^{ε}2.71	C^{γ}25.4;C^{δ}29.7;C^{ε}41.9
Arg^{122}									
Val^{123}			176.1	4.91	61.9	2.08	33.7	$H^{\gamma1}$ 0.90	$C^{\gamma1}$ 21.0
Ser^{124}	125.0	9.35	171.6	5.47	57.6	3.52,3.45	65.7		
Lys^{125}	125.0	8.76	175.6	5.45	54.2	1.90,1.77	36.6	H^{γ} 1.54; H^{δ} 1.72; H^{ε} 2.99	C^{γ}24.9;C^{δ}29.3;C^{ε}42.4
Arg^{126}	129.3	8.88	175.8	4.28	57.6	1.77	31.6	H^{γ} 1.66,1.41; H^{δ} 3.39,3.18	C^{γ} 27.3; C^{δ} 43.8
Ile^{127}	132.2	8.40	180.9	4.21	63.0	1.86	40.2	$H^{\gamma1}$1.29,0.87;$H^{\gamma2}$0.93;H^{δ}0.84	$C^{\gamma1}$27.3;$C^{\gamma2}$18.7;C^{δ}14.6

CHAPTER 3

EXCHANGE STUDIES ON APO- AND HOLO- LFABP

3.1 Introduction

Proteins are built up of amino acid residues. The protons that are bound to nitrogen, oxygen, and sulfur atoms are usually called labile protons, meaning that they have the potential to exchange with water molecules in aqueous solution. Among the labile protons, only nitrogen-attached protons are observable by ^{15}N-edited NMR techniques. Using two-dimensional ^{1}H-^{15}N HSQC NMR spectroscopy, site-specific information on solvent accessibility, hydrogen bonding between β-strands, and protein-ligand interactions may be obtained. Two methods, H_2O/D_2O exchange and H_2O-selective inversion experiments, were used in our rat liver FABP exchange studies. The first one measures the decay of amide signals with the addition of D_2O to the lyophilized protein sample, and the second measures the magnetization transfer from water to amide protons. The H_2O/D_2O exchange experiment measures exchange rate on the time scale of hours, whereas the H_2O magnetization transfer experiment measures on the millisecond time scale. The exchange rates were calculated for 42 residues of apo-LFABP.

3.2 NMR Sample Preparation

^{15}N-labeled apo-LFABP in pH 6.0 phosphate buffer was provided by Professor Judith Storch's research group at Rutgers University. The sample were concentrated with a Centricon-10 ultrafiltration (Amicon) to ~500 μl and 5% D_2O added for the H_2O magnetization transfer experiments. For the H_2O/D_2O exchange experiments,

lyophilization techniques were used to condition both apo and holo forms of the protein. Before lyophilization, protein samples were exchanged into ammonium bicarbonate solution (~ pH 8) to ensure that no non-vaporizing salts remain in the samples after lyophilization. The preparation of holo-LFABP, a complex of $^{13}C/^{15}N$-LFABP with unlabeled oleate (ratio 1:3), will be described in Chapter 5. The procedure for lyophilization is as follows: (1) The protein was exchanged with 50 mM ammonium bicarbonate solution using PD-10 columns (Pharmacia Biotech); (2) approximately 3.5 ml of protein eluent was collected in a small wide bottom tube which was covered with a Kimwipe and rubber band; (3) the tube was immersed in an isopropanol-dry ice mixture and swirled evenly to cause rapid freezing; (4) after the protein was nicely frozen, the tube was put on a vacuum line and lyophilized overnight.

Once the NMR experiment was set up, D_2O-based phosphate buffer was added to the lyophilized protein and spectra were acquired as quickly as possible. In practice, the first HSQC spectrum was acquired about 20 min after the addition of D_2O and the intervals thereafter between each spectral acquisition were in the time range of minutes to hours.

3.3 Experiments

3.3.1 H_2O/D_2O exchange experiments[73]

With the addition of D_2O buffer to the lyophilized protein, the labile protons that are solvent accessible and lacking protection from the secondary structure will be exchanged by deuterium and no longer be observed in the $^{1}H-^{15}N$ HSQC spectra. Those residues are considered as having fast amide exchange rates (10 msec to sec time-scale,

or $k > 60\ min^{-1}$). For residues having a slow amide exchange rate (min time-scale, or $k < 0.2\ min^{-1}$), the amide signals are observable in ^{1}H-^{15}N HSQC spectra but their intensities may be diminished. The loss of intensity is monitored as a function of exchange time and fit to a single-exponential equation (Eq. 1):

$$I = A + B \exp(-kt) \qquad \text{when } k < 0.2\ min^{-1} \qquad (1)$$

A pulsed-field-gradient (PFG) sensitivity-enhanced ^{1}H-^{15}N HSQC experiment [34,55] (Section 2.3.3.2) was used for measurement of H_2O/D_2O exchange rates for apo-LFABP at pH 6.0 and 30 °C. A total of 11 2D spectra were acquired consecutively over 54 hours with acquisition times of 26 min (1st exp), 40 min (2nd exp), 80 min (3rd exp), and 160 min (4th to 11th exp), respectively. Exchange rates were calculated for 22 residues of apo-LFABP. The first pfg-HSQC spectrum was acquired 34 min after dissolution of the protein in D_2O.

For a sample of oleate-bound holo-LFABP at pH 7.0, a fast HSQC (FHSQC) experiment[74], which is designed to avoid gradient saturation of most of the water signal by the WATERGATE sequence, was used to monitor H_2O/D_2O exchange. A total of 16 2D FHSQC spectra were acquired consecutively over 7 days with acquisition times of 20 min (1st and 2nd exp), 41 min (3rd and 4th exp), 82 min (5th and 6th exp), and 164 min (7th to 16th exp), respectively. The first FHSQC spectrum was acquired 20 min after dissolution of the protein in D_2O. **Fig. 3.1** illustrates the amide signal decay in oleate-bound holo-LFABP ^{1}H-^{15}N HSQC spectra after addition of phosphate buffer in D_2O. The indicated times refer to the period between the time at which D_2O addition was begun and the middle of the spectral acquisition time. After 5 hours, the number of

remaining amide signals was nearly stable, with proton exchange limited by solvent inaccessibility, protection by the secondary structure, and interaction with the ligands.

3.3.2 H_2O-selective experiments[75]

For the residues undergoing fast exchange ($k > 60$ min^{-1}), a water-selective inversion experiment was used to obtain the exchange rate. This experiment replaces dissolution in a deuterated buffer with selective inversion of magnetization associated with water and effectively labels water protons for a time on the order of the water spin-lattice relaxation time. It is derived from the 3D NOESY-HMQC experiment[76,77,78] through the use of selective excitation of the water resonance[79] and pulsed-field-gradients (PFG) to select for amide protons coupled to ^{15}N nuclei[80], and by reduction of the 3D experiment to a 2D analog that contains information primarily about water molecules. The selective inversion pulse is followed by a mixing period, during which protons at the position of the water resonance interact with the protons of the protein through cross relaxation and/or chemical exchange (NOESY mixing scheme) or through scalar coupling (TOCSY mixing scheme). Magnetization that is transferred from water to protein amide sites is then detected using a PFG-enhanced version of the HMQC pulse sequence[80]. As the mixing time increases in a H_2O-selective/HMQC experiment, the intensities of the HMQC cross-peaks are built up. The relationship between intensity and mixing time can be represented by Eq. (2):

$$I = A - A \exp(-kt) \qquad \text{when } k > 60 \text{ min}^{-1} \qquad (2).$$

However, for those residues with α-proton chemical-shift degeneracies with water or hydroxyl protons (Ser and Thr), the H_2O-selective/HMQC experiment may create

erroneous cross-peaks. The reasons are as follows: (1) if α-protons of i and i-1 residues are close to the water resonance, excitation of these α-protons might cause magnetization transfer to the amide protons, resulting in erroneous measurement of H_2O-to-NH transfer; (2) since the NOESY scheme also measures exchange and both Ser-OH and Thr-OH exchange freely with water, the measurement of –OH to NH transfer might interfere with the magnetization transfer between water and amide protons.

A total of 10 2D water-selective inversion/HMQC experiments were conducted on apo-LFABP at pH 6.0 and 30 °C with mixing times of 20, 40, 60, 80, 100, 125, 150, 175, 200, and 250 msec, respectively. A 2-G/cm z-gradient pulse was applied throughout the mixing time. **Fig. 3.2** shows the apo-LFABP amide signals' growth in ^{1}H-^{15}N HMQC/water-selective experiments as the mixing time is increased. Exchange rates were calculated for 20 residues of apo-LFABP.

3.4 Results and Discussion

3.4.1 Amide exchange rates

By using Eqs (1) and (2), amide exchange rates for slow exchange ($k < 0.2$ min^{-1}) or fast exchange ($k > 60$ min^{-1}) cases were calculated for 42 residues of apo-LFABP based on the results of H_2O/D_2O exchange (22 residues) and water-selective/HMQC experiments (20 residues), respectively. Other residues are either in the intermediate exchange regime (0.2 min^{-1} $< k < 60$ min^{-1}), have unobservable amide signals in the HSQC spectrum (1 N-terminal residue, 2 proline, and 15 unassigned residues), or have ambiguous water-selective/HMQC measurements (6 residues have their α-protons close to water resonance and 2 residues have Ser and/or Thr as the previous residue), so their

rates are either inaccessible or suspect. Examples of curve fitting using Eqs. (1) and (2) are shown in **Fig. 3.3**. The exchange rates obtained from curve fitting are represented as a bar plot along the protein sequence and shown in **Fig. 3.4**. The secondary structural elements shown on the top of the plot were derived by the Chemical-Shift Indices (CSI) method[66] based on the ^{1}H, ^{13}C, and ^{15}N assignments for apo-LFABP (Section 2.6.2). As expected, the residues with fast exchange rates are mainly located in loop regions, and residues with slow exchange rates are mostly located within the secondary structural elements. However, Lys^{78}, Lys^{80}, and Val^{82} have fast exchange with solvent although they are located within the βF-strand (residue 76-86). Although NMR does not provide rationale for this observation, prior X-ray results[25] on oleate-bound holo-LFABP suggest that βF actually involves βF' (residue 78-79) and βF'' (residue 84-86) strands, meaning that a loop (residue 80-83) is inserted into the βF strand. Based on the similarities of the secondary structures on apo- and holo-LFABP evidenced by NMR and X-ray studies, respectively (**Table 5.5**), it is reasonable to conclude that apo-LFABP also contains a loop within the βF strand.

The H_2O/D_2O exchange experiment was also carried out for oleate-bound holo-LFABP; a detailed comparison of the exchange rates between apo and holo forms of LFABP appears in Section 3.4.4.

3.4.2 Solvent accessibility

Residues undergoing fast exchange are solvent accessible, and their amide signals disappear rapidly from ^{1}H-^{15}N HSQC spectra after the addition of D_2O. For apo-LFABP, nearly 80% of the amide protons were exchanged with deuterium within 47 min after the

addition of phosphate buffer in D_2O, suggesting an unusual accessibility to solvent compared with apo forms of heart and intestinal FABP. [22,27,81] For holo-LFABP, nearly 60% of the amide protons were exchanged with deuterium within 30 min after dissolving in D_2O. Clearly, the bound oleates make the protein less accessible to solvent. The decrease in the number of amide signals for both apo- and holo-LFABP is shown in **Fig. 3.5**.

3.4.3 Hydrogen bonding networks

Secondary structural elements, either α-helices or sheets of β-strands, are typically held together by hydrogen bonds in the protein. The amide protons involved in hydrogen bonds are not easily exchanged by deuterium, thus their signals will be retained in the ^1H-^{15}N HSQC spectra after the addition of D_2O. Based on NOE constraints from ^{15}N-edited 3D and/or $^{15}N/^{13}C$-edited 4D NOESY experiments, hydrogen bonds involving the amide protons can also be deduced from HN(i)-HN(j) and HN(i)-H^{α}(j) connectivities. **Fig. 3.6** shows hydrogen bonds linking β-strands A-D, derived from NOEs for a complex of $^{13}C/^{15}N$ dual-labeled LFABP with unlabeled oleate (ratio 1:2). The amide protons drawn with circle have two characteristics: (1) their amide signals remained in the ^1H-^{15}N HSQC spectra a week after the addition of D_2O-based phosphate buffer (pH 7.0); (2) they displayed cross β-strand NOE signals in NOESY experiments (represented by the patterns  or ) (The basis for the secondary structure derivation and NOE assignments for the holo-protein will be presented in Chapter 5.)

From **Fig. 3.6**, it is clear that the results from the H_2O/D_2O exchange study are consistent with those from the NOE assignments. For example, based on the H_2O/D_2O

exchange result, the amide proton (H) signal of Tyr^{7} remained, suggesting that it formed a hydrogen bond with the carbonyl oxygen (O) of Ser^{39}. On the other hand, from the NOESY results, NOE connectivities HN(7)-HN(39) and HN(7)-H^{α}(40) (pattern 

) indicate hydrogen bond formation for N-H^{7}---^{39}O-C. Nevertheless, there are notable exceptions: hydrogen bonds of N-H^{5}---^{41}O-C, N-H^{9}---^{37}O-C, N-H^{39}---^{7}O-C, N-H^{44}---^{47}O-C, N-H^{53}---^{38}O-C, and N-H^{54}---^{57}O-C were predicted from NOE assignments but the amide signals of Gly^{5}, Val^{9}, Ser^{39}, Glu^{44}, Thr^{53}, and Tyr^{54} disappeared after a week. The reasons may be as follows: residues Val^{9}, Glu^{44}, and Tyr^{54} are located at the ends of β-strands A, B, and C, respectively. Even through the spatial distances of their amide protons to other amide and α protons are small enough to produce NOESY signals ($d < 5$ Å), those residues are very flexible and may not from stable hydrogen bonds since they are close to the loop. For residues Ser^{39} and Thr^{53}, their amide resonances are unassigned in the apo-protein presumably due to their significant flexibility, multiple conformations, and proximity to the loop. On the other hand, residues Ile^{52} and Ile^{59} have amide signals that remained after a week but their involvement in amide hydrogen bonds was not confirmed by the NOESY results (that is, no pattern  was observed). This anomaly is attributed to ambiguity in the NOE assignment of HN(52)-HN(59), since the HN resonances for Ile^{52} and Ile^{59} are 9.10 and 9.23 ppm, respectively. The distance for HN(52)-HN(59) is 2.95 Å based on X-ray result [25], so the NOE should be large.

3.4.4 Protein-ligand interaction

H_2O/D_2O exchange experiments provide information not only on solvent accessibility and hydrogen bonds between secondary structural elements, but also on the

interaction between the protein and ligand. **Fig. 3.7** illustrates the location of residues with amide signals that disappeared and remained for both apo- (panel a) and holo-LFABP (panel b). This presentation makes it clear that the binding of the ligands was accompanied by a dramatic decrease in the number of disappearing amide signals (labeled "1") and an increase in the number of amide signals that are resistant to H_2O/D_2O exchange (labeled "2").

Residues with amide signals that disappeared immediately in the apo-protein but not in the holo-protein when the first ^{1}H-^{15}N HSQC spectrum was examined may have their hydrogen bonding network strengthened by the presence of the fatty acid ligand. Similarly, residues with amide signals that remained for 24 hours after the addition of D_2O exclusively for the holo-protein may also be deduced to have stronger hydrogen bonding in the presence of the ligand. Those two observations should be consistent with each other to some extent. The strengthening of hydrogen bonding network around these residues may or may not be directly related to the binding of ligand, but those residues could be involved in the ligand binding. The two groups of residues are grouped together in **Table 3.1**. For comparison purposes, residues which are nearby and/or interacting with the two oleates as judged from an X-ray study[25] are also listed in **Table 3.1**. Residues in **bold** show the consistency of the H_2O/D_2O exchange results with the X-ray data.

The H_2O/D_2O exchange study for apo-LFABP was presented at the 36th Eastern Analytical Symposium (Somerset, NJ, 1997).

Table 3.1 Residues involved in ligand binding, deduced from an H_2O/D_2O exchange study for rat liver FABP. Residues with stars (*) are unassigned for apo-LFABP. Residues in **bold** show the consistency of the H_2O/D_2O exchange results with the X-ray data.

Residues whose amide signals disappeared in first 45 mins after the addition of D_2O for apo-LFABP but not for holo-LFABP	F18, K20, **L28**, **G32**, G37, E40, **I41**, **I59**, **N61**, E62, **F63**, **T93**, F95, V101, **T102**, E103, **M113**, I118, and S124.
Residues whose amide signals remained 24 hours after the addition of D_2O for holo-LFABP but not for apo-LFABP	F18, **L28**, E40, **I41**, K49, T51, **I52***, **I59**, **N61**, E62, **F63**, A81, **T93**, V101, **T102**, E103, **M113**, I118, and S124.
Residues which are nearby and/or interacted with the two oleates based on X-ray results	**L28**, **G32**, I35, **I41**, **I52***, G55, K57, **I59**, **N61**, **F63**, F72, T73*, M74*, **T93**, **T102**, **M113**, and R122*.

Figure 3.1 The amide region of selected spectra from H_2O/D_2O exchange experiments on a complex of $^{13}C/^{15}N$-LFABP with unlabeled oleate (ratio 1:2) at 30 ∘C. Panel A is an FHSQC spectrum obtained in H_2O phosphate buffer (pH 7.0). Panels B, C, and D are FHSQC spectra obtained 0.5 hr, 4.5 hr, and 3 days after addition of D_2O phosphate buffer (pH 7.0).

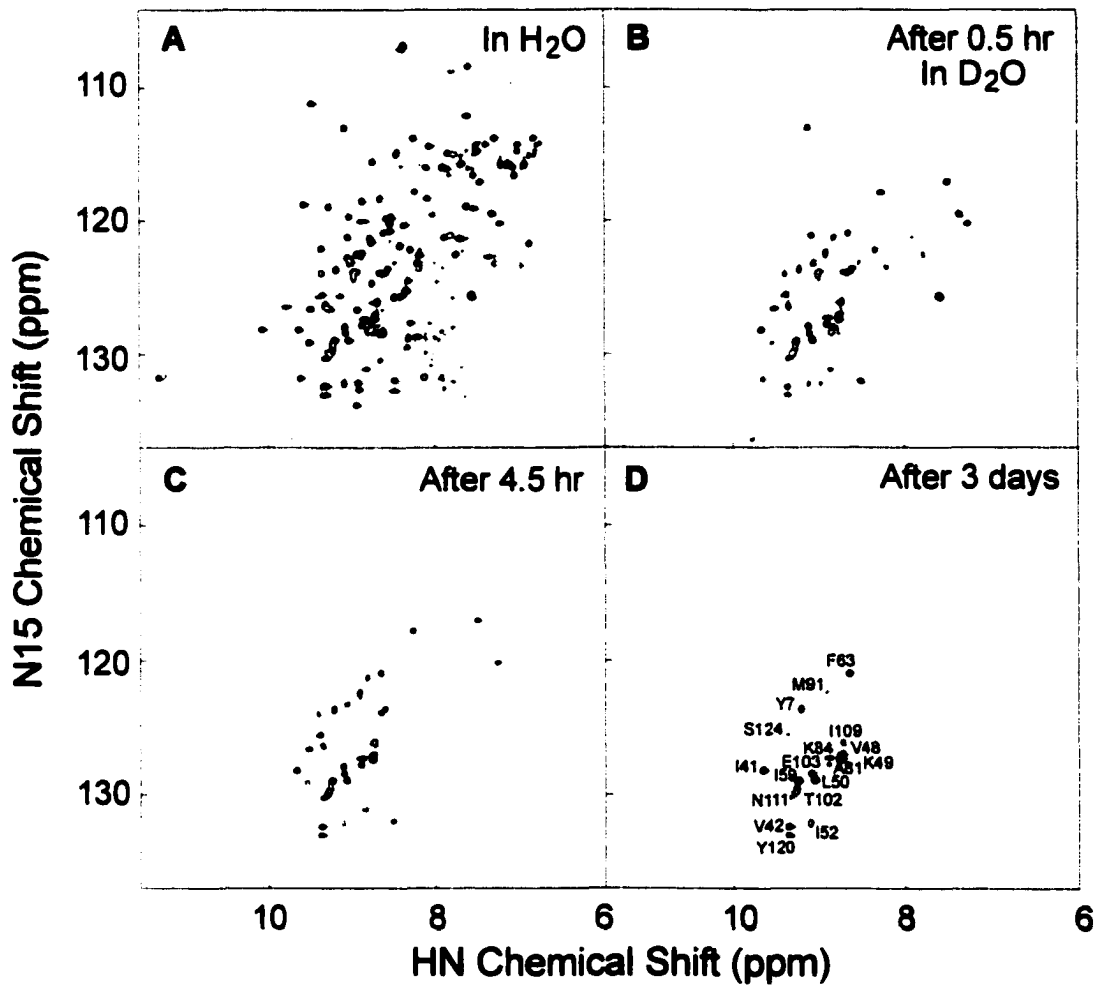

Figure 3.1

Figure 3.2 Amide region of ^{1}H-^{15}N selective inversion/exchange HMQC spectra, showing the transfer of magnetization from protons at the chemical shift of water to amide protons of the apo form of ^{15}N-LFABP at pH 6.0 and 30 °C. Experiments with mixing times of 40ms, 100ms, and 250ms are displayed.

Figure 3.3 Curve fitting to obtain amide proton exchange rate constants for the apo form of ^{15}N-labeled LFABP. The left panel shows slow exchange measured by the H_2O/D_2O exchange experiment. The right panel shows fast exchange measured by the H_2O-selective experiment.

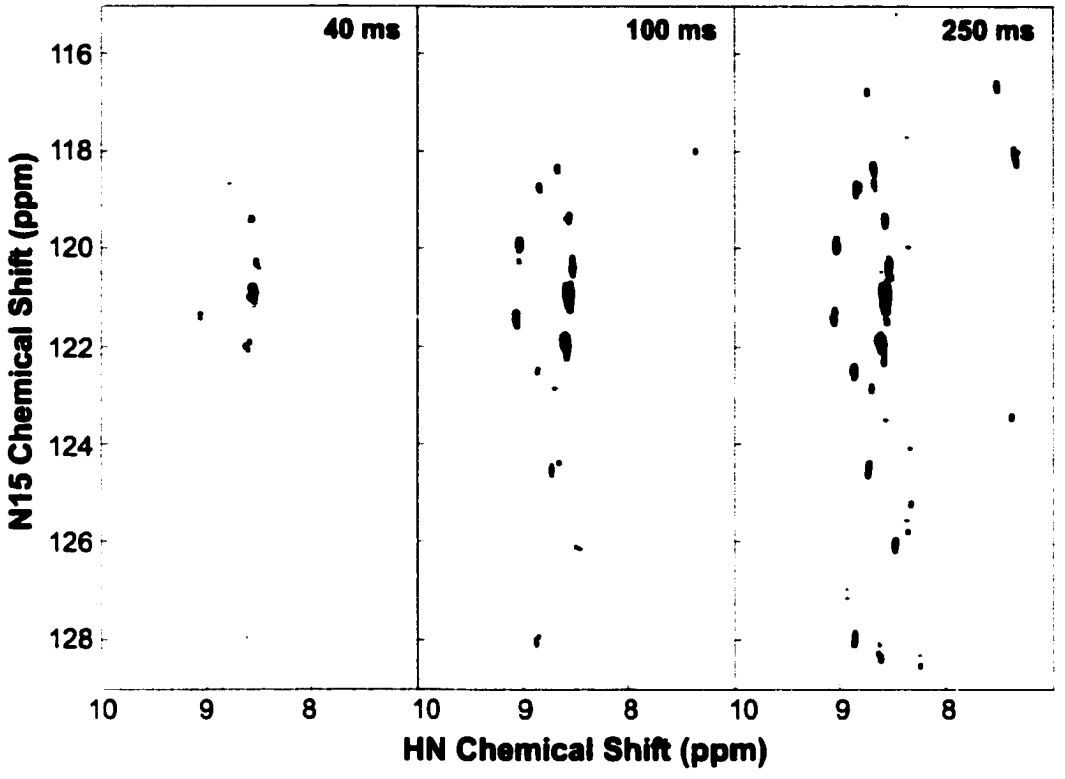

Figure 3.2

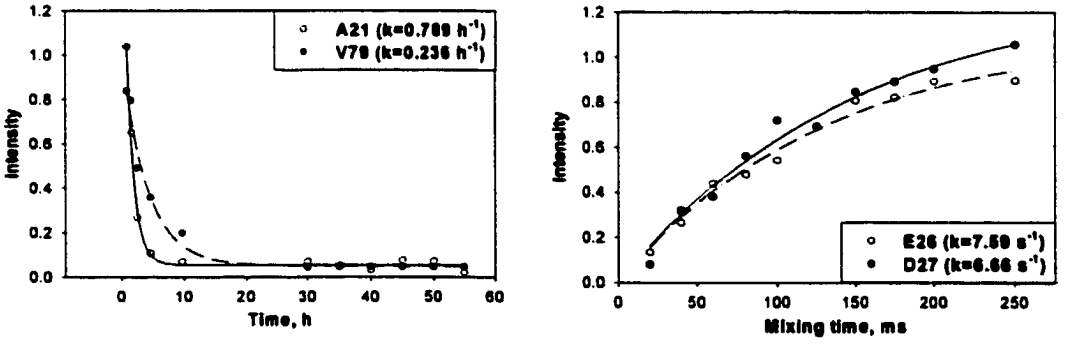

Figure 3.3

Figure 3.4 Backbone amide proton exchange rate constants versus residue number measured for the apo form of ^{15}N-LFABP from H_2O/D_2O exchange experiments (bars below dotted line, $k < 0.2$ min^{-1}) and selective water inversion experiments (bars above dashed line, $k > 60$ min^{-1}). Intermediate exchange rates (between two lines) are not measured by either method.

Figure 3.5 The percentage of residues remaining versus the time after addition of phosphate buffer in D_2O. The dashed line shows the decay of ^{1}H-^{15}N HSQC signals with an apo form of ^{15}N-labeled LFABP (pH 6.0). The solid line shows the decay of ^{1}H-^{15}N HSQC for a complex of dual-labeled LFABP and unlabeled oleate (ratio 1:2 and pH 7.0).

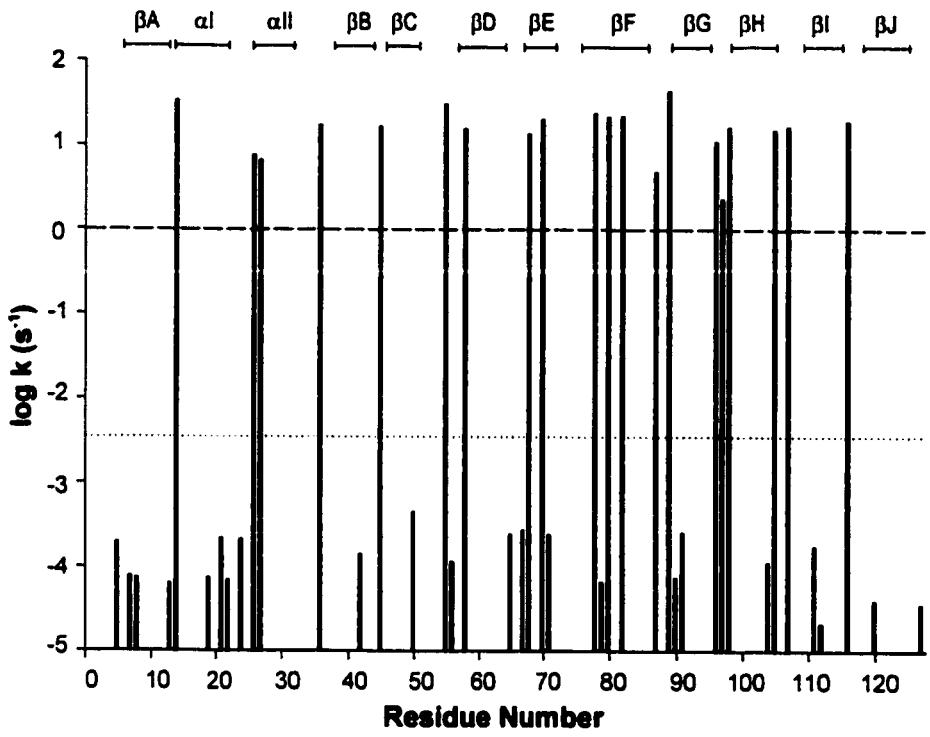

Figure 3.4

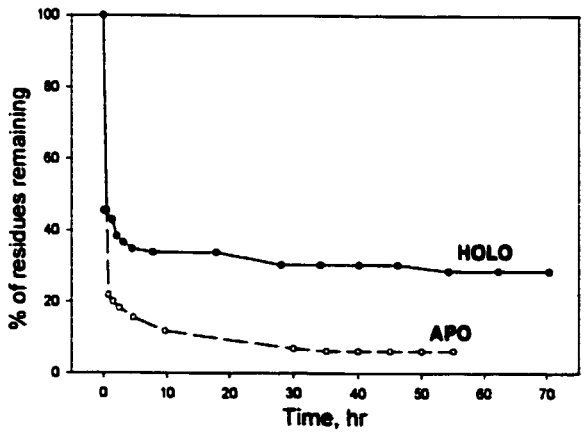

Figure 3.5

Figure 3.6 Hydrogen-bonding network derived from NOE connectivities of β-strands A-D in a complex of $^{13}C/^{15}N$-LFABP with unlabeled oleate (ratio 1:2). The amide protons drawn with circle correspond to the remaining peaks in a ^{1}H-^{15}N FHSQC experiment acquired one week after H/D exchange with D_2O-based phosphate buffer (pH 7.0). NOE assignments for the holo-protein will be presented in Chapter 5.

Figure 3.7 Locations of H_2O/D_2O exchange for (a) apo-LFABP at pH 6.0 and (b) oleate-bound holo-LFABP at pH 7.0, based on the x-ray structure of oleate-bound holo-LFABP[25]. Residues labeled "1" undergo disappearance of their amide proton signals in ^{1}H-^{15}N HSQC spectrum after (a) 47 min, and (b) 30 min subsequent to the addition of phosphate buffer in D_2O. Residues labeled "2" have amide proton signals that remain in the ^{1}H-^{15}N HSQC spectra after (a) 2 days, and (b) one week after the addition of phosphate buffer in D_2O. Residues in black are either unassigned (apo: 15 of 124 are not assigned; holo: 1 of 124 is not assigned) or undergo disappearance of their amide proton signals in the ^{1}H-^{15}N HSQC spectra during the time periods of (a) 47 min to 2 days, and (b) 30 min to one week, respectively. The numbers shown on panel (a) are the residue numbers in the protein sequence.

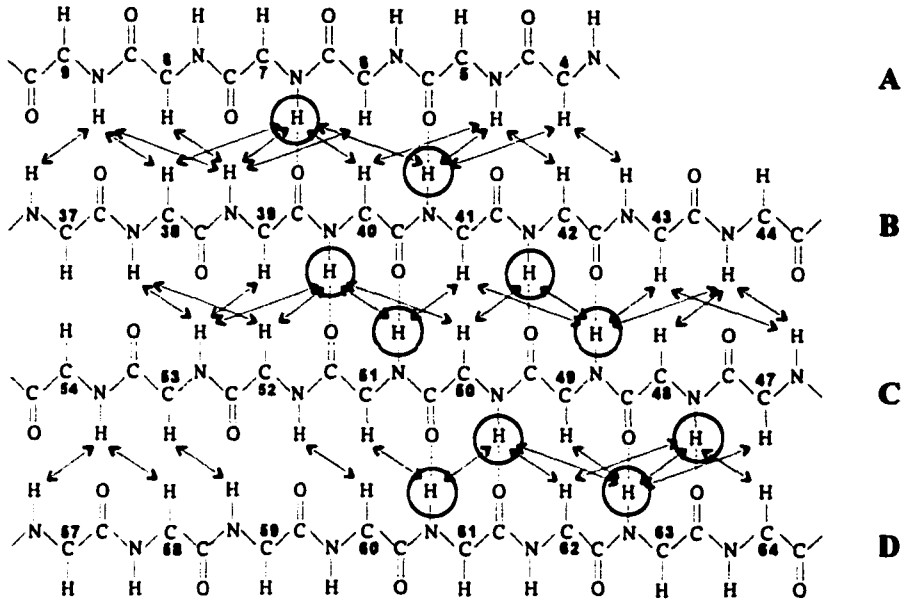

Figure 3.6

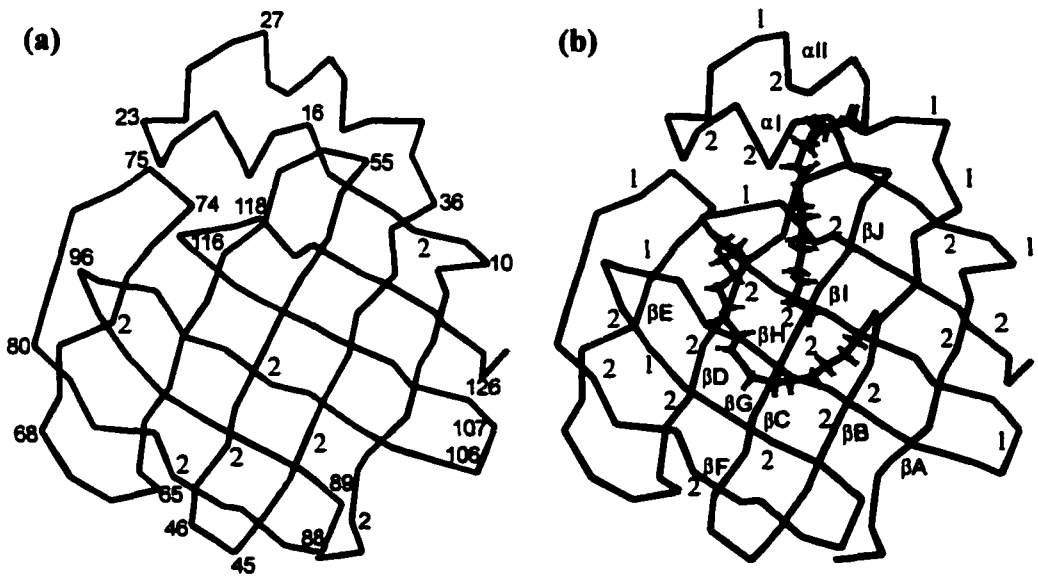

Figure 3.7

CHAPTER 4

PROTEIN-LIGAND INTERACTION AND BINDING PHENOMENA

4.1 Introduction

NMR spectroscopy has proven to be a useful tool for the analysis of protein-ligand interactions in recent years. Information on protein-ligand interactions (binding affinity, binding site, stoichiometry, and bound conformation) can be derived from NMR parameters such as chemical shifts, relaxation parameters (R_1 and R_2), nuclear Overhauser effects (NOEs), linewidths, and intensities.

Rat liver fatty acid binding protein (LFABP) is a member of the intracellular lipid-binding protein (iLBP) family. It can reversibly and non-covalently bind fatty acid (FA) to enhance the FA's solubility. As noted in Chapter 1, LFABP differs from the other FABPs because of its ability to bind at least two FA rather than one[16,82] and its diffusion-limited (rather than collisional) transport mechanism[18]. **Fig. 4.1** compares the visual appearance of three samples: a) 0.50 mM oleate in pH 7.0 phosphate buffer; b) 0.26 mM LFABP with 0.50 mM oleate (ratio 1:2) at pH 7.0; and c) 0.17 mM LFABP with 1.20 mM oleate (ratio 1:8) at pH 7.0. The figure shows that oleate alone is insoluble in the buffer even at the low concentration of 0.50 mM, but the complex of oleate with LFABP is soluble with up to 8 equivalents of oleate. This observation confirms that LFABP possesses remarkable functions, which will greatly enhance aqueous solubility and thus facilitate the transport of fatty acids.

In this protein-ligand titration study, the stoichiometry of FA binding to LFABP will be examined by viewing the protein and the ligand, respectively. Three series of

titration experiments were carried out: (1) ^{15}N-LFABP titrated with unlabeled oleate; (2) ^{15}N-LFABP titrated with [U-^{13}C]-palmitate; and (3) ^{15}N-LFABP titrated with [U-^{13}C]-oleate.

4.2 NMR Titration Studies --- Series I: ^{15}N-LFABP Titrated with Unlabeled Oleate

4.2.1 Sample preparation

Unlabeled sodium oleate salt was obtained from Sigma (St. Louis, MO), and ^{15}N-labeled rat LFABP was provided by Professor Judith Storch's group at Rutgers University. A 10 mM stock solution of sodium oleate in H_2O at pH 9.2 was prepared to permit direct addition to 440 μl of 0.17 mM apo ^{15}N-LFABP in pH 7.0 phosphate buffer in a 5-mm NMR tube. For every equivalent of oleate added to the protein, 7.5 μl of 10 mM oleate was needed. The exact amount was added with the help of a 10-μl syringe and tubing. Six complexes of ^{15}N-LFABP with oleate in ratios of 1:1, 1:2, 1:3, 1:4, 1:6, and 1:8 were prepared for the titration study. After the addition of the sixth equivalent of oleate to the LFABP, the sample still remained clear and pH value was 7.0. With the addition of the eighth equivalent of oleate, a thin layer of white precipitate formed and settled to the bottom of the NMR tube, but the supernatant was still clear and gave well-resolved signals in NMR experiments (see Section 4.2.2).

The concentration of apo-protein in pH 7.0 phosphate buffer (50 mM Na_2HPO_4/NaH_2PO_4, 100 mM NaCl, 50 μM EDTA, and 0.02 % NaN_3) was measured by both the Lowry method[30] (see Chapter 5) and using the UV absorption at 280 nm[31].

4.2.2 Experiments

Unless otherwise stated, data were collected at 30 °C on a four-channel Varian INOVA-600 spectrometer (Varian NMR instruments, Palo Alto, CA) equipped with an indirect-detection triple resonance probe and z-axis pulsed field gradients. In all experiments, the H_2O signal was set on resonance in the proton dimension.

To study the stoichiometry of FA bound to LFABP by viewing the protein, 1D proton and 2D ^{1}H-^{15}N HSQC experiments were carried out on an apo-LFABP sample and six holo-LFABP samples in ratios of 1:1, 1:2, 1:3, 1:4, 1:6, and 1:8 to monitor the proton and nitrogen chemical shifts of the protein. In the 1D proton experiment, water suppression was achieved by the presaturation technique. The 2D ^{1}H-^{15}N HSQC spectra were acquired with sensitivity-enhanced gradient coherence selection (see pulse sequence in **Fig. 2.4**) with a water flip-back pulse to minimize water disturbance[34]. The ^{15}N carrier was set in the middle of the amide region (120.54 ppm). The experiments were carried out with 256 complex points in t_1, 1024 complex points in t_2, and 32 transients.

4.2.3 Results

4.2.3.1 Effect of fatty acid on protein NMR spectra **Figs. 4.2** and **4.3** display selected portions of one-dimensional proton spectra and two-dimensional ^{1}H-^{15}N HSQC spectra for the apo form of ^{15}N-LFABP and its complexes with unlabeled oleate in ratios of 1:1, 1:2, 1:3, 1:4, 1:6, and 1:8, respectively. Several qualitative trends are evident: (1) binding of the fatty acid produces stronger and better-resolved spectral features (more peaks visible, good spectral dispersion, fewer doubled peaks, and narrower linewidth); (2) LFABP is locked into a well-defined structure after two equivalents of FA are added; (3) both the backbone amide and some methyl proton peak positions of the apo-protein

are changed significantly upon adding the oleate; and (4) as more than two equivalents of FA are added, the cross-peaks are further sharpened, but the resonance positions remain essentially the same. Thus the NMR results immediately suggest that internal protein flexibility, which may be substantial in the apo-protein, is diminished dramatically upon binding of fatty acids. Significant changes in the backbone amide peak positions are also indicative of conformational alterations in the holo-protein. Based on observations (2) and (4) above for the backbone amide spectral region of the protein, it may be concluded that LFABP binds at least two oleate molecules. This observation also provides a practical rationale for using the 1 LFABP: 2 oleate complex for subsequent resonance assignments and structural determinations in the holo protein (Chapter 5).

4.2.3.2 Chemical shift and linewidth analysis of protein resonances The average HN linewidths for apo- and holo-proteins with ratios 1:2, 1:3, 1:4, and 1:6 were 34.6, 24.4, 19.4, 18.3, and 17.4 Hz, respectively. The HN linewidth change between apo- and 2 oleate-bound holo-LFABP ($\Delta\nu(0,2)$ were found in the range of 1-52 Hz along the protein sequence). The linewidths of backbone amide protons for the holo-protein with ratios 1:2 to 1:6 were analyzed by VNMR and plotted in **Fig. 4.4**. Upon adding the third equivalent of oleate to the 2 oleate-bound holo-LFABP, the HN linewidths were narrowed by 0-16 Hz ($\Delta\nu(2,3)$ = 0-16). Compared with the linewidth changes $\Delta\nu(3,4)$ of 0-5 Hz and $\Delta\nu(4,6)$ of 0-5 Hz, the larger value of $\Delta\nu(2,3)$ suggests that LFABP could bind a third oleate molecule. **Fig. 4.5** is a site-specific three-dimensional view of the protein and derived from the X-ray structure of oleate-bound holo-LFABP [25]. Residues with amide proton chemical shift differences exceeding $\Delta\nu(2,3) > 10$ Hz are shown in black. Since the black residues are located around the binding cavity and the portal, this

trend again supports the possibility that LFABP binds three molecules of oleate. It should also be noted that X-ray diffraction revealed a fragment of a four-carbon chain near the amino-terminal end of the first LFABP helix, just where the chemical shift analysis showed the blue residues. This feature was attributed provisionally to a third bound oleate molecule with a disordered hydrocarbon tail.

4.3 NMR Titration Studies --- Series II: ^{15}N-LFABP Titrated with [U-^{13}C]-Palmitate

4.3.1 Sample preparation

[U-^{13}C]-palmitic acid was purchased from Cambridge Isotope Labs (Andover, MA), and ^{15}N-LFABP was provided by Professor Judith Storch's group at Rutgers University. A stock solution of 10 mM [U-^{13}C]-palmitic acid in $CDCl_3$ was prepared. A 0.25-ml portion of the solution was exposed under the hood until $CDCl_3$ was completely evaporated and then 10.0-ml of 100 mM $(NH_4)_2CO_3$ were added to obtain a 0.25 mM [U-^{13}C]-palmitate solution in $(NH_4)_2CO_3$ at pH 9.6. A 900-µl solution of 0.46 mM apo ^{15}N-LFABP in phosphate buffer at pH 6.0 (concentration measured as in Section 4.2.1) was exchanged into a 100 mM $(NH_4)_2CO_3$ solution with a PD-10 gel filtration and 3.5-ml of protein eluent was collected. A 5-ml portion of the 0.25 mM [U-^{13}C]-palmitate in $(NH_4)_2CO_3$ was mixed with the 3.5-ml protein eluent. The mixture with protein-to-ligand ratio of 1:3 was stirred overnight at 4 °C and then treated as follows: (1) Centricon-10 ultrafiltration with $(NH_4)_2CO_3$ to remove the unbound palmitate; (2) PD-10 gel filtration column to exchange solvent with a pH 7.0 phosphate buffer; and (3) Centricon-10 ultrafiltration again with a pH 7.0 phosphate buffer to reduce the volume to ~ 250 µl.

After addition of 5 % D_2O by volume, the solution was transferred to a 5-mm Shigemi NMR tube (Shigemi, Allison Park, PA) and stored at 4 °C until use.

4.3.2 Experiments

To study the stoichiometry of FA binding to LFABP by labeling the ligand with ^{13}C, we measured the resonances of the carboxyl, methyl, and α-methylene groups of the [U-^{13}C]-palmitate in the 3 palmitate:holo-protein. The ^{13}C resonances of pH 7.0 ^{15}N-LFABP-bound [U-^{13}C]-palmitate were studied at 10 °C and 30 °C with 1D ^{13}C spectra, 2D ^{1}H-^{13}C HSQC, and constant-time 2D HA-CO correlation from a 3D HCACO experiment [83]. The HSQC data were acquired with 160 complex points in t_1, 1024 complex points in t_2, and using the 'wet' scheme[84] to suppress water. The 'wet' technique uses a series of variable-tip-angle solvent-selective radiofrequency (rf) pulses, where each selective rf pulse is followed by a dephasing field-gradient pulse. The ^{13}C carrier was placed at 45 ppm and the sweep widths in ^{1}H and ^{13}C dimensions were set to 8000 and 9000 Hz, respectively. The CT-HCACO experiments were carried out in two dimensions only to obtain the HA-CO correlation. The ^{13}C carrier was placed at 45 ppm, and the sweep widths were 6000 Hz in ^{1}H and 1800 Hz in CO, respectively. Spectra were acquired with 64 complex points in CO. Water was suppressed with gradient purge pulses.

4.3.3 Results

The results of 1D ^{13}C, 2D ^{1}H-^{13}C HSQC, and 2D HA-CO correlation (from a 3D HCACO experiment) on ^{15}N-LFABP-bound [U-^{13}C]-palmitate at 10 °C are shown in **Fig.**

4.6. Two sets of α-CH_2 and ω-CH_3 resonances were observed in this holo-protein, indicating that one LFABP binds at least two palmitate molecules in different electronic environments. Nevertheless, only a single carboxyl resonance was observed in both ^{13}C and HCACO spectra, which is consistent with previous 1D ^{13}C NMR studies[16,82].

4.4 NMR Titration Studies --- Series III: ^{15}N-LFABP Titrated with [U-^{13}C]-Oleate

4.4.1 Sample preparation

[U-^{13}C]-oleic acid was purchased from Isotec (Miamisburg, OH), and ^{15}N-LFABP was produced by Professor Judith Storch's group at Rutgers University. A 15-µl portion of [U-^{13}C]-oleic acid solution was neutralized with 0.1 N sodium hydroxide to prepare a 10 mM sodium oleate salt stock solution at pH 9.5. A 550-µl solution of 0.26 mM apo-^{15}N-LFABP in pH 7.0 phosphate buffer (concentration measured as in Section 4.2.1) was titrated with 7.2-µl portions of 10 mM [U-^{13}C]-oleic acid in 0.1 N NaOH to obtain holo-protein samples with molar ratios of 1:0.5, 1:1, 1:1.5, 1:2, 1:3, and 1:4, respectively.

4.4.2 Experiments

Experiments including 1D proton, 1D carbon, 2D constant time (CT)-C13-HSQC, 2D HMQC-TOCSY, and 2D ^{1}H-^{13}C HSQC NMR were carried out to complete the ^{1}H and ^{13}C resonance assignments of 2-mM [U-^{13}C]-oleate in pH 7.0 phosphate buffer. Both C13-HSQC and HMQC-TOCSY experiments were acquired with 128 complex points in t_1, 1024 complex points in t_2 and total running times 4 h and 7.7 h, respectively. The 'wet' water suppression scheme[84] was used to suppress water, and the ^{13}C carrier frequency was set at 80 ppm.

^{15}N-LFABP at pH 7.0 and 10 °C was titrated with [U-^{13}C]-oleate to form complexes with ratios of 1:0.5, 1:1, 1:1.5, 1:2, 1:3, and 1:4. The titration was monitored by C13-HSQC, HCACO, and HCCH-COSY experiments[53]. The experiments were acquired with 160, 128, and 128 complex points in t_1, respectively, and 1024 complex points in t_2, using 32 transients for signal averaging.

4.4.3 Results

4.4.3.1 Assignment of [U-^{13}C]-oleate A 2-mM [U-^{13}C]-oleate solution in pH 7.0 phosphate buffer was used to make complete ^{1}H and ^{13}C assignments. The 1D proton spectrum clearly showed the ethylenic proton resonance at 5.26 ppm. The 1D carbon spectrum showed a carbonyl signal at 182.0 ppm and an ethylenic carbon resonance at 132.0 ppm. The (CT)-C13-HSQC spectrum gave the assignments for α-CH_2 (38.0 & 2.18 ppm) and ω-CH_3 (16.5 & 0.84 ppm), since their cross peaks had opposite signs compared with the other carbons in the long chain that each connect to two other aliphatic carbons. Finally, the HMQC-TOCSY spectrum, which showed the connections of the adjacent protons, was combined with the C13-HSQC spectrum to complete the assignments of the oleate (**Fig. 4.7**). The oleate assignments, especially those of α-CH_2 and ω-CH_3, directly guide the protein-ligand titration study.

4.4.3.2 Stoichiometry of oleate binding to LFABP The fatty acid environments in 1:2 and 1:0.5 complexes of ^{15}N-LFABP with [U-^{13}C]-oleate are shown in **Fig. 4.8**. Two distinct sets of α-CH_2 and ω-CH_3 resonances are observed in both C13-HSQC and HCCH-COSY spectra, and two slightly different carboxyl environments separated by 0.2 ppm are shown in the HA-CO correlation plot of the HCACO spectrum. The results

again demonstrate the specific binding of at least two fatty acid molecules per LFABP. As deduced from X-ray crystallography[25], these NMR data also support preferential occupancy of the primary (internal) binding site.

4.4.3.3 Chemical shift analysis on ligand The stepwise binding of fatty acid was monitored through the behavior of α-CH_2 and ω-CH_3 groups observed in ^{1}H-^{13}C correlation plots, using the complexes of ^{15}N-LFABP with [U-^{13}C]-oleate in ratios of 1:0.5, 1:1, 1:1.5, 1:2, 1:3, and 1:4 (**Fig. 4.9**). With addition of the first 0.5 equivalent of [U-^{13}C]-oleate, it was possible to populate one of this protein's binding sites preferentially, as indicated by the different peak intensities of the two sets of crosspeaks. That is, the first binding site of the oleate corresponds to peak #1 (40.6 ppm, 1.86 ppm) for the α-CH_2 group and peak #4 (16.5 ppm, 0.64 ppm) for the ω-CH_3 group. For the 1 oleate:holo-protein, a distinctive set of oleate resonances is observed, with similar chemical shifts to the set of α-CH_2 and ω-CH_3 resonances observed in 2 oleate:holo-LFABP. Two interpretations are possible for this latter phenomenon: (1) the first oleate occupies a site that is different from the final binding site and a rearrangement occurs upon the entrance of the second oleate to yield the final conformation; (2) the first oleate occupies the internal binding site and has its α-CH_2 rendered more sterically defined upon addition of the second oleate. After a third and then a fourth equivalent of oleate were added to the protein, the resonance positions of α-CH_2 and ω-CH_3 remained the same as in the 2 oleate:holo-protein, consistent with the protein chemical shift trends observed for the complexes of ^{15}N-LFABP with unlabeled oleate (Section 4.2). Thus, by viewing the ligand we can confirm the conclusion that LFABP binds at least two molecules of oleate.

4.4.3.4 Intensity analysis on ligand Since the α-CH_2 and ω-CH_3 resonances of [U-^{13}C]-oleate alone at (38.0 ppm, 2.18 ppm) and (16.5 ppm, 0.84 ppm) had proton chemical shifts close to those of the second binding site at (40.8 ppm, 2.20 ppm) and (17.1 ppm, 0.83 ppm), it should be asked whether the second oleate observed during titration is actually a free molecule. To address this question, intensity measurements were made for peaks #1 to #6 (see **Fig. 4.9**) in complexes of ^{15}N-LFABP with [U-^{13}C]-oleate at ratios of 1:0.5, 1:1, 1:1.5, 1:2, 1:3, and 1:4 at 10 °C and pH 7.0. A plot of intensity versus equivalents of oleate is shown in **Fig. 4.10**. The singly occupied oleate (peaks #1 and #4) decreases its intensity with increasing equivalents of oleate and disappears after adding a second oleate. The doubly occupied oleate (peaks #2, #3, #5, and #6) grows in intensity upon the addition of oleate and is unchanged between 1:3 and 1:4. These results suggest that entrance of the second oleate makes the first-bound oleate rearrange and that no free oleate exists until the addition of a third or maybe a fourth oleate. The intensity analysis of the ligand resonances again demonstrates the likelihood that a third oleate binds to the protein, which is consistent with the NMR results obtained by viewing the protein and the reported X-ray data[25].

4.5 Discussion

4.5.1 Comparison of holo-protein with palmitate and oleate ligands

Fig. 4.11 shows superimposed ^{1}H-^{15}N HSQC spectra for 1:2 complexes of ^{15}N-LFABP with [U-^{13}C]-palmitate and with [U-^{13}C]-oleate. The similar backbone amide peak positions suggest that the two long-chain FA-bound-proteins have similar

conformations. This result is reasonable in light of their similar structures and binding affinities.

4.5.2 Stoichiometry of fatty acid (FA) binding to LFABP

Both the cessation of changes in protein conformation after additon of two FA and the observation of two sets of α-CH_2 and ω-CH_3 in the spectra of bound ligands suggest that LFABP binds at least two FA. One α-CH_2 group has distinguishable prochiral protons; the ^{13}CO resonances are magnetically equivalent in palmitate-bound-protein but nearly equivalent in oleate-bound-protein at 10 °C. The further narrowing of ^{1}H-^{15}N HSQC peaks of LFABP indicates that LFABP could also bind a third FA.

But what accounts for LFABP's ability to solubilize up to six molecules of oleate? The explanation could be that exchange exists not only between the two bound oleates but also between bound-oleate and excess free oleate. The excess or partially bound-oleate may attach to the periphery of the protein as suggested by a 4-carbon fragment in the X-ray structure. Independent evidence for such exchange phenomena comes from the fact that the ^{13}C resonances of the two distinguishable methyl groups coalesced in the ^{1}H-^{13}C HSQC spectrum as the temperature was raised from 10 °C to 30 °C (data not shown).

4.5.3 Impact of ligand binding on the structure of LFABP

The spectral trends involving backbone amide chemical shifts, linewidths, peak doubling in the HN dimension (**Fig. 4.12**), additional observable backbone amide protons, and slower H/D exchange rates (see Chapter 3) all support the conclusion that

FA locks the LFABP into a well-defined, less flexible structure. **Fig. 4.12** shows the backbone amide assignments for a 1:2 complex of $^{13}C/^{15}N$-LFABP with unlabeled oleate at 30 °C and pH 7.0. The HSQC spectrum of apo-LFABP is shown as background for comparison. The assignments were completed based on a set of multi-dimensional NMR experiments (see Chapter 5).

In order to determine the protein sites that experience the greatest structural perturbations, the chemical shift difference in Hz was calculated for the combination of HN proton and ^{15}N resonances between apo- and holo-LFABP, i.e.,

$$\Delta\delta = \text{sqrt}((\Delta HN)^2 + (\Delta N)^2).$$

The quantity $\Delta\delta$ for oleate binding is plotted along the protein sequence in **Fig. 4.13**. Using the X-ray structure (oleate-bound holo-protein)[25] depicted with the SYBYL program (**Fig. 4.14**), residues with $\Delta\delta > 100$ Hz are labeled as "1" (they are: F3, Q8, V9, F18, I29, Q30, G32, D34, G37, T51, G55, K57, N61, E72, T75, G76, V101, T112, M113, K125, and R126). Residues with $\Delta\delta < 10$ Hz are labeled as "2" (they are: Q10, V42, H43, G45, K47, V48, L65, M85, G87, D88, F104, D107, D117, and I118). Those residues with missing backbone amide assignments in the apo form (but not in holo form) are labeled as "3" (they are: V38, S39, I52, T53,Y54, H60, T73, M74, V92, G106, I109, T110, R122, and V123). It is clear that residues in red and in green are located near the two ligands, and those residues in blue are located in general further away from the ligands. These trends indicate that addition of ligand significantly perturbs the residues near the portal (αII-βB turn, βC-βD turn, and βE-βF turn as shown in **Fig. 4.13**) and those inside the binding cavity (as shown in **Fig. 4.14**). A similar set of conclusions

could be drawn from the NMR structure for holo-LFABP in solution, which was determined subsequently to this analysis (see Chapter 5).

X-ray results suggest that the two bound oleate molecules take advantage of nearly all of the cavity space formed by the β-barrel, possibly exchanging with each other and interacting physically in a highly hydrophobic environment. The X-ray structure suggests that the primary bound-oleate has an internalized carboxylate, which is thought to form an ion pair with the guanidine group of Arg^{122}, and a U-shaped hydrocarbon chain. As the first oleate molecule binds to the protein, a larger cavity and more hydrophobic environment may be created to allow the second oleate molecule to physically squeeze into the protein and also induce some rearrangement of the first bound oleate. The secondary bound-oleate has the carboxylate near the surface with the hydrocarbon tail inserted toward the center of the protein and the primary bound oleate. The orientation of the two oleates bound to LFABP is pictured in **Fig. 4.5**.

The LFABP-fatty acid titration study was presented at both the 39th Experimental Nuclear Magnetic Resonance Conference (ENC) in California in 1998 and the 28th Keystone Symposium on Molecular and Cellular Biology in Colorado in 1999.

Figure 4.1 Appearance comparison among samples of 0.50 mM oleate in pH 7.0 phosphate buffer (left NMR tube), complex of 0.26 mM LFABP with 0.50 mM oleate (ratio 1:2) in pH 7.0 phosphate buffer (middle NMR tube), and complex of 0.17 mM LFABP with 1.20 mM oleate (ratio 1:8) in pH 7.0 phosphate buffer (right NMR tube).

Figure 4.2 Selected regions of one-dimensional proton spectra for the apo form of ^{15}N-labeled LFABP and its complexes with unlabeled oleate in ratios of 1:1, 1:2, 1:3, 1:4, 1:6, and 1:8, respectively. All data sets were acquired on 0.2 mM samples at 30 °C and pH 7.0 with presaturation of the water resonance.

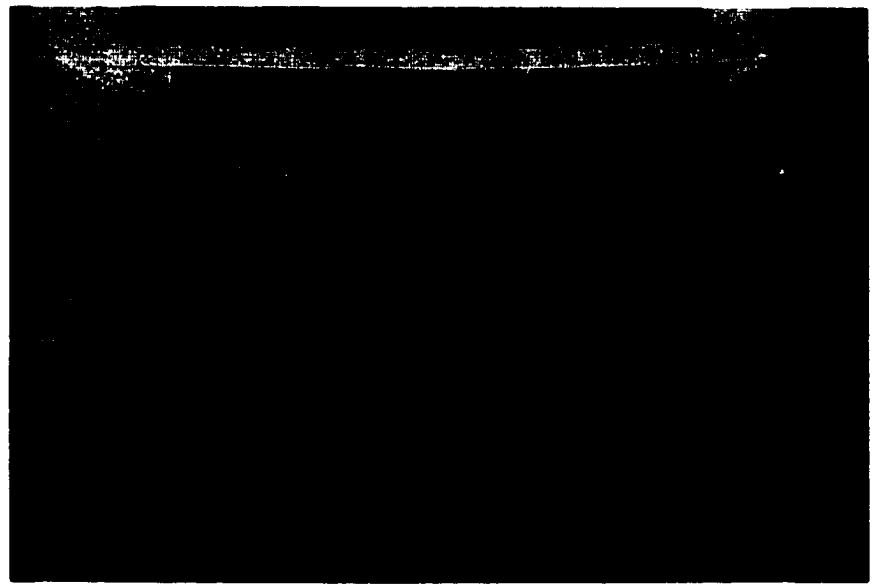

Figure 4.1

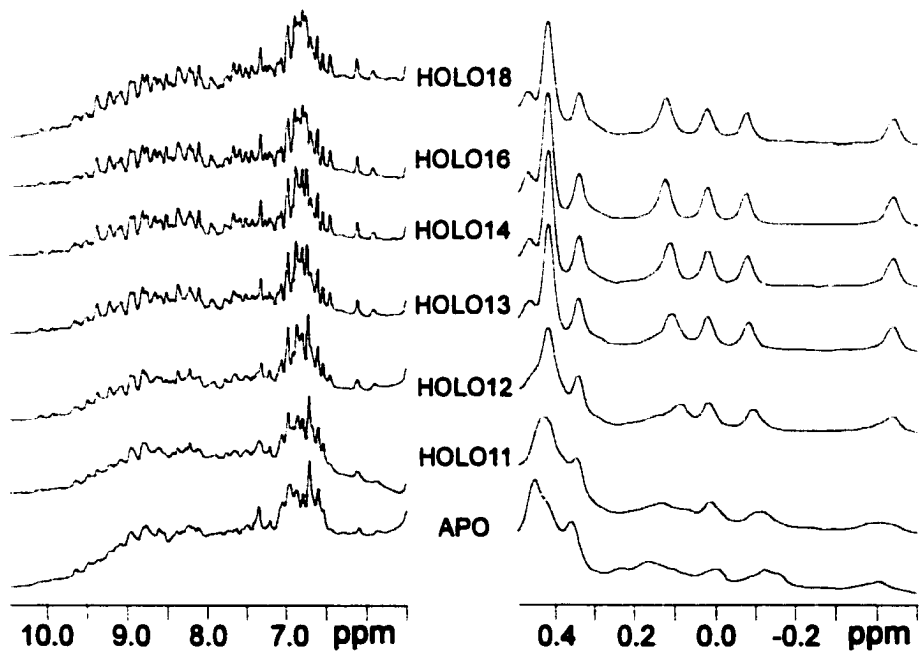

Figure 4.2

Figure 4.3 Comparison of ^{1}H-^{15}N HSQC spectra for the apo form of ^{15}N-LFABP and its complexes with unlabeled oleate in ratios of 1:1, 1:2, 1:3, 1:4, and 1:8, respectively. All data sets were acquired on 0.2 mM samples at 30 ∘C and pH 7.0 with a sensitivity-enhanced PFG-HSQC sequence[34]. As the protein-to-ligand ratio was varied from 1:0 (apo) to 1:6 (plot not shown), the average linewidths at half-height for 41 well-resolved signals ranged from 34.6 to 17.4 Hz (HN) and from 18.7 to 7.8 Hz (^{15}N). Doubled peaks (33 in apo form) are highlighted by arrows.

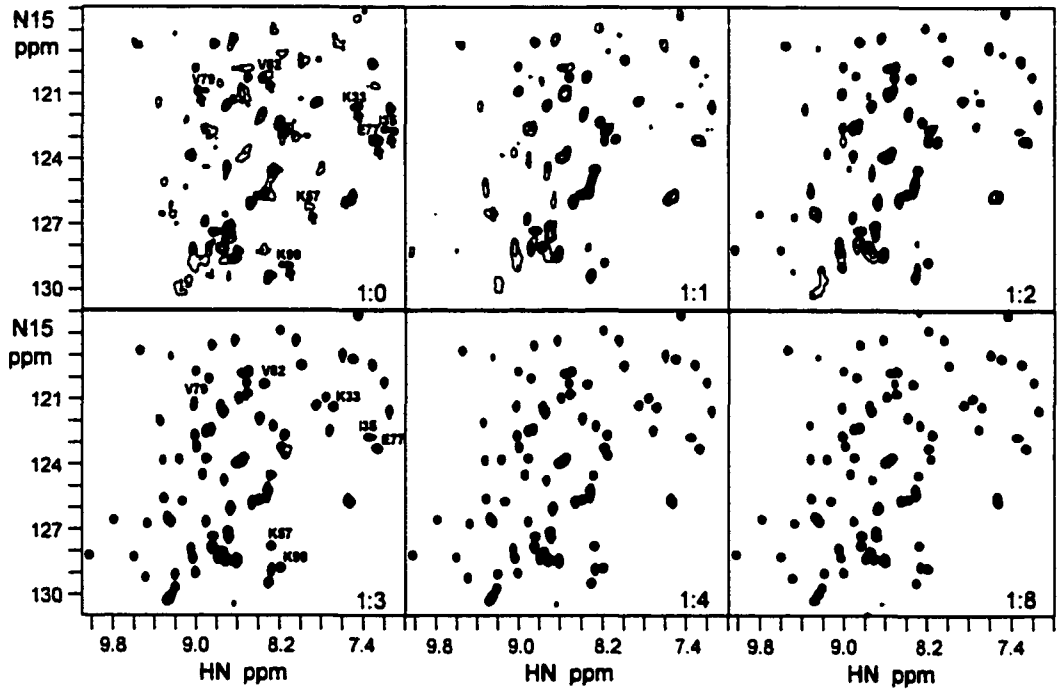

Figure 4.3

Figure 4.4 Bar plot of HN linewidth versus protein sequence for complexes of ^{15}N-LFABP with unlabeled oleate in ratios of 1:2 to 1:8. All bars show changes in linewidth upon addition of successive equivalents of FA. Secondary structural elements shown on the plot are based on X-ray results for 2 oleate-bound holo-LFABP[25].

Figure 4.5 Site-specific effects of ligand binding on rat liver FABP, as determined from ^{1}H-^{15}N HSQC NMR spectra. The X-ray structure of 2 oleate-bound holo-LFABP[25] is used here as a model. Residues with HN chemical-shift difference exceeding 10 Hz between 1:2 and 1:3 ratios of holo-protein are shown in black.

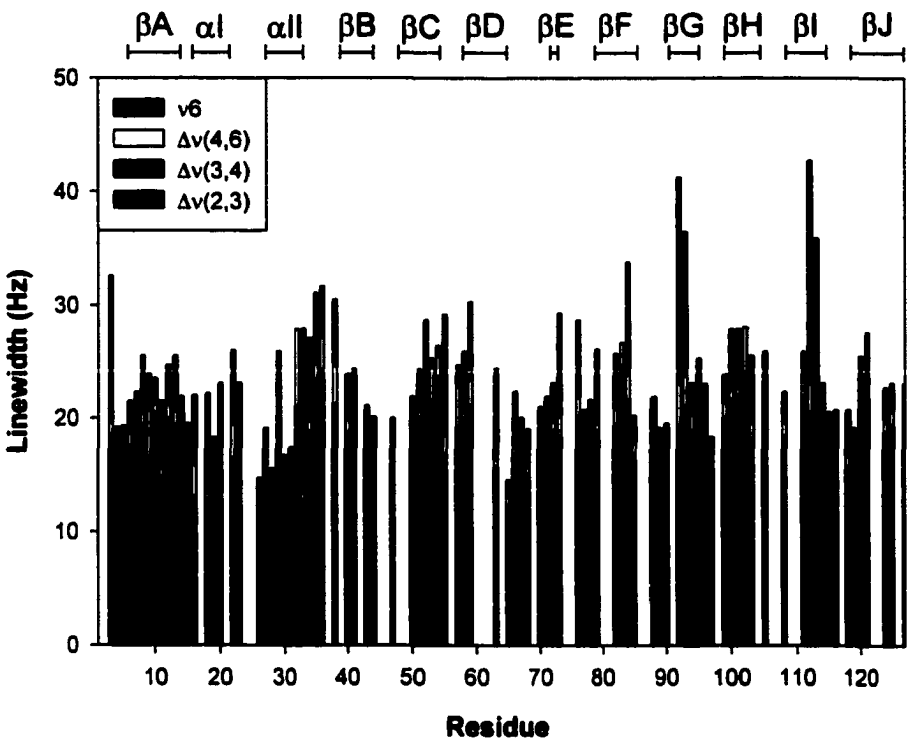

Figure 4.4

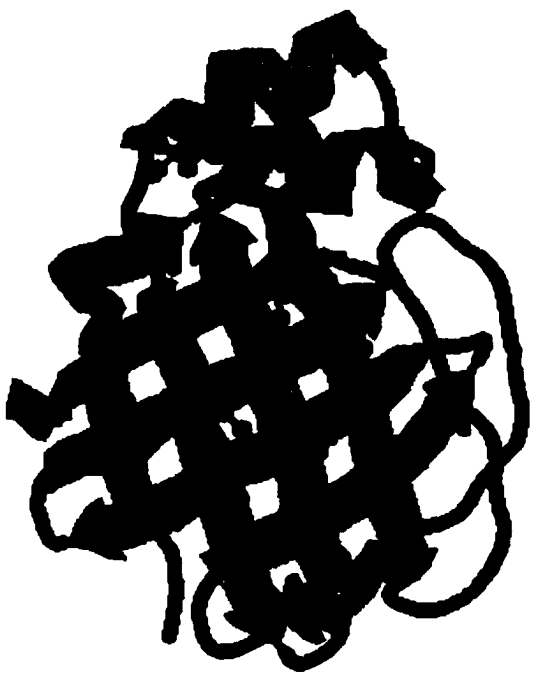

Figure 4.5

Figure 4.6 An NMR view of fatty-acid environments on a complex of recombinant [^{15}N]-LFABP with [U-^{13}C]-palmitate (ratio 1:2) examined at 10 °C and pH 7.0. Left: $^{1}H_{\alpha}$-^{13}CO correlation plot from a 2D HCACO experiment, showing a single carbonyl shift corresponding to the two distinct pairs of α-protons. Right: 2D ^{1}H-^{13}C HSQC results, illustrating chemically shifted resonances for methyl (ω_1, ω_2) and carboxymethylene (α_1, α_2) ends of the fatty-acid molecules. Portions of the corresponding ^{1}H-decoupled ^{13}C spectrum are shown above the contour plots.

Figure 4.7 ^{1}H and ^{13}C assignments for 2 mM [U-^{13}C]-oleate in pH 7.0 phosphate buffer obtained from 2D ^{1}H-^{13}C HSQC (black) and HMQC-TOCSY (cyan) experiments. α/β connectivities are shown at lower contours. m and n represent 12-15 and 4-7 CH_2 groups, respectively.

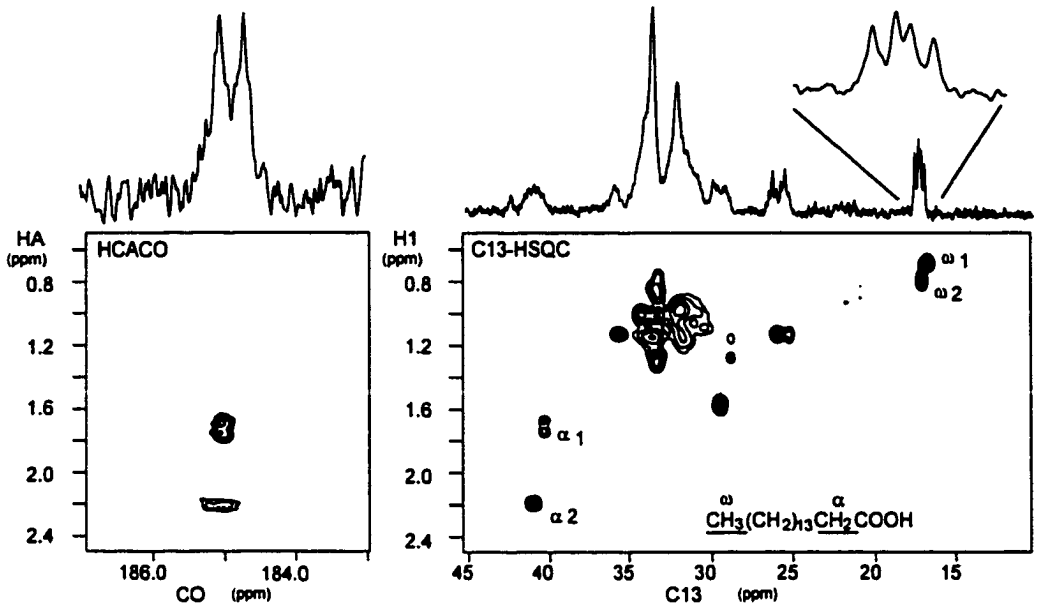

Figure 4.6

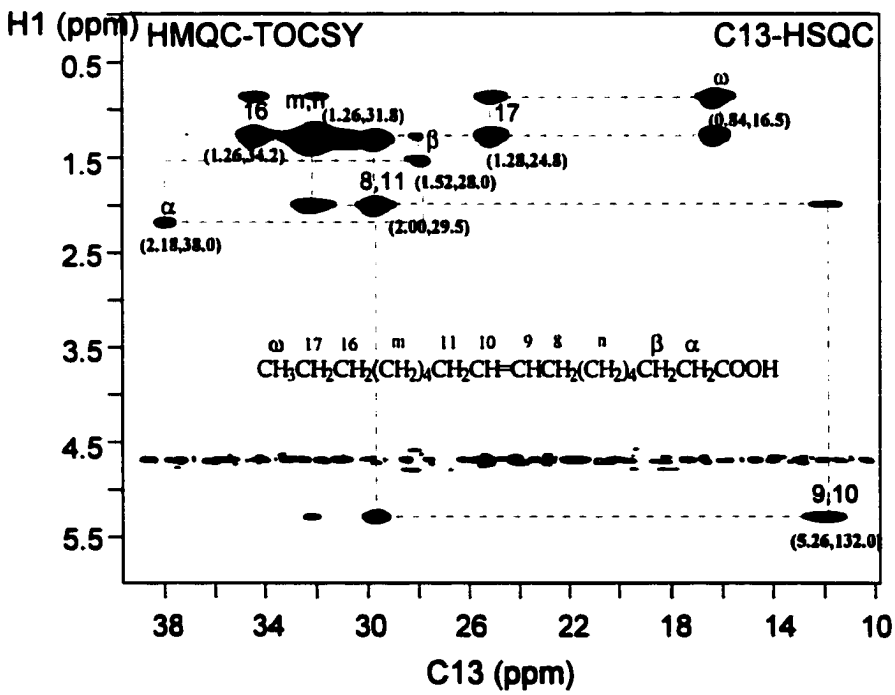

Figure 4.7

Figure 4.8 FA environments in complexes of [U-^{15}N]-LFABP with [U-^{13}C]-oleate at 10 °C and pH 7.0. Left and Center: a 1:2 complex. Left: $^{1}H_{\alpha}$-^{13}CO correlation plot from a 2D HCACO experiment[83], showing two similar carbonyl shifts corresponding to the two distinct pairs of α-protons. Center: contour plot of 2D ^{1}H-^{13}C HSQC and HCCH-COSY, showing two sets of α-CH_2 and ω-CH_3 resonances. Right: 2D ^{1}H-^{13}C HSQC results for a 1:0.5 complex, showing preferential occupancy of the primary binding site.

Figure 4.9 FA environments in complexes of [U-^{15}N]-LFABP with [U-^{13}C]-oleate in ratios of 1:0.5, 1:1, 1:1.5, 1:2, 1:3, and 1:4, viewed by ^{1}H-^{13}C HSQC correlation at 10 °C and pH 7.0. Changes in chemical shift for the two sets of α-CH_2 and ω-CH_3 upon adding the ligand to the protein are described in the text.

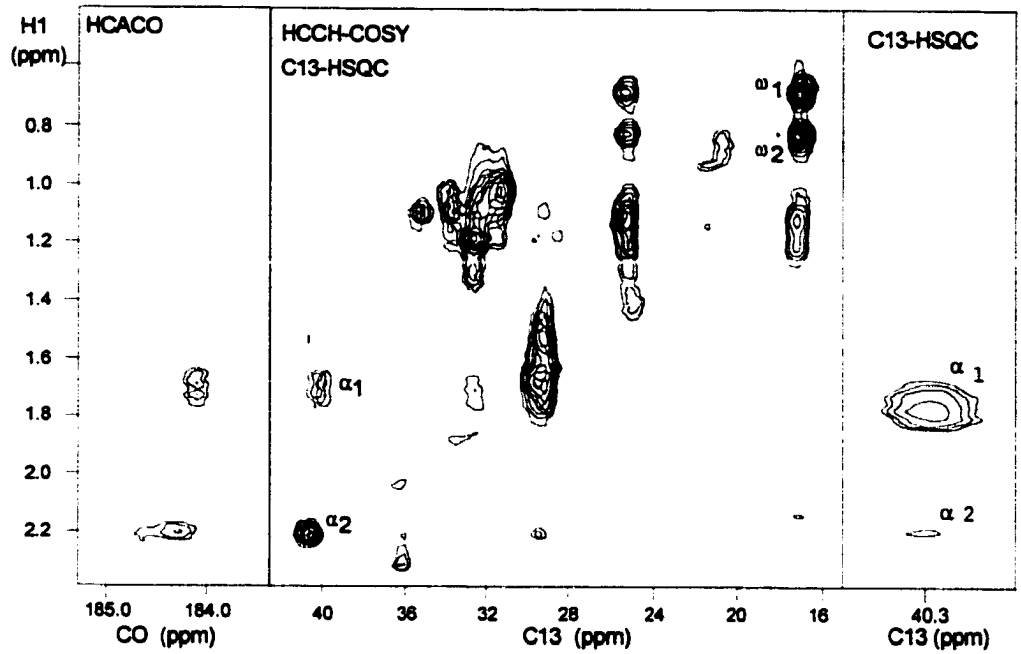

Figure 4.8

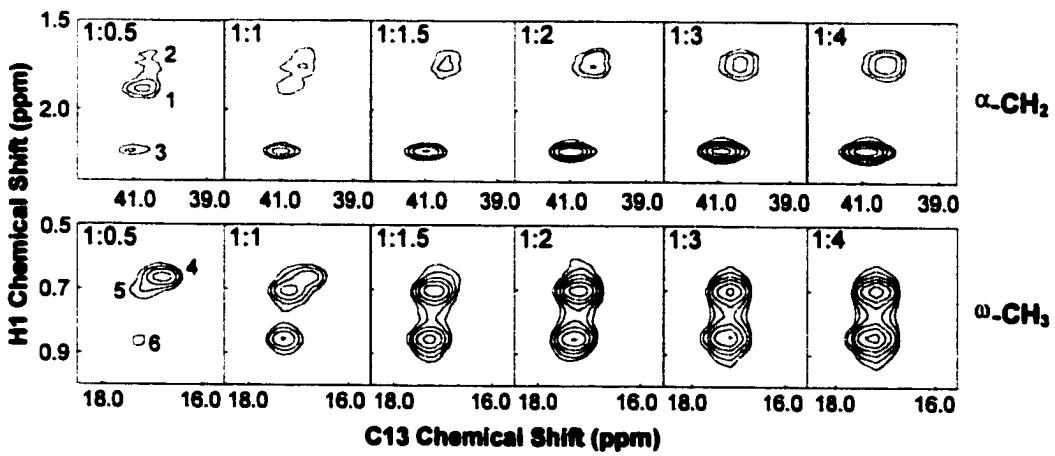

Figure 4.9

Figure 4.10 Intensity analysis of α-CH_2 and ω-CH_3 groups in ^{1}H-^{13}C HSQC spectra (peak numbers are defined in **Fig. 4.9**) for complexes of [U-^{15}N]-LFABP with [U-^{13}C]-oleate in ratios of 1:0.5, 1:1, 1:1.5, 1:2, 1:3, and 1:4 at 10 °C and pH 7.0. The plot of peak intensity versus equivalents of oleate shows that intensity grows from a ratio 1:0.5 to 1:3 and is unchanged between 1:3 and 1:4.

Figure 4.11 Superimposed ^{1}H-^{15}N HSQC spectra for a 1:2 complex of [U-^{15}N]-LFABP with [U-^{13}C]-palmitate and a complex of [U-^{15}N]-LFABP with [U-^{13}C]-oleate, showing the similar binding characteristics of the two ligands to the protein.

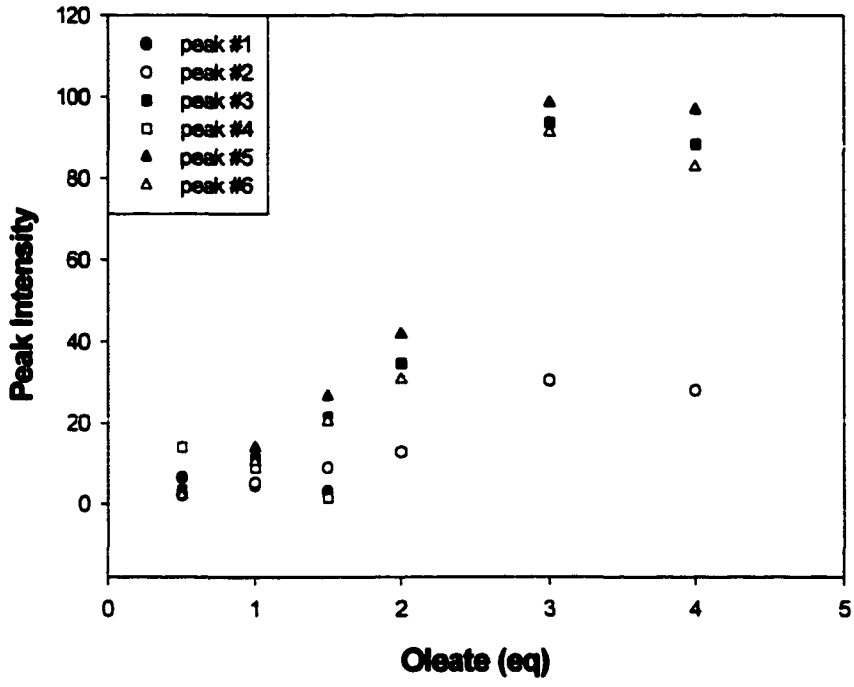

Figure 4.10

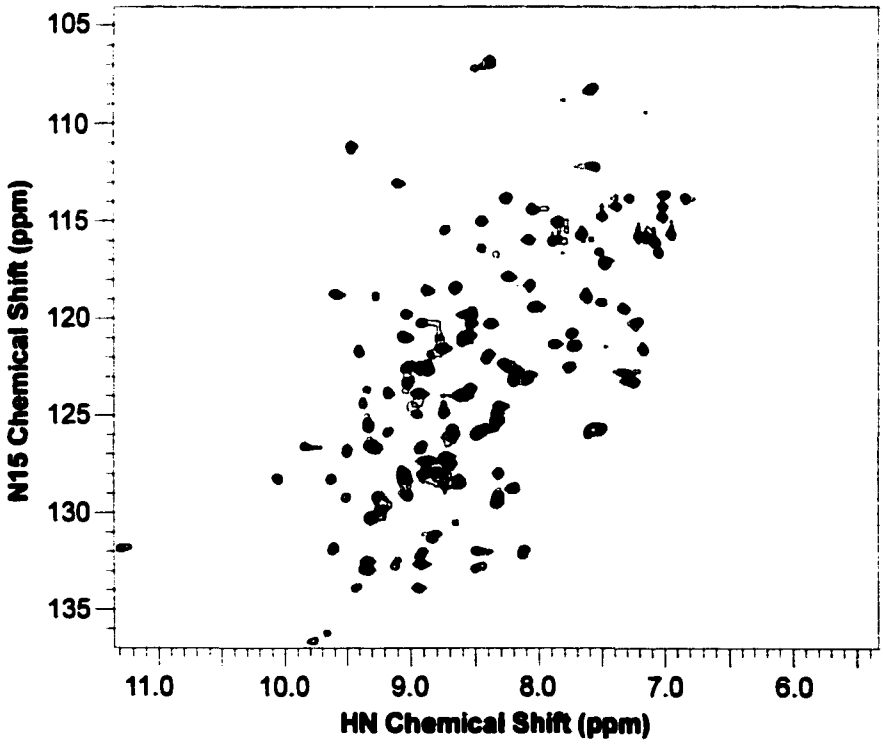

Figure 4.11

Figure 4.12 HN and ^{15}N assignments for a 1:2 complex of $^{13}C/^{15}N$ dual-labeled rat LFABP with unlabeled oleate at 30 °C and pH 7.0. The HSQC spectrum of the apo-LFABP is shown as background for comparison.

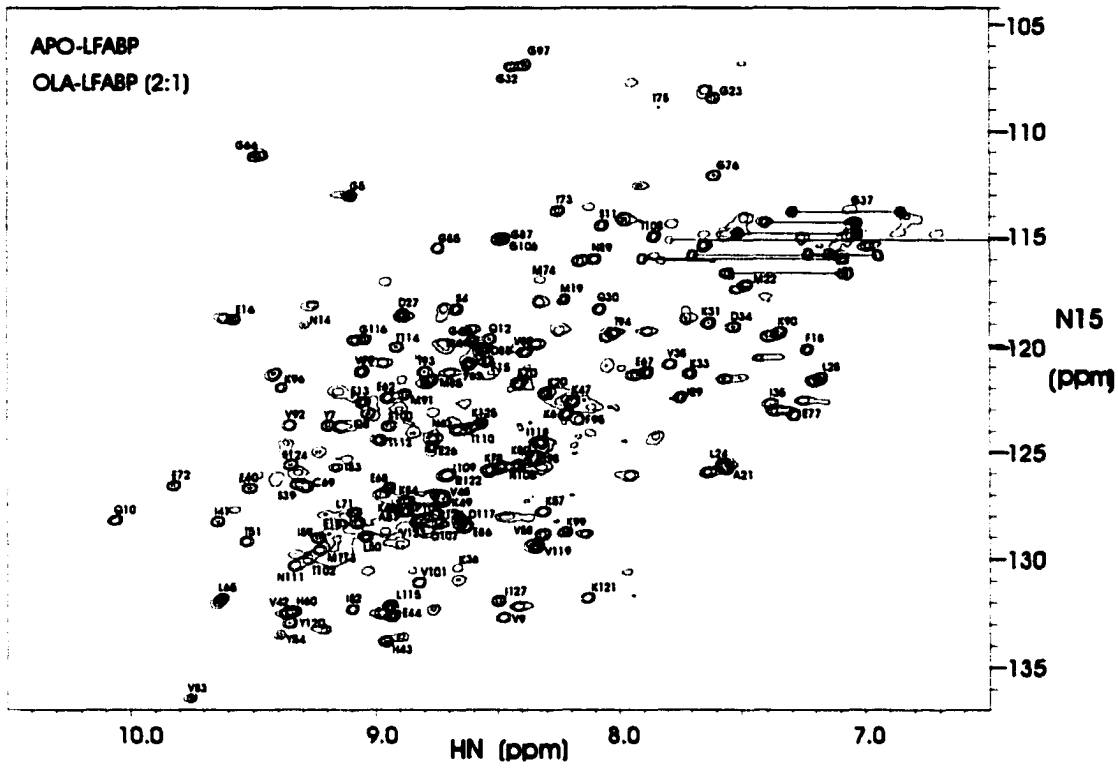

Figure 4.12

Figure 4.13 Chemical-shift differences ($\Delta\delta$) for the combination of HN and ^{15}N resonances (see text) between apo- and 2 oleate-bound holo-LFABP as a function of protein sequence. Stars indicate unavailable assignments due to missing HN peaks for the apo-protein. Residues 17 and 25 are prolines. The first Met residue and Asn^2 are not assigned in either apo- or holo- proteins. The secondary structural elements shown above the plot are taken from the X-ray structure for 2 oleate-bound holo-LFABP[25].

Figure 4.14 Chemical shift difference between apo- and 2 oleate-bound holo-LFABP, shown on the X-ray structure[25] of 2 oleate-bound holo-LFABP. Residues with a chemical-shift difference larger than 100 Hz (see **Fig. 4.13**) are labeled as "1", and residues with a chemical-shift difference less than 10 Hz are labeled as "2". Residues with missing assignments in the apo form are labeled as "3".

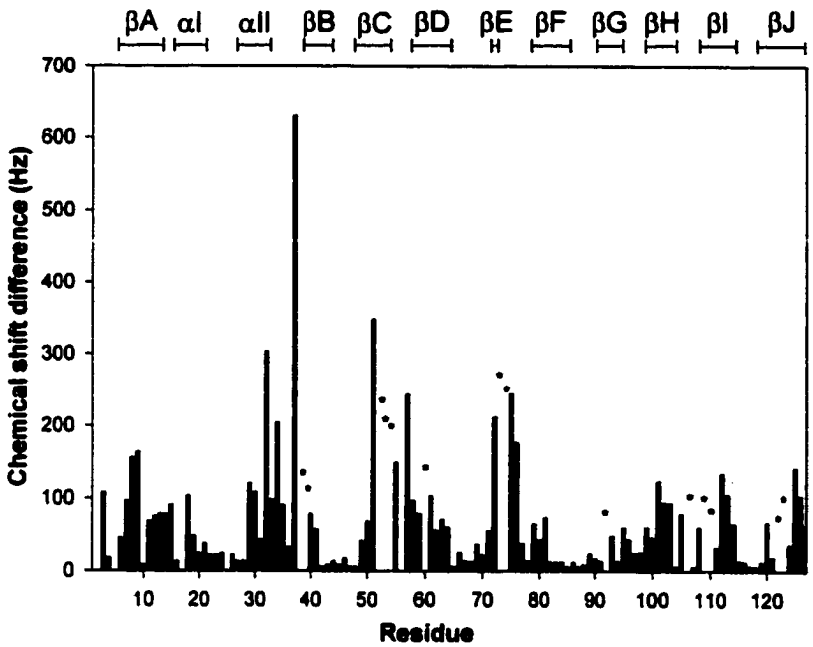

Figure 4.13

Figure 4.14

CHAPTER 5

TERTIARY STRUCTURE OF HOLO-OLEATE-LFABP

5.1 Introduction

The NMR method for protein structure determination in aqueous solution relies on a dense network of distance restraints and dihedral angle restraints[7]. The distance restraints are derived from nuclear Overhauser effects (NOEs) between pairs of nearby hydrogen atoms in the protein. NOEs are the essential NMR data to define the secondary and tertiary structure of a protein because they connect hydrogen atoms separated by less than about 5 Å from amino acid residues that may be far away along the protein sequence but close together in space (**Fig. 5.1**). The NOE reflects the transfer of magnetization between spins coupled by the dipole-dipole interaction in a molecule that undergoes Brownian motion in a liquid[85]. The dipolar cross-relaxation rate constant is proportional to the inverse sixth power of the distance between the two interacting protons. In the initial rate approximation, NOE cross-peak intensities (or volumes) are proportional to the cross-relaxation rate constants. Dihedral angle constraints are directly related to vicinal scalar coupling constants between atoms separated by three covalent bonds from each other, ^3J[86]. All possible backbone conformations are obtained by variation of the torsion angles ϕ_i and ψ_i (**Fig. 5.2**). The side chain conformations are characterized by the torsion angles χ_i^1, χ_i^2, ...

The secondary structure (α-helix or β-sheet) of a protein is reflected in the relative intensities of NOEs as well as the magnitudes of the torsion angles[5]. For example, the observation of intense d_{NN} NOEs and small ϕ and ψ values ($\phi \sim -57°$, $\psi \sim$ -

47° for a right-handed α-helix) is indicative of a helical polypeptide; an observation of intense $d_{\alpha N}$, weak d_{NN} and $d_{\beta N}$ NOEs and large ϕ and ψ values ($\phi \sim -139°$, $\psi \sim +135°$ for antiparallel β-sheet) is indicative of extended β-strands of polypeptide.

Based on the results of LFABP-FA titration studies presented in Chapter 4, two equivalents of FA constituted a binding ratio for which no further changes in NMR chemical shifts were observed, and which approached the approximately two equivalents of bound oleate observed by X-ray crystallography[25]. This chapter will present the three-dimensional solution structure of rat LFABP complexed with two oleate molecules determined using multidimensional triple-resonance NMR methods. Oleate was chosen as the bound ligand for structural studies of holo-LFABP because of its physiologic abundance in liver[87] and its high affinity for LFABP[88]. For the dissociation of oleate from rat and bovine LFABP, fluorescence methods have yielded K_d's ranging from 0.009 to 0.2 μM for one site (tight-binding)[88], and the titration calorimetry method gave K_d's of 0.06-4.0 μM for the other site (moderate-binding)[89,90]. Thus, oleate has suitable binding affinity to the protein for NMR determination of its solution-state structure. Moreover, oleate is more soluble than palmitate in aqueous solution and thus easier to work with.

The NMR structure of apo-LFABP is more challenging to solve for the following reasons: (1) 15 of 124 backbone amide ^{1}H and ^{15}N were not assigned, possibly because of incompletely defined secondary structures in the protein; (2) 33 doubled cross-peaks were observed in the 2D ^{1}H-^{15}N HSQC spectrum, attributed to multiple conformations of the protein; (3) nearly 80 % of the backbone amide protons were exchanged with D_2O within a 47-minute timeframe, suggesting high solvent accessibility of the protein; and (4) a significant number of broad and overlapped peaks were found in all NMR

experiments. For these reasons, holo-LFABP was chosen as the first candidate for NMR structural determination. Accompanying ^{15}N-relaxation studies will be presented in Chapter 6 for both apo- and holo-LFABP. After we understand in detail NMR structure of holo-protein and the dynamics of the apo-protein, approaches may be designed for solving the NMR structure of the apo-protein (not included in the thesis).

5.2 NMR Assignments of oleate-bound holo-LFABP

5.2.1 Sample preparation

5.2.1.1 H_2O Sample The procedure for preparing a complex of $^{13}C/^{15}N$-LFABP with unlabeled oleate was as follows: (1) a 2.66-ml sample of 0.24 mM $^{13}C/^{15}N$-LFABP in pH 6.0 phosphate buffer containing 10^{-4} % aproprotenin protease inhibitor was treated using a PD-10 gel filtration column with 100 mM $(NH_4)_2CO_3$ to raise the sample pH to 8.9; (2) the sample was mixed with 400 µl of 5 mM unlabeled sodium oleate at pH 9.6 to achieve a protein-to-oleate ratio of 1:3; (3) the mixture was stirred overnight at 4 °C and subjected to Centricon-10 ultrafiltration with a pH 7.0 phosphate buffer in order to reduce the volume to 560 µl and remove the unbound or weakly bound oleate, assuming that a sample of holo-LFABP with two bound oleates (from results in Chapter 4) was produced; and (4) after addition of 5 % D_2O by volume, 300 µl of the solution was transferred to a 5-mm Shigemi NMR tube and stored at 4 °C.

Fig. 5.3 shows a 1D proton spectrum of a 5 mM unlabeled oleate salt in H_2O at pH 9.0. The clear double bond (CH=CH) resonance at 5.32 ppm indicates that the oleate is not oxidized and is suitable for use.

The concentrations of both apo- and holo-proteins were assayed at 0.24 and 0.67 mM by the Lowry method [30]. **Fig. 5.4** gives the results of the concentration measurements for the proteins based on Beer's Law under the following conditions: (1) the protein standard is 100 mg/ml bovine albumin in 0.85 % NaCl solution containing 0.05 % NaN_3 (for preservative); (2) the absorption wavelength is set at 600 nm; (3) protein samples were diluted 10 times for apo and 20 times for holo forms, respectively; (4) a correction factor of 0.6 was used for LFABP (since Lowry method overestimates the protein concentration of purified LFABP) [91]; and (5) the absorbance readings for the diluted samples of apo and holo were 0.5977 and 0.9808, respectively. Thus, the concentration of the protein can be calculated by

(absorbance / slope) * (dilution factor) * 0.6

in units of mg/ml. To convert the protein concentration from mg/ml to mM, the molecular weight of LFABP (14 kDa) should be used. For example, for apo-LFABP (slope = 1.05 in **Fig. 5.4**),

conc. (mM) = (0.5977 / 1.05) * 10 * 0.6 /14000 * 10^3 = 0.24.

5.2.1.2 D_2O Sample After the above holo-protein sample in H_2O was used for completing ^1H, ^{13}C, and ^{15}N sequential assignments and running 3D/4D ^{15}N-edited NOESY experiments, lyophilization techniques (Section 3.2) were used to exchange the H_2O sample with D_2O for the purposes of studying H/D exchange and running 3D/4D ^{13}C-edited NOESY experiments.

5.2.2 NMR experiments

Similar to procedures described for apo-LFABP, one 2D ^{1}H-^{15}N **HSQC** (Section 2.3.3.2) and seven 3D NMR experiments (Section 2.3.4) were carried out to obtain the sequential resonance assignments for oleate-bound holo-LFABP at pH 7.0 and 30 °C. **CBCA(CO)NH** and **HNCACB** spectra were used to make the backbone sequential assignments of H^{N}, ^{15}N, C^{α}, and C^{β}. Backbone ^{13}CO and H^{α} assignments were achieved (except for Gly) by **HNCO** and **CBCACOHA** experiments, respectively. Side-chain aliphatic ^{13}C assignments were obtained by **C(CO)NH-TOCSY** and completed by **HCCH-TOCSY** experiments. An **H(CCO)NH-TOCSY** spectrum was used for backbone and side-chain aliphatic ^{1}H assignments, but unambiguous differentiation of certain protons (such as: H^{β} and H^{γ} of Gln, Glu, Met, Ile, Arg, Lys, and Pro; and H^{γ} and H^{δ} of Lys) required data from the HCCH-TOCSY experiment. The acquisition parameters for those 2D/3D NMR experiments on holo-LFABP are listed in **Table 5.1**.

Table 5.1 Acquisition parameters for NMR experiments on a oleate-bound holo-LFABP

Experiment	Nucleus F1/F2/F3	Complex data points F1/F2/F3	Spectral width, kHz F1/F2/F3	Scans	Exp. time, h
HSQC	$^{15}N/^{1}HN$	256/1024	2.0/8.0	32	5.5
CBCA(CO)NH	$^{13}C^{\alpha\beta}/^{15}N/^{1}HN$	58/40/512	9.2/2.0/8.0	16	48.5
HNCACB	$^{13}C^{\alpha\beta}/^{15}N/^{1}HN$	50/40/512	9.2/2.0/8.0	32	82.5
HNCO	$^{13}CO/^{15}N/^{1}HN$	52/40/512	1.8/2.0/8.0	16	43.5
CBCACOHA	$^{13}C^{\alpha\beta}/^{13}CO/^{1}HN$	58/60/512	9.2/2.0/8.0	16	70.5
C(CO)NH-TOCSY	$^{13}C/^{15}N/^{1}HN$	52/40/512	9.2/2.0/8.0	32	87.5
H(CCO)NH-TOCSY	$^{1}H/^{15}N/^{1}HN$	72/38/512	4.0/2.0/8.0	32	114.0
HCCH-TOCSY	$^{1}H/^{13}C/^{1}H$	128/32/512	4.2/3.6/8.0	16	68.5

5.2.3 NMR assignments

All NMR data were processed with NMRPipe and converted to NMRView (Section 2.4). The processing parameters for 2D/3D data were similar to those shown in **Table 2.2**. As described in Chapter 4, titration of LFABP with oleate or palmitate locked the protein into a well-defined conformation and resulted in very well resolved and sharp

spectral features (**Fig. 4.12**). In the ^{1}H-^{15}N HSQC spectrum, all of the 124 expected backbone amide resonances were observed and assigned, with the single exception of Asn^{2}; all 10 pairs of side-chain NH_2's of Asn and Gln were observed and assigned by acquiring CBCA(CO)NH data with a delay time of $1/4J_{NH}$ instead of $1/2J_{NH}$; and 2 side-chain NH's of Arg were also observed and assigned. 2D HBCBCGCDHD and HBCBCGCDCEHE experiments (Section 2.3.5) were used to make the assignments for aromatic proton H^{δ} and H^{ε} resonances from Phe, His, and Tyr (there is no Trp in LFABP) residues. 30 of 46 aromatic protons were assigned. A total of 28 side-chain ^{13}CO resonances were assigned by acquiring CBCACOHA and HNCO data with a delay time of $1/4J_{XH}$ instead of $1/2J_{XH}$. (X = ^{13}C for CBCACOHA and X = ^{15}N for HNCO. For side-chain ^{13}CO groups, there are two protons attached to either side-chain ^{13}C or side-chain ^{15}N.) The complete ^{1}H, ^{13}C, and ^{15}N assignments are listed in **Table 5.2**; the percentage of completed assignments are compared with those from apo-LFABP and summarized in **Table 5.3**.

Table 5.3 Completeness of resonance assignments for apo- and holo-LFABP.

	APO-LFABP						**HOLO-LFABP**					
Backbone	HN	N	C^{α}	C^{β}	H^{α}	CO	HN	N	C^{α}	C^{β}	H^{α}	CO
# Expected	124	124	127	115	139	127	124	124	127	115	139	127
# Assigned	109	109	120	108	130	118	123	123	127	115	139	127
% Completion	87.9	87.9	94.5	93.9	93.5	92.9	99.2	99.2	100	100	100	100
Side-chain	^{13}C	^{1}H	NH_2/NH		Aromatic	CO	^{13}C	^{1}H	NH_2/NH		Aromatic	CO
			N	H	^{1}H				N	H	^{1}H	
# Expected	164	451	14	24	46	28	164	451	14	24	46	28
# Assigned	139	405	0	0	0	0	163	441	12	22	30	28
% Completion	84.8	89.8	0	0	0	0	99.4	97.8	86	92	65.2	100

5.3 Secondary Structure Determination

The complete secondary structure of oleate-bound holo-LFABP was derived from sequential assignments of $^{1}H^{\alpha}$, $^{13}C^{\alpha}$, $^{13}C^{\beta}$, and ^{13}CO resonances with the CSI program

(Section 2.6.2) as shown in **Fig. 5.5** (bottom panel), which reveals two 2 α-helices inserted between the first two β-strands of the 10 strand β-sheet, similar to the results found for apo-LFABP (Section 2.6.2). This is supported by the plot of NOE connectivies (HN(i)-HN(j)) derived from a 3D ^{15}N-edited NOESY-HSQC experiment (Section 5.4.1.2) along the LFABP sequence (**Fig. 5.5**, top panel), that is, two α-helical structural elements were again indicated by connectivity patterns parallel and adjacent to the diagonal [92], and 10 anti-parallel β-strands structures are confirmed by 9 connectivity patterns orthogonal to the diagonal. The distribution of backbone amide proton NOEs among the 9 connectivity patterns indicates that there is a 'gap' between β-strands D and E.

5.4 Tertiary Structure Determination

5.4.1 nD (n = 2, 3, and 4) NOESY experiments

Nuclear Overhauser enhancements (NOEs) provide information on ^{1}H-^{1}H inter-nuclear distances that may be used directly for NMR structure calculations on the protein. Different types of NOESY experiments are designed for obtaining ^{1}H-^{1}H NOEs. In principle, the number of ^{1}H-^{1}H NOE cross-peaks observable in 3D and 4D heteronuclear-edited NOESY spectra are the same as those present in the 2D homonuclear NOESY spectra. However, the resolution of 3D/4D spectra is substantially improved due to the fact that each NOE cross-peak is separated into a third or fourth dimension by the chemical shift of the heteronucleus attached to the proton. Moreover, the sensitivity of the 3D and 4D NOESY experiments is relatively good because the through-bond coherence transfer steps are highly efficient.

Several multidimensional NOESY experiments (2D, 3D, and 4D) were carried out for protein structure determination. A mixing time of 100 ms was used for all NOESY experiments.

5.4.1.1 2D NOESY experiment The two-dimensional NOESY experiment has the following pulse sequence: $\pi/2$ - t_1 - $\pi/2$ - τ_m - $\pi/2$ - Acquire (t_2) [93]. The spectrum acquired for holo-LFABP is shown in **Fig. 5.6**. It is obvious that 3D and/or 4D NOESY experiments are needed to make unambiguous NOE assignments for the protein. Nevertheless, 2D NOESY is typically useful for the NOEs assignments involving aromatic protons because the aromatic carbons have not been assigned and this region has relatively little peak overlap.

5.4.1.2 ^{15}N-edited NOESY experiments 3D ^{15}N-edited NOESY-HSQC[93] (**noesy3Dn**) and 4D ^{13}C/^{15}N-edited HMQC-NOESY-HMQC[94,95] (**cn4Dnoesy**) experiments were conducted on oleate-bound holo-LFABP dissolved in H_2O. Their complete magnetization transfer pathways are as follows:

noesy3Dn $\quad {}^1H_i\,(t_1) \xrightarrow{NOE} {}^1H_j^N \xrightarrow{{}^1J_{NH}} {}^{15}N_j\,(t_2) \xrightarrow{{}^1J_{NH}} {}^1H_j^N\,(t_3, \text{acquire})$

cn4Dnoesy $\quad {}^1H_i \xrightarrow{{}^1J_{CH}} {}^{13}C_i\,(t_1) \xrightarrow{{}^1J_{CH}} {}^1H_i\,(t_2) \xrightarrow{NOE} {}^1H_j^N \xrightarrow{{}^1J_{NH}} {}^{15}N_j\,(t_3) \xrightarrow{{}^1J_{NH}} {}^1H_j^N\,(t_4, \text{acquire}).$

The NOE connectivities between amide protons and all other kinds of protons can be measured from these two NOESY experiments.

5.4.1.3 ^{13}C-edited NOESY experiments For oleate-bound holo-LFABP dissolved in D_2O phosphate buffer, 4D ^{13}C/^{13}C-separated HMQC-NOESY-HMQC[96] (**c4Dnoesy**) and 3D ^{13}C-edited NOESY (**noesy3Dc**) experiments were carried out to obtain through-space information between carbon-attached protons and carbon-attached protons (4D),

and NOEs information between carbon-attached protons and all others (3D). The paths of magnetization transfer are described as follows:

c4Dnoesy $^{1}H_i \xrightarrow{^{1}J_{CH}} {}^{13}C_i\,(t_2) \xrightarrow{^{1}J_{CH}} {}^{1}H_i\,(t_1) \xrightarrow{NOE} {}^{1}H_j \xrightarrow{^{1}J_{CH}} {}^{13}C_j\,(t_3) \xrightarrow{^{1}J_{CH}} {}^{1}H_j\,(t_4, \text{acquire})$

noesy3Dc $^{1}H_i\,(t_1) \xrightarrow{NOE} {}^{1}H_j \xrightarrow{^{1}J_{CH}} {}^{13}C_j\,(t_2) \xrightarrow{^{1}J_{CH}} {}^{1}H_j\,(t_3, \text{acquire}).$

The pulse sequence for noesy3Dc was altered from the software package of Lewis Kay's (University of Toronto, Canada) (**Fig. 5.7**).

NMR acquisition parameters for all the nD (n = 2, 3, and 4) NOESY experiments are listed in **Table 5.4**. The NMR data sets were processed with NMRPipe and converted to NMRView. The intensity of every picked NOE cross-peak was obtained by NMRView to generate an input file for structure calculation with DYANA program.

Table 5.4 Acquisition parameters for nD NOESY experiments on oleate-bound holo-LFABP

Experiment	Nucleus F1/F2/F3/F4	Complex data points F1/F2/F3/F4	Spectral width, kHz F1/F2/F3/F4	Scans	Exp. time, h
2D NOESY	$^{1}H/^{1}H$	512/1024	9.0/9.0	96	61.5
noesy3Dn	$^{1}H/^{15}N/^{1}HN$	128/40/512	8.0/2.0/8.0	16	110.5
cn4Dnoesy	$^{1}H/^{13}C/^{15}N/^{1}HN$	64/16/16/256	8.0/3.6/2.0/5.0	2	91.0
c4Dnoesy	$^{1}H/^{13}C/^{13}C/^{1}H$	64/16/16/256	5.3/3.6/3.6/5.3	2	79.5
noesy3Dc	$^{1}H/^{13}C/^{1}H$	128/32/512	8.0/3.3/8.0	16	89.0

5.4.2 Assignments of NOE constraints between ^{1}H (i) and ^{1}H (j)

All the NOE constraints from different NOESY experiments were derived from the sequential ^{1}H chemical shift assignments on holo-LFABP. The published X-ray structure[25] was loaded in NMRView as a PDB (protein data bank entry 1lfo) file for cross-check purposes when there was more than one possible NOE assignment by NMR. For example, in the noesy3Dc data set, the NMR-based NOE assignments could be ambiguous due to the degeneracy of ^{13}C chemical shifts. For $^{1}HN(i)$-$^{1}H(j)$ NOEs, the cn4Dnoesy spectrum gave unambiguous assignments because of the ^{13}C and ^{15}N

chemical shift dispersion in both the third and fourth dimensions (**Fig. 5.8**). The β-sheet network derived from backbone NOEs is illustrated in **Fig. 5.9**. The hydrogen bonds in the β-barrel formed by backbone amide protons and oxygen that are supported by NOE assignments are summarized in **Fig. 5.10**. **Fig. 5.11** illustrates the sequential and medium-range interproton distances derived from the NOESY data sets and confirms the elements of regular secondary structure in the holo-LFABP. The proton-deuterium exchange information (Section 3.4) is also shown in **Fig. 5.11**.

5.4.3 DYANA protocol for structure determination

For oleate-bound holo-LFABP, the program DYANA (DYnamics Algorithm for Nmr Applications)[97,98], a successor of the program DIANA (DIstance geometry Algorithm for Nmr Applications),[99] was used to calculate its NMR tertiary structure in solution and display it with the MOLMOL program[100]. Two separate supporting programs of DYANA, CALIBA and HABAS, were also used in structure calculation. The flowchart of calculation procedures is shown in **Fig. 5.12**.

The program CALIBA derives upper-limit distance constraints from all assigned NOE peaks and adds them to the list of current distance constraints. The NOE peaks are classified into three calibration classes:

(1) backbone: all HN/H^{α}--HN/H^{α}, and HN/H^{α}--H^{β} with $|i-j|<5$ function: $V = A/d^6$

(2) sidechain: not "backbone" and not "methyl" function: $V = B/d^4$

(3) methyl: all involving methyl groups function: $V = C/d^4$

where V is volume or intensity of the peak and d is distance. The constant A is calculated automatically by default CALIBA program according to the NOE peak input

file; the constants B and C are set to $B = A/d_{min}^2$ and $C = B/3$, where d_{min} is set to 2.4 Å as a default value. After running CALIBA, an upper-limit distance constraints file is generated in which only unique distance constraints are included.

The lower-limit distance constraints file is generated based on hydrogen bonds derived from NOE assignments (see **Fig. 3.6**). The distance between the amide proton and oxygen is set to 1.8 Å, and the distance between the amide nitrogen and oxygen is set to 2.7 Å.

The program HABAS performs grid searches for all amino acid residues including the dihedral angles ϕ, ψ, χ^1, and χ^2. After running HABAS, an angle constraints file is generated and the upper-limit distance constraints are modified to remove irrelevant constraints (constraints that involve fixed distances and constraints that cannot be violated).

With the input files of upper-limit distance constraints, lower-limit distance constraints, and dihedral angle constraints, DYANA performs a 3D structure calculation using the standard simulated annealing protocol[97] with a random generator seed number. The results include an overview, dihedral angles, and Cartesian co-ordinate files. Based on the judgment of RMSD values and percentage of residual constraint violations listed in the overview output file, adjustment of the distance constraints and cross-checks of the NOE assignments may be needed for re-calculation of the structure. The final acceptable dihedral angles and Cartesian co-ordinates files can be loaded into the MOLMOL program to display the three-dimensional structure.

5.4.4 NMR structure calculation

Three of five NOESY experimental datasets (**Table 5.4**), were used for the 3D structure calculation on oleate-bound holo-LFABP: 2D NOESY, cn4Dnoesy, and noesy3Dc. The noesy3Dn dataset was not used for the following reasons: (1) all HN(i)-^{1}H(j) NOE connectivities could be obtained from the cn4Dnoesy dataset except those NOEs of amide protons to protons with no attached carbons (e.g. backbone amide protons and side-chain NH_2 protons) or aromatic protons (since aromatic carbons were not assigned); (2) the exception from (1) was compensated by the 2D NOESY dataset; (3) the baselines of the noesy3Dn spectrum were not flat enough to ensure the accuracy of the experimental NOE intensities. Another dataset, c4Dnoesy, was not used because of its low signal-to-noise ratio (only 2 scans were used), poor spectral resolution, and small number of signals compared to the noesy3Dc dataset. Furthermore, all expected ^{1}H(i)-^{1}H(j) NOEs in c4Dnoesy could be obtained from the noesy3Dc dataset.

A combined total of 3177 NOE cross-peaks obtained from the 2D NOESY dataset (82 assigned), cn4Dnoesy dataset (955 assigned), and noesy3Dc dataset (2140 assigned) were used as input files to the distance calibration. 2421 unique upper-limit distance constraints were used for the HABAS grid search, and 464 dihedral angle constraints were generated. Of the 2421 upper-distance limits, 534 were found to be irrelevant, i.e. they are either independent of the conformation, or there exists no conformation that would violate the constraint. The remaining 1887 modified upper-distance limits, together with 68 lower-distance limits derived from H-bonds and 464 dihedral angle constraints, were processed with DYANA to obtain a total of 20 structures with a backbone RMSD value of 1.05 ± 0.20 Å and 4% distance violations. The processing parameters and results are summarized below:

NMR Dataset	Assigned NOEs	Unique Constraints	2421	Computational Results	
2D NOESY	82	Intra-residue	1060	# of structures	19 of 20
cn4Dnoesy	955	Sequential	474	Distance violations	83 (4%)
noesy3Dc	2140	Medium-range, |i-j|<5	222	Angle violations	2 (0.4%)
All datasets	3177	Long-range, |i-j|≥5	665	Backbone RMSD	1.05 Å
(25 per residue)		Dihedral angles	464	Heavy atom RMSD	1.74 Å
		Hydrogen bonds	68		

The number of distance restraints are shown as a function of protein sequence in **Fig. 5.13** (top panel). The RMS deviation of the 15 best NMR structures from the mean, at each residue, is also shown in **Fig. 5.13** (middle panel), with the secondary structure as a reference (bottom panel). The superimposed backbone structures of the 15 best conformations calculated with the DYANA program are shown in **Fig. 5.14**. As expected, the C- and N- terminal regions and the turns that connect the β-strands (typically at C-D turn, E-F turn, G-H turn, H-I turn, and I-J turn) are less well defined compared to the 10 β-strands. The NMR-derived structure, shown as a ribbon diagram in **Fig. 5.15**, exhibits a "β-barrel" shape, which is a common feature of the intracellular lipid-binding protein family[25]. Compared to the X-ray structure (**Fig. 5.15**), the NMR structure shows very similar secondary structural characteristics (described further in Chapter 7).

5.5 Discussion

5.5.1 Completeness of assignments for apo- and holo-LFABP

As expected, adding fatty acid locks the protein into a rigid conformation and makes the protein structure well defined. Because of the sharper linewidths and retrieval of missing peaks, a significantly higher percentage of resonance assignments were made for holo-LFABP than apo-LFABP (**Table 5.3**).

5.5.2 Comparison between apo- and holo-LFABP secondary structures

As noted previously in Section 3.4, adding fatty acid enhances the definition of the protein secondary structure. Look at the β-sheet networks derived from ^{1}H-^{1}H NOEs (**Fig. 5.16**), it is clear that more NOEs are observed from holo-LFABP, indicating more hydrogen-bond connections and thus less protein flexibility. **Table 5.5** shows the secondary structural elements for apo- and holo-LFABP derived by the CSI method and the X-ray results from oleate-bound holo-LFABP for comparison. The X-ray results indicate an additional loop inserted in the βF strand, i.e. βF' involves residues 78-79 while βF'' comprises residues 84-86. In the table, we use 78...86 to denote the βF strand.

Table 5.5 Secondary structural elements for apo- and holo-LFABP obtained from NMR and X-ray results

Residues	APO (CSI)	HOLO (CSI)	HOLO (X-ray)
βA	6-13	5-13	5-13
αI	14-22	14-23	15-21
αII	26-32	25-34	26-32
βB	38-44	38-43	38-44
βC	46-51	46-53	47-54
βD	57-64	57-64	57-64
βE	67-72	69-73	71-72
βF	76-86	78-85	78...86
βG	89-95	89-95	90-95
βH	98-105	98-103	98-105
βI	109-115	108-115	108-115
βJ	118-125	118-125	118-127

5.5.3 Intermolecular interaction between LFABP and oleate

(Dr. Xiaomin Yang, a research associate in our group, analyzed the intermolecular NOE data, some of which was obtained by Mr. Christopher Kroenke of Columbia University).

The published X-ray structure[25] of oleate-bound holo-LFABP showed two ligands in the binding cavity, which is consistent with our NMR results that two equivalents of oleate are required to lock the protein into the holo conformation (Chapter 4). One oleate molecule (OLA129), presumed to be the first bound ligand, is bound in a U-shaped conformation (**Fig. 4.5**). It occupies an internal site different from other FABP's and has a carboxyl group that interacts with Arg^{122} and is partially exposed to structural water within the binding cavity. By contrast, the second oleate molecule (OLA128) occupies a hydrophobic site that may be partially created by OLA129, and its carboxyl group is situated close to the protein surface. The two bound oleate molecules are in proximity to each other physically. The possibility of a third bound oleate was suggested by additional unresolved electron density, which is again consistent with our NMR titration results showing the ability of LFABP to solubilize additional fatty acid molecules.

Our NMR analysis of intermolecular NOEs between LFABP and oleate (**Table 5.6**) revealed that 7 residues (L24, L28, I29, G32, I35, Y54, and I59) had intermolecular NOEs with OLA128 and 15 residues (I41, V48, L50, F63, L71, T73, V83, T93, F95, I98, T102, I109, M113, Y120, and S124) had intermolecular NOEs with OLA129. Two data sets were used for intermolecular NOE assignments. One measured NOEs between aliphatic carbon-attached protons in the protein and all protons in oleate, using a sample of $^{13}C/^{15}N$-labeled LFABP complexed with unlabeled oleate. The other measured NOEs between protons in the protein and carbon-attached protons in oleate, using a sample of ^{15}N-labeled LFABP complexed with [U-^{13}C]-oleate. The chemical shifts of oleates in the complexed form were based on the assignment of the free form (**Figure 4.7**), assuming no significant change between the free oleate and bound one, except alpha- and methyl-

protons which were obtained from titration results (**Figure 4.8**). There were 43 NOEs assigned in the first data set and 20 NOEs in the second data set. All those NOEs were assigned and confirmed with the X-ray structure[25] as a reference (< 5Å cutoff for the X-ray-derived proton-proton distance). The overall picture of LFABP-oleate interactions is shown in **Figure 5.17**.

Two kinds of important information could be extracted from our intermolecular NOE results: (1) What is the orientation of the oleate in the protein cavity? (2) What kind of interaction exists between protein and ligand and how does the oleate bind to LFABP?

Firstly, by looking through the details of the intermolecular NOE assignments and checking the oleate-bound holo-LFABP X-ray[25] structure, we can constrain the location of the oleate. For OLA128, NOEs between I35 HB, I35 HD11 and OLA128 H4 (see **Figure 4.7** for the oleate labeling) help to set the location of the OLA128 head group. NOEs between I59 HD11, I59 HG21 and the OLA128 methyl protons give information regarding the location of the OLA128 tail. Moreover, NOEs between Y54 HE and OLA128 H12-H15 confirm the position of OLA128 in the protein cavity. For OLA129, NOE data show that I98 and Y120 are close to its tail, I41, T102, and I109 are close to its head group, and V83 and M113 are close to its double bond. Thus, our NMR data basically support the X-ray results, which revealed that OLA129 is bound in a U-shape and OLA128 has its head group exposed to the aqueous interface.

By looking back at the chemical shift perturbation data between apo- and holo-LFABP (**Chapter 4**), it can be seen that some residues exhibit much larger proton chemical-shift changes between the apo and holo forms than the others. For example, the amide proton difference of G32 and side-chain proton difference of I35 are as high as 0.5

and 0.15 ppm, respectively, which means that adding ligand changes the protein conformation substantially and there is likely to be an interaction between the ligand and those protein residues. In fact, intermolecular NOE data did show that G32 HA1 interacts with OLA128 H7 and I35 HB, HD11 interact with OLA128 H4. Therefore, large chemical-shift changes in the protein can be used to deduce which short distances (< 5Å) in the X-ray structure correspond to sites of ligand binding and further are supportive of the intermolecular NOE data. Residue G32 is located at the end of the second α-helix and I35 is located at the turn between αII and βB regions that are considered part of the hypothetical "portal" region for ligand entry and exit. Thus, both our intermolecular NOE and titration data suggest that residues located in the "portal" region are responsible for the protein-ligand interaction. This conclusion is supported by other FABPs in the iLBP family, such as IFABP[3,21,22], CRBPII[23] and HFABP[24].

Using a cut-off of 0.15 ppm for the proton NMR chemical-shift difference and 5.0 Å for the X-ray-derived proton-proton distance, it may be deduced that residues L28, I29, and K33 (in region αII) interact with OLA128 (data not shown), and residues L71, E72 (the end of βE) and M74, T75 (βE-βF turn) interact with OLA129 (data not shown). Again, intermolecular NOE data confirm these protein-ligand interactions involving L28, I29, and L71 protein sites. The only exception to this correlation is K57, which exhibited large chemical shift perturbations but no intermolecular NOEs.

Secondly, most of the residues (18 out of 22) that showed proximal interactions with oleate are hydrophobic, with the exception of T73, T93, T102, and S124. Even for those four residues (Thr or Ser), only aliphatic protons are involved in the interactions of protein and ligand. In addition, our titration data (**Figure 4.8**, 2D ^{1}H-^{13}C HSQC

spectrum) showed preferential occupancy of the primary binding site for a 1:0.5 complex, assumed from X-ray[25] data to be OLA129. Thus our NMR results are consistent with the hypothesis that OLA129 binds to LFABP first by hydrophobic-hydrophobic interactions with the protein. Given the more hydrophobic environment created by OLA129, the second oleate (OLA128) then binds to LFABP via hydrophobic-hydrophobic interactions. Also, these interactions between OLA128 and OLA129 may serve to maintain the hydrophobic environment in the binding cavity.

Figure 5.1 Illustration of ^{1}H-^{1}H NOEs in a polypeptide chain. From reference 5.

Figure 5.2 Standard nomenclature for the atoms and the torsion angles along a polypeptide chain. From reference 5.

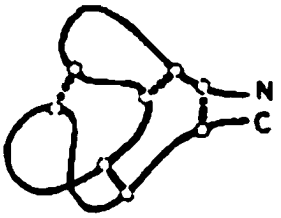

Figure 5.1

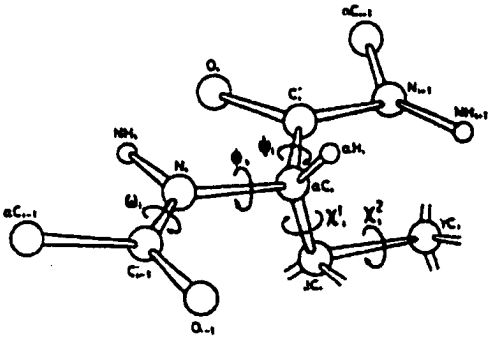

Figure 5.2

Figure 5.3 1D proton spectrum for a 5 mM oleate salt in H_2O solvent at pH 9.0.

Figure 5.4 Protein concentration measurements by Lowry method. The absorbencies were measured at 600 nm.

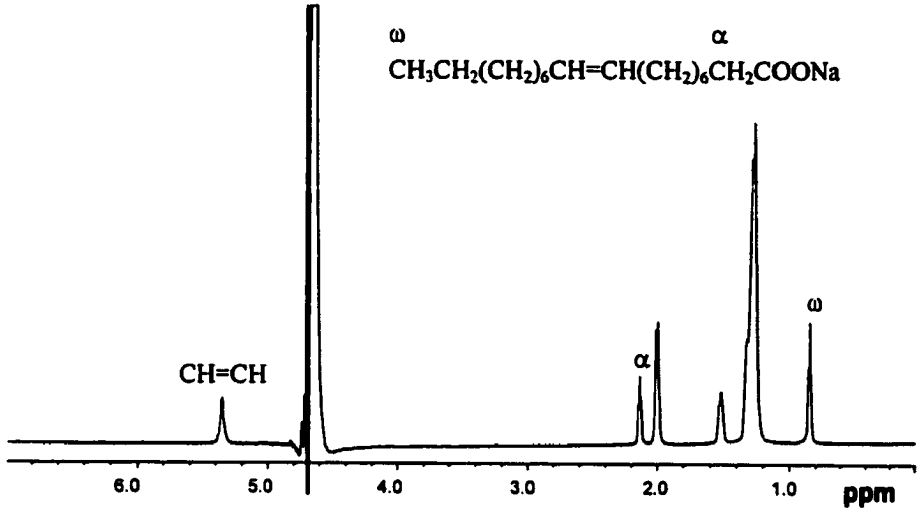

Figure 5.3

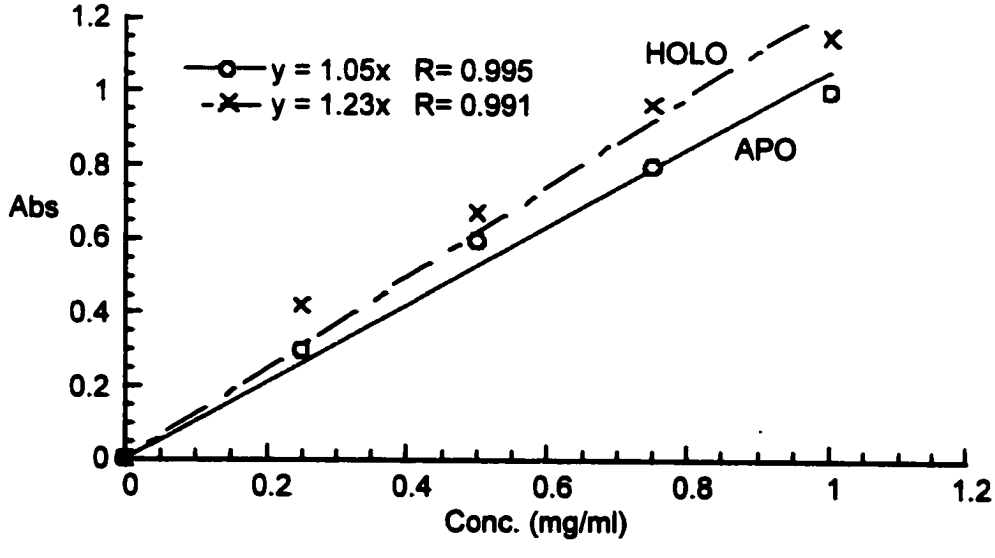

Figure 5.4

Figure 5.5 Illustration of the secondary structure on 2 oleate-bound holo-LFABP. Top panel: Diagonal plot presenting the backbone amide proton NOEs connectivities along the LFABP sequence[92]. Bottom panel: Representation of secondary structure elements derived from sequential assignments by CSI program[66].

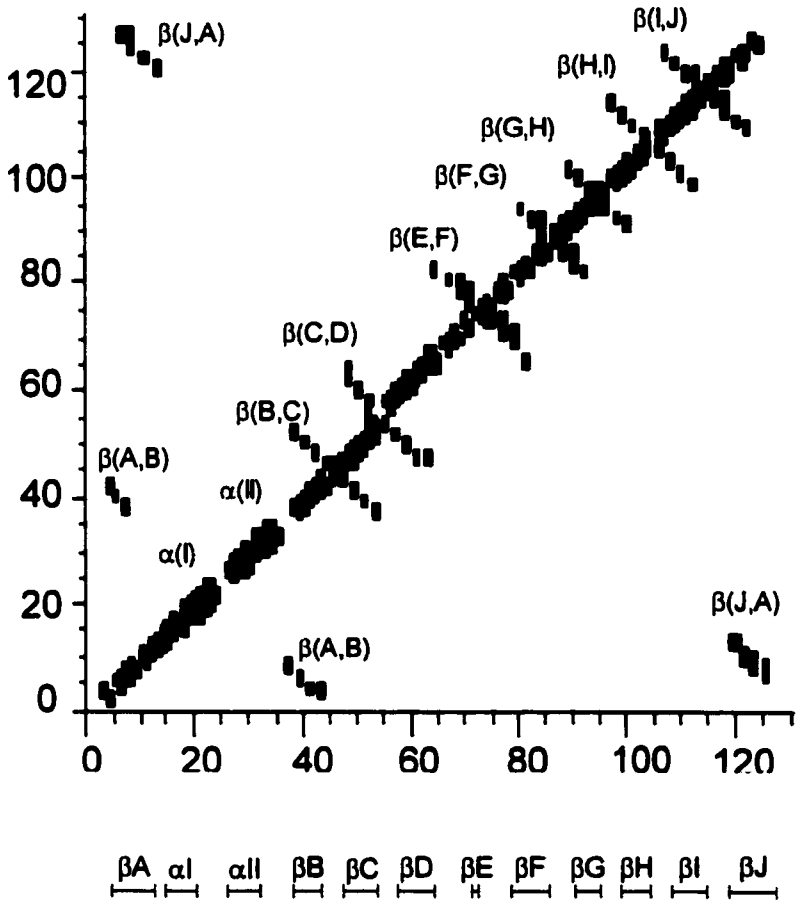

Figure 5.5

Figure 5.6 Contour plot of the entire ^{1}H-^{1}H 2D NOESY spectrum for 0.67 mM 2 oleate-bound holo-LFABP at pH 7.0 and 30 °C. Water suppression was achieved by 'wet' scheme[84].

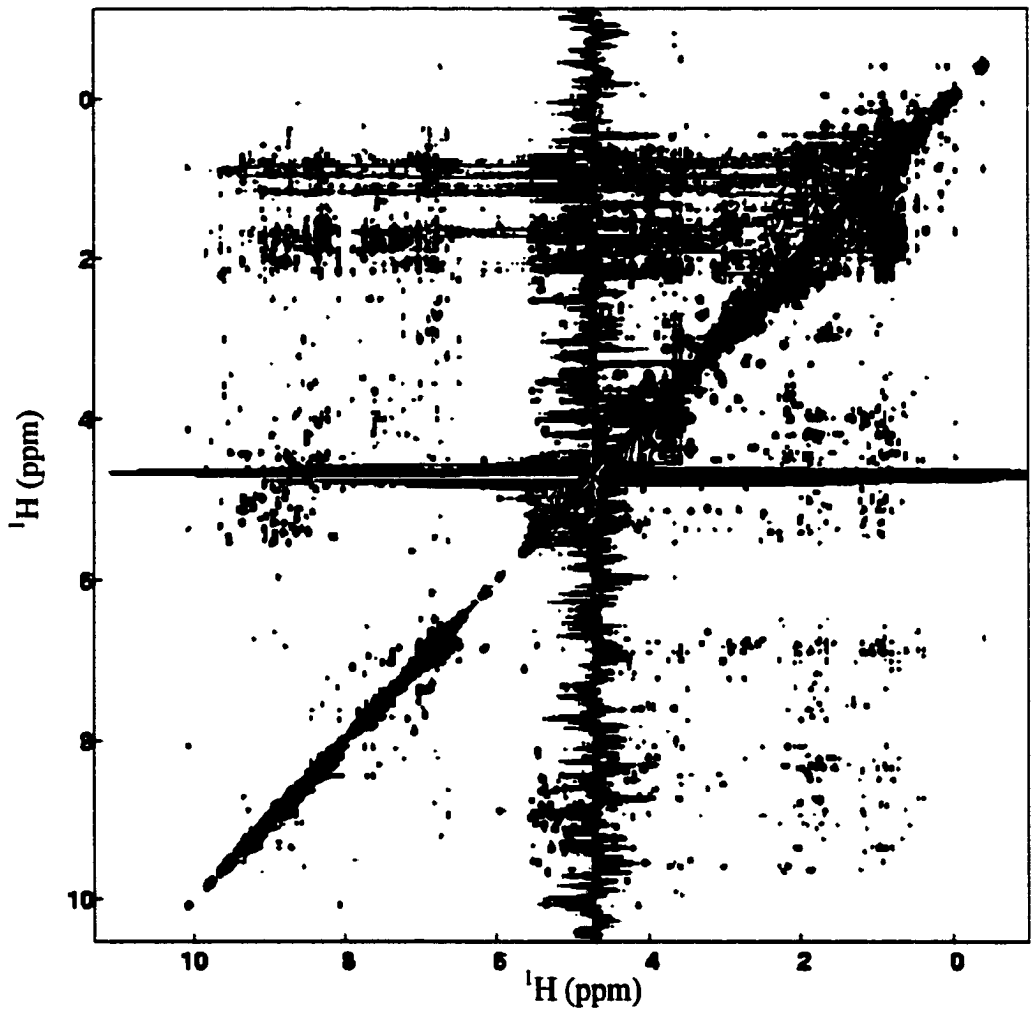

Figure 5.6

Figure 5.7 Pulse sequence for the gradient-enhanced 3D ^{13}C-edited NOESY experiment. The sequence was altered from Lewis Kay's package (University of Toronto, Canada). All narrow (wide) pulses have a flip angle of 90° (180°). The value of τ_a was set to 1.7 ms ($1/J_{CH}$). ^{13}CO was decoupled using the SEDUCE-1 decoupling sequence. ^{15}N decoupling before and during acquisition were achieved with GARP and WALTZ16 decoupling schemes, respectively. The phase cycle employed was: ϕ_1 = 4(x), 4(-x); ϕ_2 = 8(x), 8(-x); ϕ_3 = 4(x), 4(-x); ϕ_5 = x, y, -x, -y; and receiver = x, -y, -x, y, 2(-x, y, x, -y), x, -y, -x, y. Quadrature detection in t_1, t_2, and t_3 was implemented with the States-TPPI method[77].

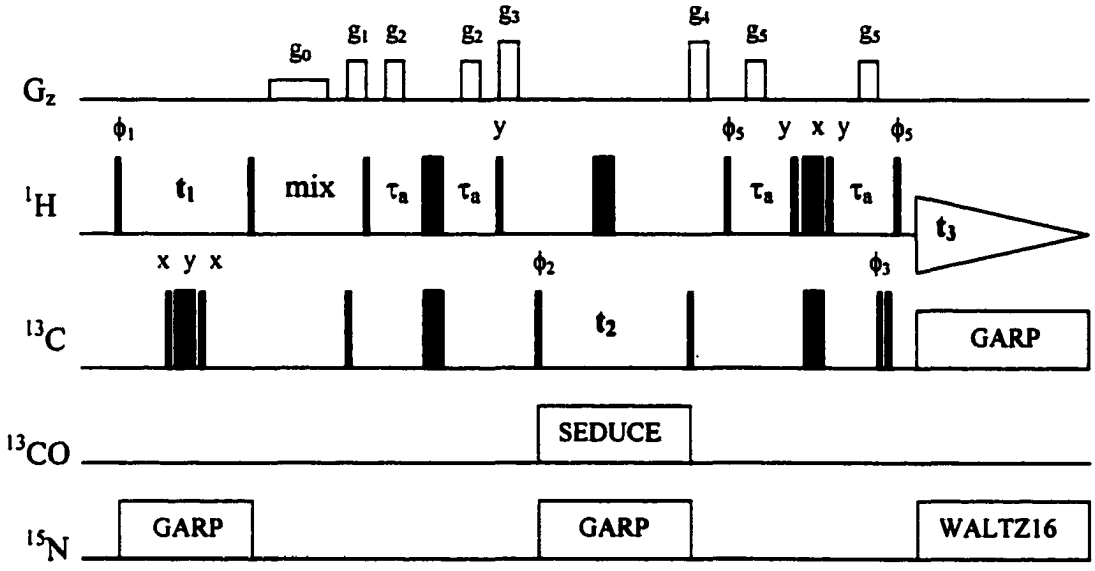

Figure 5.7

Figure 5.8 An illustration of NOE assignments made from noesy3Dn and cn4Dnoesy spectra using NMRView. The assignment of crosspeak #875 in the 3D spectrum to Ser^{4}HN-His^{43}Hβ1 (2.52 ppm) is confirmed by crosspeak #1019 of the 4D spectrum located at the correct ^{13}Cβ shift of 34.7 ppm.

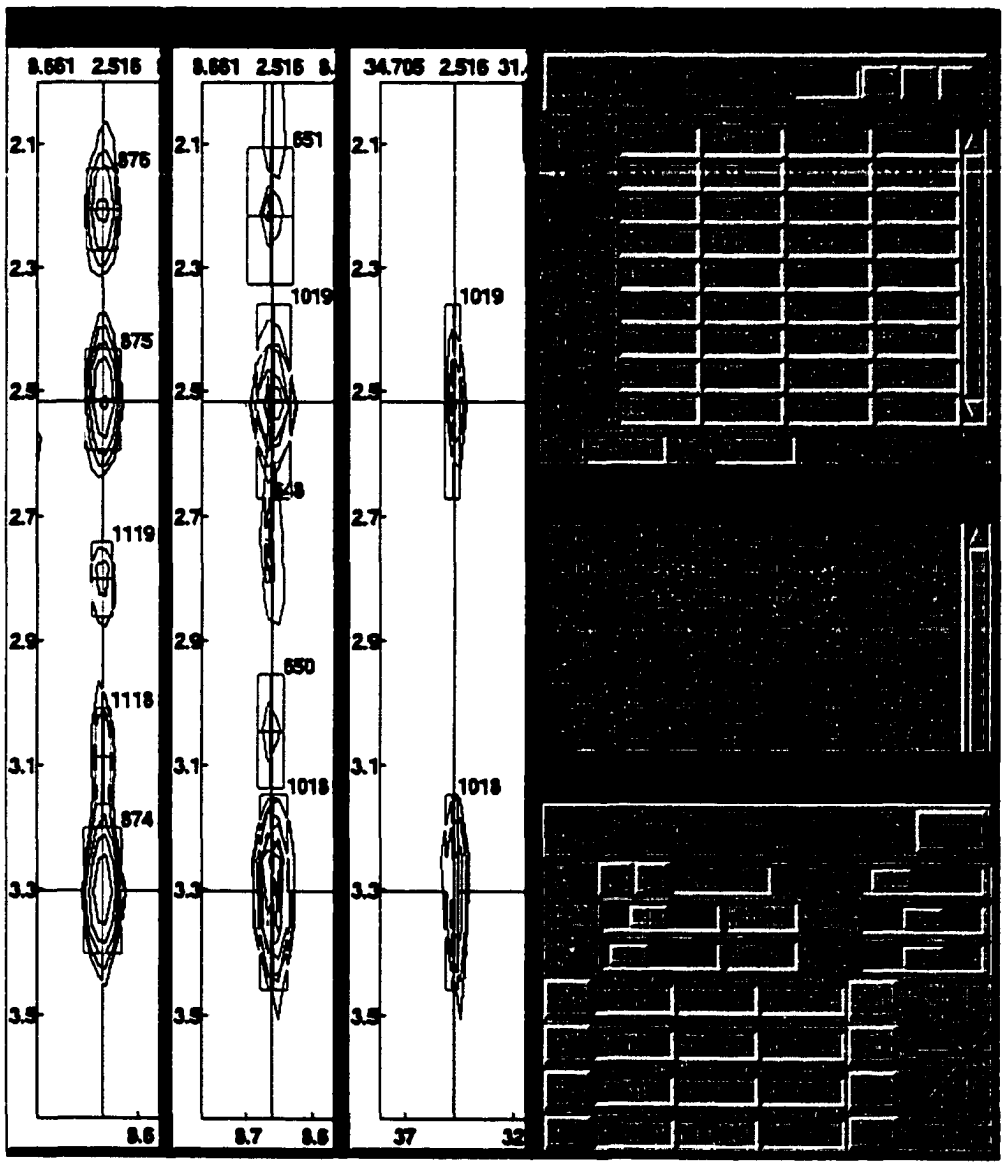

Figure 5.8

Figure 5.9 β-sheet network assembled from backbone NOE connectivities derived from five NOESY experiments (**Table 5.4**).

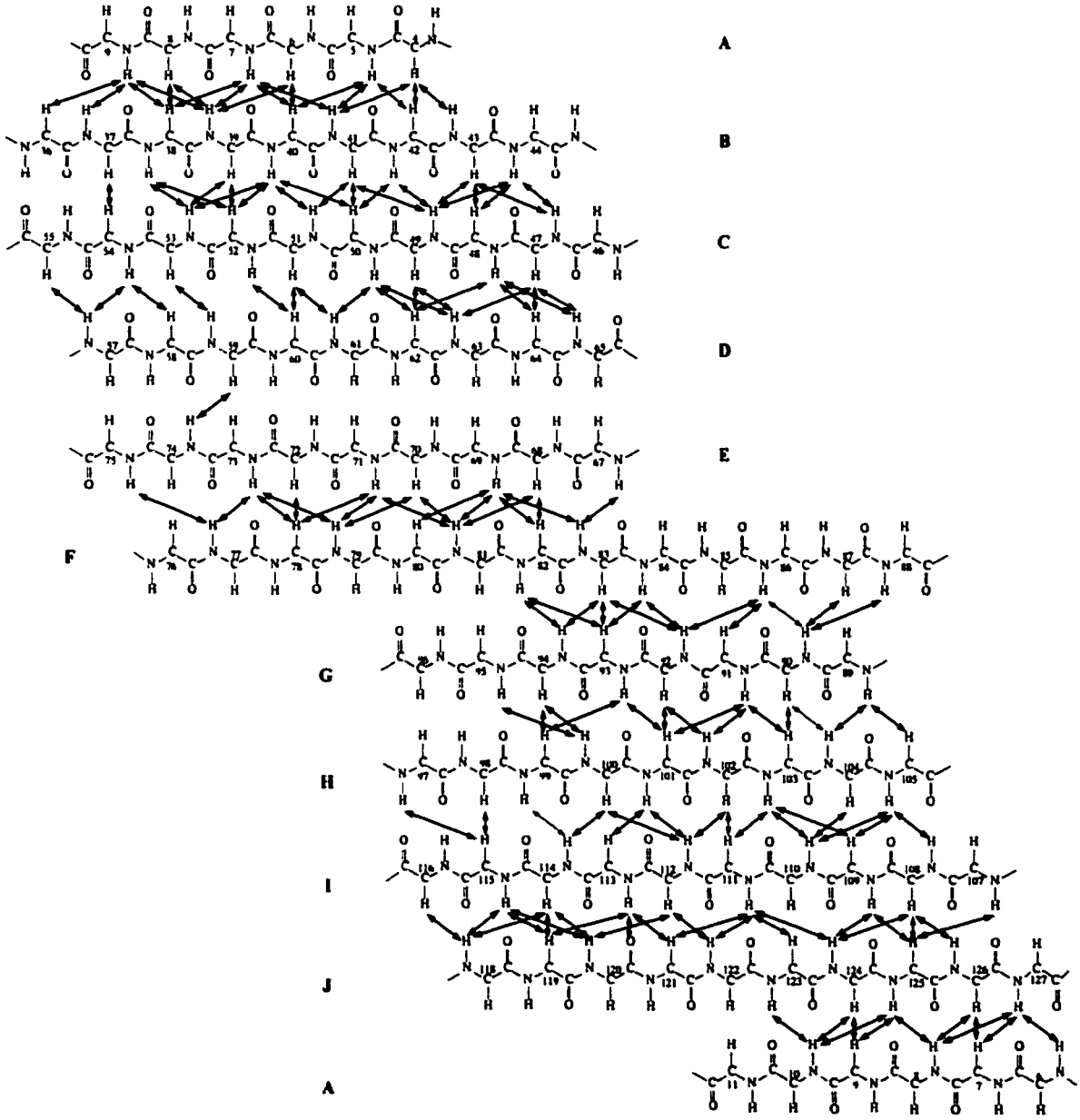

Figure 5.9

Figure 5.10 The LFABP β barrel, showing the 10 β strands. The vertical lines indicate hydrogen bonds linking the labeled β-strands. As for **Fig. 5.9**, backbone NOE connectivities from five NOESY experiments were used to derive the β-sheet network.

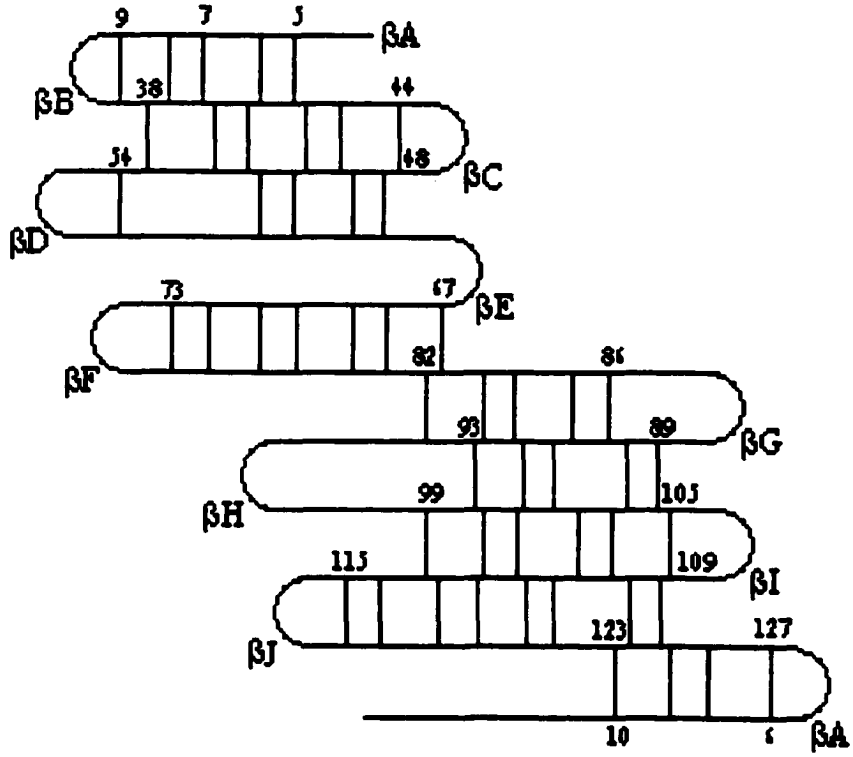

Figure 5.10

Figure 5.11 Amino acid sequence and summary of strong and weak NOEs, used to delineate the sequential and medium-range NOEs and to identify elements of regular secondary structure in 2 oleate-bound holo-LFABP. The residues with slow H/D exchange rates (amide protons remained one week after the addition of D_2O) are indicated with filled circles.

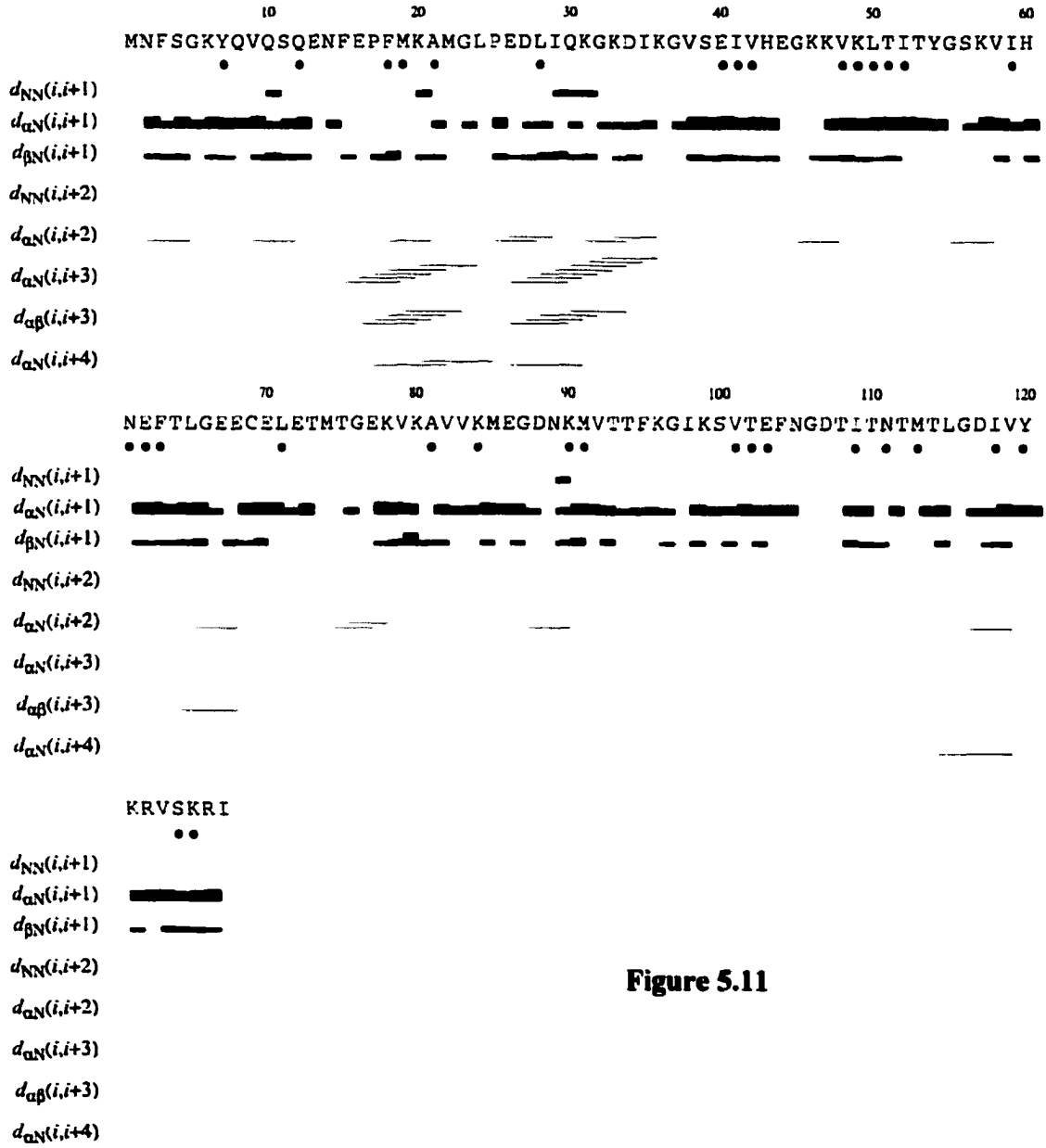

Figure 5.11

Figure 5.12 Schematic representation of the functions of the programs CALIBA, HABAS, DYANA, and MOLMOL. See the text for details.

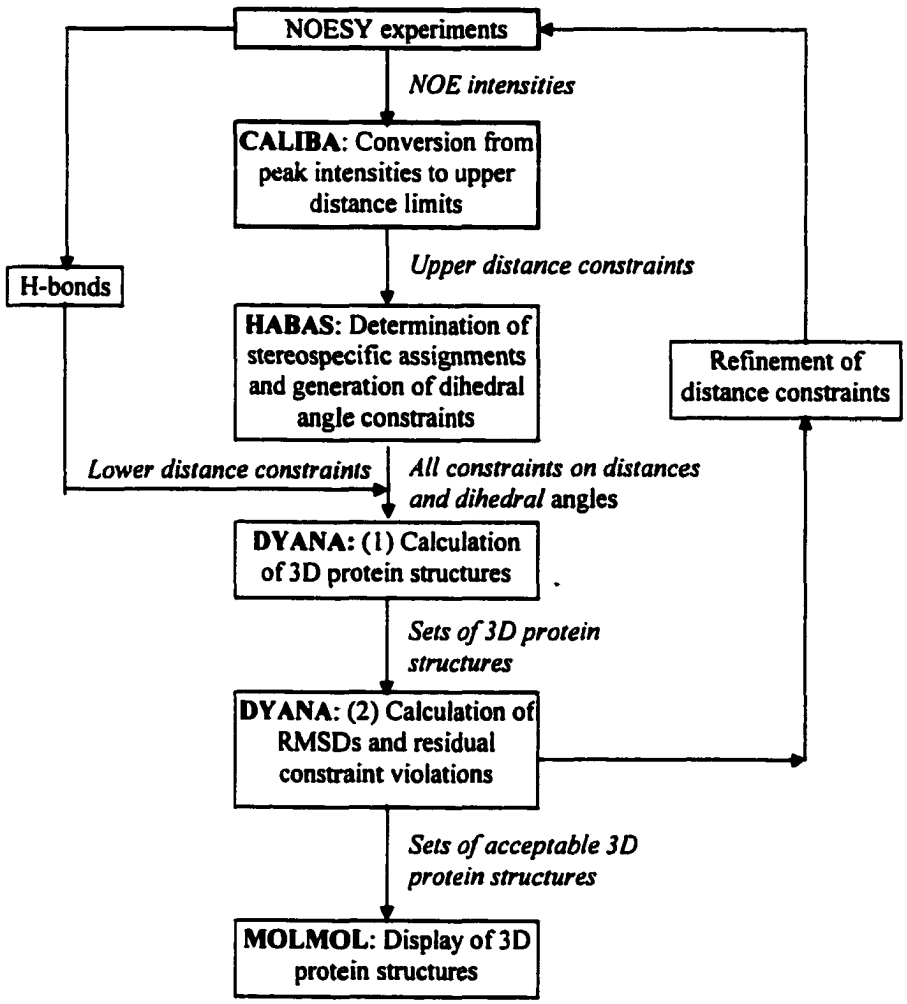

Figure 5.12

Figure 5.13 (a) Distribution of the unique distance restraints used to obtain the final 20 solution structures for 2 oleate-bound holo-LFABP. The CSI-derived secondary structure is shown at the bottom of the chart. (b) RMS deviations of the backbone coordinates of the 15 best conformations relative to their mean coordinates calculated by the MOLMOL program.

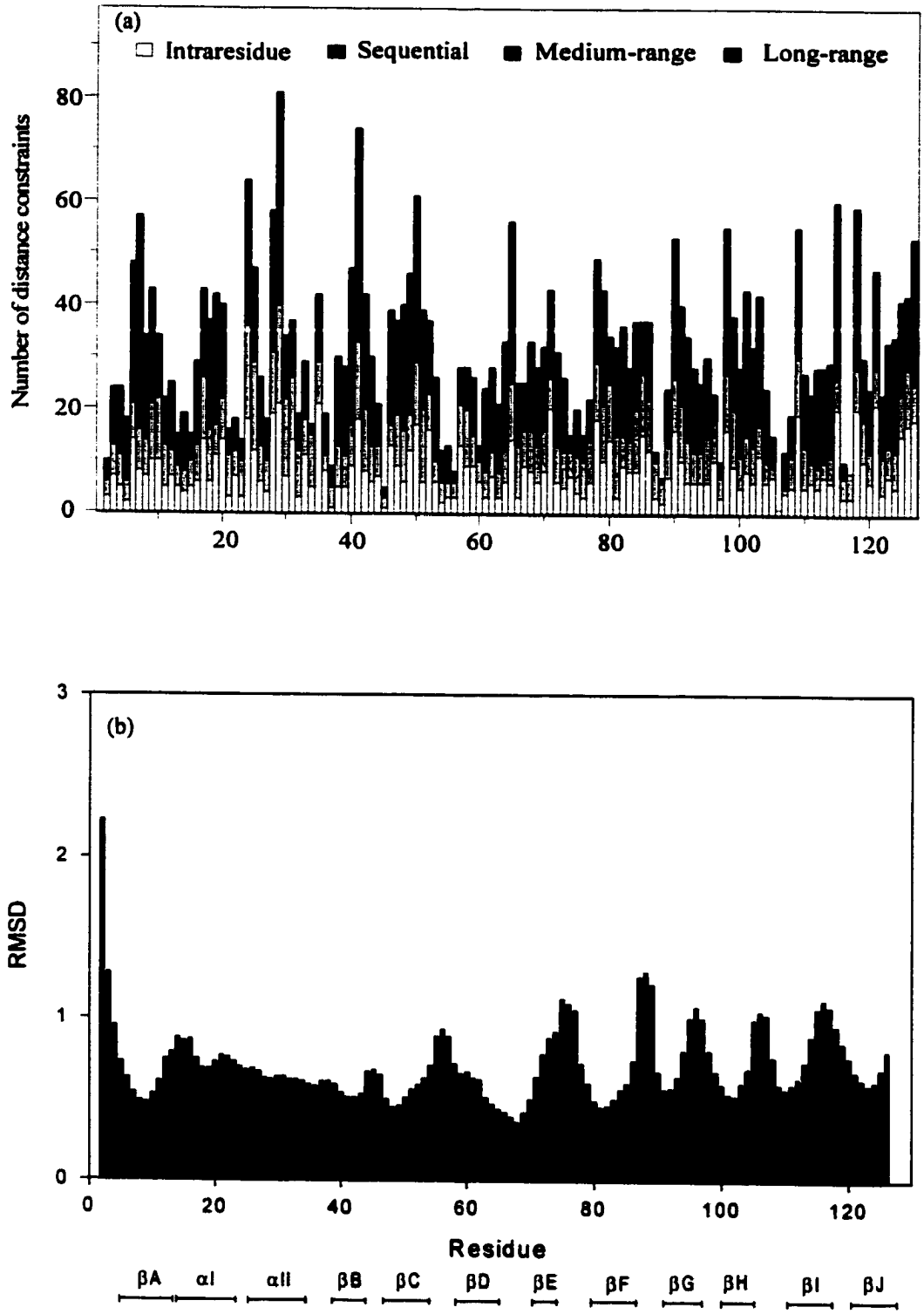

Figure 5.13

Figure 5.14 Diagram of 15 superimposed backbone C^{α} traces representing the final ensemble of NMR structures for 2 oleate-bound holo-LFABP.

Figure 5.15 A ribbon drawing showing the DYANA structure of 2 oleate-bound holo-LFABP with the fewest violations of the NOE distance constraints (lowest target function) after simulated annealing. The 10 β-strands are indicated by capital letters A, B, C, etc. The X-ray crystal structure is also shown for comparison.

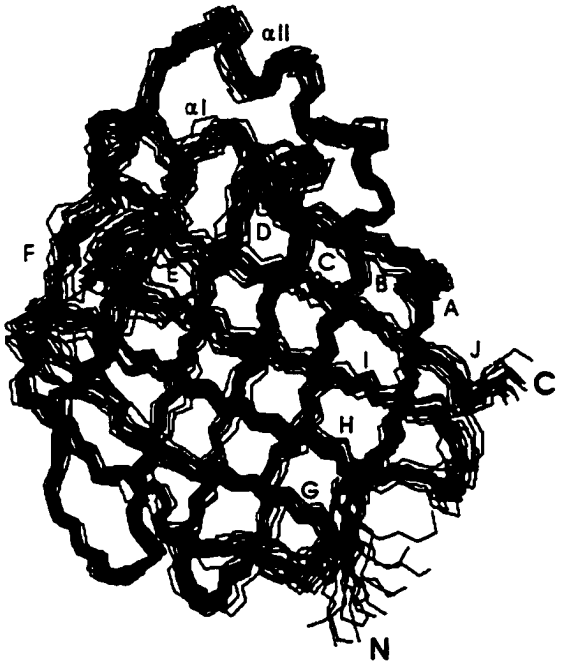

Figure 5.14

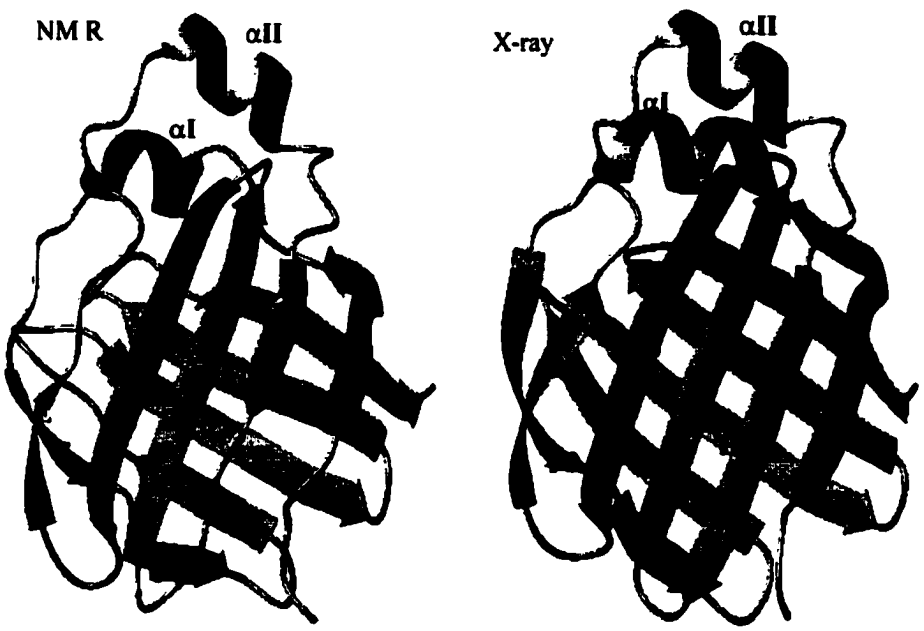

Figure 5.15

Figure 5.16 A portion of the β-sheet network built up by ^{1}H-^{1}H NOEs derived from both apo- and 2 oleate-bound holo-LFABP. Adding fatty acid enhances the LFABP β-sheet structure.

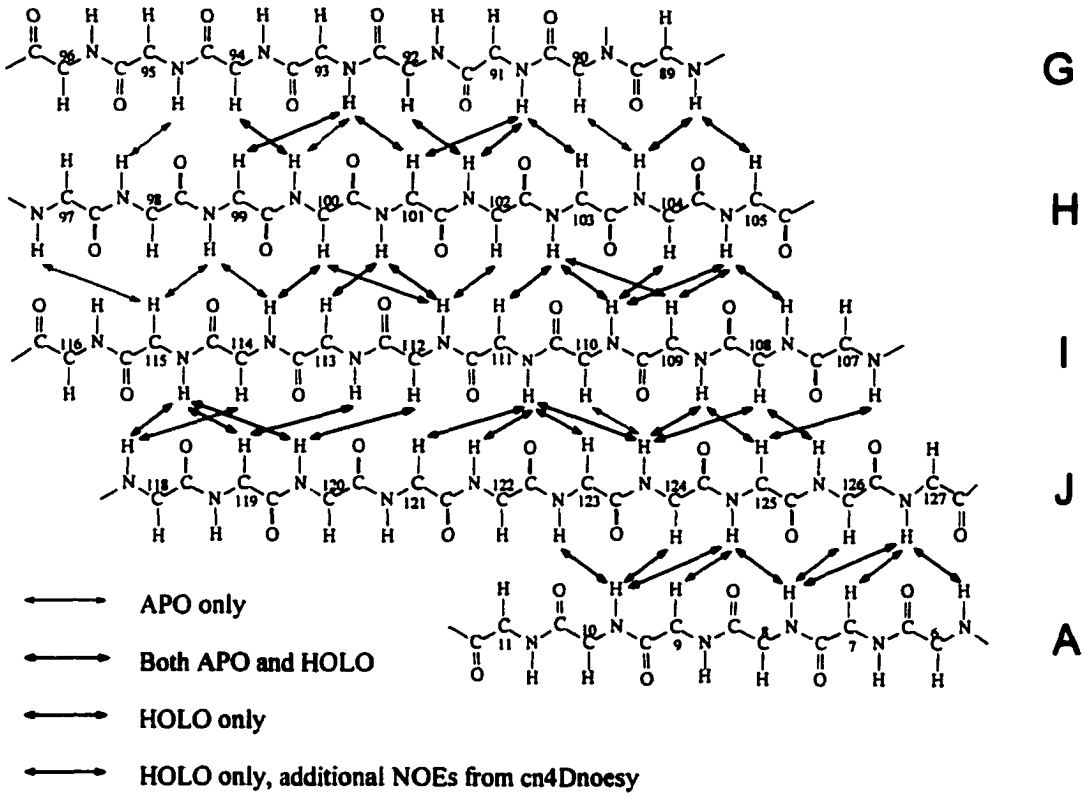

Figure 5.16

Figure 5.17 A view of interactions between LFABP and the two bound oleates. Residues L24, L28, I29, G32, I35, Y54, and I59 interact with OLA128. Residues I41, V48, L50, F63, L71, T73, V83, T93, F95, I98, T102, I109, M113, Y120, and S124 interact with OLA129. The head groups of oleates are labeled as "COOH".

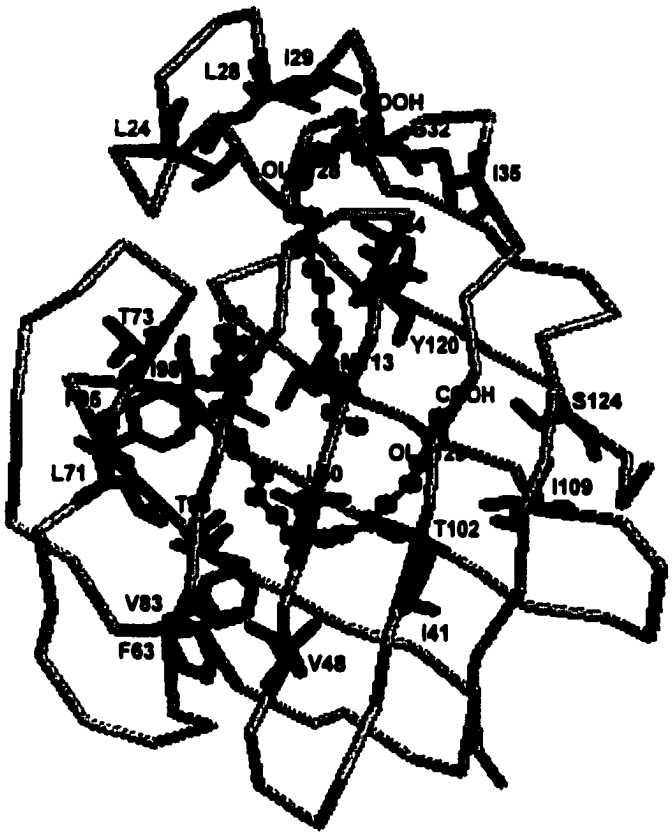

Figure 5.17

Table 5.2 ^{1}H, ^{15}N and ^{13}C chemical shifts for a complex of rat LFABP with unlabeled oleate (1:2) at pH 7.0 and 30 °C.

Table 5.2

Spin	^{15}N	^{1}HN	$^{13}C'$	$^{1}H^{\alpha}$	$^{13}C^{\alpha}$	$^{1}H^{\beta}$	$^{13}C^{\beta}$	Other ^{1}H	Other ^{13}C	NH_2 & NH (sc)	$^{13}C'$(sc)	Aromatic ring
Asn[2]			176.1	4.76	52.2	2.80 2.54	40.5			δ 116.6 7.55,7.07	γ 177.6	
Phe[3]	131.8	11.3	176.8	4.51	57.2	3.08 2.21	38.8					H^{δ} 6.15 H^{ε} 6.82
Ser[4]	118.3	8.67	174.2	4.42	61.1	4.13 3.98	64.5					
Gly[5]	113.0	9.10	169.9	4.01 3.89	45.3							
Lys[6]	123.2	8.22	174.3	5.08	55.6	1.61	34.9	γ 1.35,1.19; δ 1.61; ε 2.86	γ 26.1; δ 29.8; ε 42.1			
Tyr[7]	123.7	9.19	174.1	5.20	56.3	2.68 2.51	42.1					H^{δ} 6.72 H^{ε} 6.58
Gln[8]	123.2	9.03	176.3	5.40	54.0	1.97 1.87	33.6	γ 2.34,2.28	γ 34.2	ε 113.8 7.30,6.85	δ 180.2	
Val[9]	132.7	8.48	175.1	4.14	64.7	1.88	33.0	γ^1 0.96; γ^2 0.86	γ^1 22.4; γ^2 21.2			
Gln[10]	128.2	10.1	176.3	4.49	55.9	2.17 1.92	31.8	γ 2.40	γ 34.6	ε 115.8 7.23,7.15	δ 179.7	
Ser[11]	114.4	8.07	172.1	4.74	57.6	3.85 3.79	65.4					
Gln[12]	119.7	8.53	174.7	5.49	54.8	2.36 2.26	34.1	γ 2.52	γ 35.1	ε 115.1 7.79,6.41	δ 180.6	
Glu[13]	122.7	9.05	176.0	4.85	55.5	2.13 1.90	34.0	γ 2.28	γ 36.3		δ 183.6	
Asn[14]	119.0	9.29	174.4	4.51	54.9	3.76 3.13	36.3			δ 116.0 7.91,7.09	γ 178.5	
Phe[15]	120.7	8.54	176.3	3.57	62.5	3.01	40.5					H^{δ} 7.00 H^{ε} 6.71
Glu[16]	118.8	9.58	175.2	3.73	62.4	2.16	27.2	γ 2.27	γ 38.1		δ 183.1	
Pro[17]			179.7	4.21	65.7	2.32 1.73	31.1	γ 2.08; δ 3.69,3.59	γ 28.3; δ 40.7			
Phe[18]	120.2	7.24	176.1	3.88	62.4	2.94 2.73	40.4					H^{δ} 7.29 H^{ε} 7.35
Met[19]	117.8	8.23	179.5	3.99	56.7	1.56 1.35	31.6	γ 1.76, 1.49	γ 33.0			
Lys[20]	122.2	8.31	180.7	3.93	59.6	1.74	32.5	γ 1.46,1.32; δ 1.61; ε 2.90	γ 25.7; δ 29.3; ε 42.3			
Ala[21]	125.7	7.56	179.5	4.00	54.9	1.29	18.0					
Met[22]	117.2	7.48	176.5	4.16	55.4	2.16 2.08	32.4	γ 1.88,1.83	γ 32.6			
Gly[23]	108.4	7.61	175.2	4.09 3.66	45.4							
Leu[24]	125.6	7.58	174.2	4.30	53.8	1.38 1.13	42.2	γ 1.63; δ^1 0.81; δ^2 0.71	γ 27.9; $\delta^1$25.4; δ^2 24.9			
Pro[25]			177.9	4.41	63.0	2.45 2.03	33.0	γ 2.11; δ 3.99,3.44	γ 28.2; δ 51.0			
Glu[26]	124.7	8.77	178.2	3.82	60.2	2.06	30.0	γ 2.33	γ 36.5		δ 183.4	
Asp[27]	118.5	8.89	178.7	4.35	57.1	2.65 2.60	40.1				γ 179.7	
Leu[28]	121.5	7.18	179.2	4.19	57.5	1.79 1.46	42.0	γ 1.72; $\delta^1$0.91; δ^2 0.85	γ 27.5; $\delta^1$25.5; δ^2 23.8			
Ile[29]	122.4	7.74	177.9	3.49	66.6	1.99	38.0	γ^1 1.65,0.35; γ^2 0.87; δ 0.65	γ^1 29.9; $\gamma^2$17.7; δ 13.6			
Gln[30]	118.3	8.08	178.9	3.93	59.0	2.16	28.2	γ 2.50	γ 33.7	ε 115.8 7.70,6.95	δ 180.3	
Lys[31]	118.9	7.63	179.1	4.19	59.1	1.85 1.72	33.8	γ 1.70,1.53; δ 1.62; ε 2.98	γ 26.1; δ 29.6; ε 42.6			
Gly[32]	107.0	8.43	175.2	3.98 3.60	46.9							

Table 5.2 --- *Continued.*

Spin	^{15}N	^{1}HN	$^{13}C'$	$^{1}H^{\alpha}$	$^{13}C^{\alpha}$	$^{1}H^{\beta}$	$^{13}C^{\beta}$	Other ^{1}H	Other ^{13}C	NH_2 & NH (sc)	$^{13}C'$(sc)	Aromatic ring
Lys[33]	121.3	7.71	176.5	3.33	59.1	1.85	32.5	γ 1.53,1.44; δ 1.69	γ 24.1; δ 30.1; ε 42.5			
Asp[34]	119.1	7.53	176.2	4.80	54.8	2.85 2.50	42.3				γ 180.2	
Ile[35]	122.7	7.38	176.0	3.98	61.5	1.86	39.6	γ^1 1.74,1.11; γ^2 0.62; δ 0.87	γ^1 27.9; $\gamma^2$17.5; δ 14.1			
Lys[36]	130.4	8.67	175.9	4.26	55.1	1.80	30.8	γ 1.48,1.30; δ 1.62; ε 2.99	γ 24.8; δ 29.2; ε 42.1			
Gly[37]	113.7	7.06	171.7	3.51 3.02	45.4							
Val[38]	120.9	7.79	176.0	5.04	61.0	1.91	35.8	γ^1 0.95; γ^2 0.95	γ^1 21.0; γ^2 21.0			
Ser[39]	126.5	9.32	172.8	5.53	56.9	3.77 3.65	65.6				δ 182.8	
Glu[40]	126.7	9.51	175.3	5.33	55.3	2.14 1.89	33.0	γ2.19,2.08	γ 37.2			
Ile[41]	128.2	9.64	176.7	5.12	60.5	2.22	41.1	γ^1 1.73,0.97; γ^2 0.79; δ 0.89	γ^1 28.4; $\gamma^2$18.2; δ 14.3			
Val[42]	132.4	9.35	173.9	4.21	63.4	2.05	33.5	γ^1 0.93;,γ^2 0.98	γ^1 21.0; γ^2 20.6			
His[43]	133.8	8.96	174.1	5.52	53.1	3.31 2.52	34.7					H^{δ} 6.63
Glu[44]	132.6	8.93	175.9	4.33	54.9	1.89 1.82	32.0	γ 2.04	γ 36.2		δ 184.0	
Gly[45]	119.4	8.60	174.4	3.97 3.53	47.5							
Lys[46]	127.7	8.87	175.0	4.57	56.5	2.24 1.85	33.7	γ 1.59,1.53; δ 1.77; ε 3.02	γ 25.8; δ 29.8; ε 42.3			
Lys[47]	122.6	8.19	175.5	4.76	56.3	1.91	34.0	γ 1.41; δ 1.65; ε 2.90	γ 25.2; δ 29.2; ε 42.1			
Val[48]	127.0	8.73	174.1	4.51	61.3	0.54	33.9	γ^1 0.39; γ^2 0.46	γ^1 22.0; γ^2 21.4			
Lys[49]	127.2	8.73	174.7	4.77	55.3	1.81	34.7	γ 1.45,1.33; δ 1.64; ε 2.88	γ 25.3; δ 30.0; ε 42.2			
Leu[50]	128.9	9.04	175.5	5.45	53.4	1.73 1.16	46.8	γ 1.53; $\delta^1$0.93; δ^2 0.92	γ 28.1; $\delta^1$27.5; δ^2 24.0			
Thr[51]	129.2	9.53	173.8	5.23	62.4	4.05	70.9	γ 1.12	γ 22.6			
Ile[52]	132.3	9.10	174.5	4.94	60.6	1.78	41.2	γ^1 1.53,1.41; γ^2 1.04; δ 0.87	γ^1 27.2; $\gamma^2$17.3; δ 14.4			
Thr[53]	125.7	9.16	174.0	5.11	62.7	3.96	70.5	γ 1.15	γ 21.5			
Tyr[54]	133.5	9.39	175.2	4.46	57.3	2.91 2.76	41.7					
Gly[55]	115.5	8.74	174.8	4.05 3.59	47.3							
Ser[56]	124.9	9.08	174.2	4.34	59.2	4.04 3.90	64.1					
Lys[57]	127.8	8.31	173.7	4.50	55.7	2.15 1.86	33.1	γ 1.38; δ 1.71; ε 2.99	γ 25.1; δ 28.8; ε 42.4			
Val[58]	128.8	8.31	176.2	5.00	61.1	1.85	34.5	γ^1 0.67; γ^2 0.88	γ^1 21.4; γ^2 21.4			
Ile[59]	129.0	9.23	175.7	4.43	60.5	1.70	41.1	γ^1 1.55,1.47; γ^2 0.72; δ 0.81	γ^1 28.4; $\gamma^2$18.5; δ 14.3			
His[60]	132.4	9.35	173.6	5.38	55.9	3.14 2.94	32.8					H^{δ} 7.04
Asn[61]	123.9	8.66	173.2	5.16	53.4	2.49	45.6			δ 116.0 7.83,7.61	γ 177.2	
Glu[62]	122.4	8.95	174.1	5.21	55.5	2.00	32.9	γ 2.19,2.11	γ 36.4		δ 183.6	
Phe[63]	120.9	8.62	173.0	5.10	56.1	3.22	41.3					H^{δ} 6.64 H^{ε} 6.85
Thr[64]	119.8	8.60	175.5	5.01	61.3	3.90	70.4	γ 1.21	γ 22.0			
Leu[65]	131.8	9.62	178.2	4.42	57.1	1.90 1.60	42.4	γ 1.84; δ^1 0.98; δ^2 0.94	γ 27.7; $\delta^1$26.4; δ^2 26.4			
Gly[66]	111.2	9.49	173.6	4.40 3.45	45.8							

Table 5.2 --- *Continued.*

Spin	^{15}N	^{1}HN	$^{13}C'$	$^{1}H^{\alpha}$	$^{13}C^{\alpha}$	$^{1}H^{\beta}$	$^{13}C^{\beta}$	Other ^{1}H	Other ^{13}C	NH_2 & NH (sc)	$^{13}C'$ (sc)	Aromatic ring
Glu[67]	121.3	7.89	175.4	4.80	54.4	2.17 1.88	32.6	γ 2.23,2.18	γ 36.1		δ 183.4	
Glu[68]	126.7	8.94	176.0	4.45	58.0	2.02 1.94	30.5	γ 2.12	γ 37.8		δ 183.6	
Cys[69]	126.6	9.29	172.5	5.14	56.7	3.44 3.07	32.6					
Glu[70]	121.8	8.41	175.6	4.98	55.7	1.89	32.1	γ 2.16,1.98	γ 38.1		δ 183.5	
Leu[71]	127.8	9.08	175.4	4.63	53.2	1.23 0.84	44.4	γ 1.39; δ^1 0.17; δ^2 0.47	γ 26.4; $\delta^1$25.5; δ^2 23.4			
Glu[72]	126.5	9.82	176.5	4.82	55.6	1.93	31.7	γ 2.45,2.08	γ 36.9		δ 183.4	
Thr[73]	113.7	8.25	176.1	4.50	60.6	4.54	70.4	γ 1.04	γ 21.5			
Met[74]	116.9	8.32	175.5	4.22	59.1	2.14 1.92	31.0	γ 2.58,2.47	γ 33.3			
Thr[75]	108.9	7.83	175.7	4.34	61.7	4.55	69.2	γ 1.09	γ 22.1			
Gly[76]	112.1	7.61	173.8	4.36 3.80	45.3							
Glu[77]	123.2	7.29	175.5	4.19	56.4	1.82	30.7	γ 2.23,2.10	γ 36.3		δ 183.8	
Lys[78]	125.7	8.49	177.1	5.37	54.8	1.76 1.51	33.7	γ 1.51,1.31; δ 1.61; ε 2.99	γ 25.4; δ 29.1; ε 42.5			
Val[79]	121.2	9.05	174.3	4.62	59.2	2.03	35.0	γ^1 0.57; γ^2 0.79	γ^1 19.6; γ^2 21.8			
Lys[80]	125.3	8.35	176.4	5.06	55.8	1.79 1.69	33.5	γ 1.54,1.35; δ 1.63; ε 2.95	γ 25.6; δ 29.2; ε 42.2			
Ala[81]	127.7	8.87	175.1	4.86	51.6	1.18	23.5					
Val[82]	120.3	8.39	176.1	4.28	62.0	1.92	34.4	γ^1 0.85; γ^2 0.70	γ^1 21.0; γ^2 20.8			
Val[83]	136.4	9.76	175.1	4.48	61.5	1.66	31.9	γ^1 0.63; γ^2 –0.03	γ^1 22.0; γ^2 18.5			
Lys[84]	127.3	8.87	175.6	4.89	54.8	1.78	36.6	γ 1.36; δ 1.68; ε 2.94	γ 25.4; δ 29.7; ε 42.3			
Met[85]	121.6	8.77	177.3	5.40	54.3	2.79 2.61	32.5	γ 2.38,1.99	γ 32.4			
Glu[86]	128.5	8.64	175.7	4.57	56.1	1.87 1.74	32.4	γ 2.13,2.09	γ 36.8		δ 183.1	
Gly[87]	114.9	8.47	174.0	4.19 3.79	45.6							
Asp[88]	120.3	8.55	178.0	4.72	55.4	2.70	42.0				γ 180.1	
Asn[89]	116.0	8.11	174.1	5.14	53.4	3.75 2.81	40.1			γ 114.3 7.41,7.04	γ 179.1	
Lys[90]	119.4	7.35	175.7	5.97	54.9	2.13 1.59	36.6	γ 1.47,1.18; δ 1.50; ε 2.85	γ 25.4; δ 29.7; ε 42.1			
Met[91]	122.3	8.88	175.5	5.28	55.1	1.66	36.8	γ 2.42,2.10	γ 34.0			
Val[92]	123.7	9.35	175.0	5.28	60.2	2.00	35.7	γ^1 0.91; γ^2 0.94	γ^1 20.3; γ^2 20.3			
Thr[93]	121.2	8.80	172.3	4.86	61.9	4.06	69.5	γ 0.91	γ 18.8			
Thr[94]	119.4	8.02	173.4	5.45	59.8	4.06	71.6	γ 1.10	γ 20.4			
Phe[95]	123.5	8.17	173.5	4.85	56.6	3.30 2.71	40.1					H^{δ} 6.79 H^{ε} 6.91
Lys[96]	122.0	9.39	175.6	3.88	57.2	2.15	30.8	γ 1.56; ε 3.00 δ 1.76,1.64;	γ 25.8; δ 29.1; ε 41.9			
Gly[97]	106.9	8.39	173.8	4.00 3.54	45.6							
Ile[98]	125.2	8.35	176.1	4.42	60.6	1.55	39.5	$\gamma^1$1.54,0.81; $\gamma^2$0.71; δ 0.80	$\gamma^1$29.2;$\gamma^2$18.4; δ 15.1			
Lys[99]	128.7	8.22	175.5	4.86	55.4	1.84 1.69	34.4	γ 1.35,1.28; δ 1.61; ε 2.81	γ 25.5; δ 29.5; ε 42.2			
Ser[100]	123.7	8.94	174.0	5.40	56.8	3.68 3.33	64.9					
Val[101]	131.0	8.82	174.9	4.63	62.1	2.01	34.9	γ^1 0.94; γ^2 0.84	$\gamma^1$21.2; γ^2 21.2			
Thr[102]	130.0	9.28	173.0	4.82	62.1	3.68	70.0	γ 0.53	γ 23.5			

Table 5.2 --- *Continued.*

Spin	^{15}N	^{1}HN	$^{13}C'$	$^{1}H^{\alpha}$	$^{13}C^{\alpha}$	$^{1}H^{\beta}$	$^{13}C^{\beta}$	Other ^{1}H	Other ^{13}C	NH_2 & NH (sc)	$^{13}C'$ (sc)	Aromatic ring
Glu[103]	128.3	9.07	174.5	4.98	54.8	2.00 1.71	33.0	γ2.03,1.97	γ 37.2		δ183.2	
Phe[104]	128.1	8.79	175.5	4.49	57.6	2.89 2.66	40.3					
Asn[105]	125.6	8.42	175.4	5.09	52.5	2.82 2.59	40.2			δ114.8 7.51,7.03	γ177.7	
Gly[106]	115.1	8.48	174.4	4.22 3.67	47.9							
Asp[107]	128.7	8.76	175.2	4.80	54.9	2.99 2.89	41.7				γ180.6	
Thr[108]	114.9	7.85	173.5	5.33	61.4	4.11	72.5	γ 1.16	γ 21.4			
Ile[109]	125.9	8.71	175.5	4.60	60.2	1.05	41.3	γ^1 0.88, 0.18; γ^2 0.07;δ -0.38	γ^1 27.5;γ^2 18.6; δ 13.1			
Thr[110]	123.9	8.62	173.0	5.01	61.7	3.94	70.5	γ 1.05	γ 21.1			
Asn[111]	130.3	9.33	174.4	5.56	52.2	2.61 2.32	43.3			δ109.5 7.11,5.65	γ173.9	
Thr[112]	124.4	8.98	173.8	4.75	62.0	3.85	70.2	γ 0.96	γ 21.9			
Met[113]	129.6	9.23	174.0	5.43	54.6	1.78 1.56	37.1	γ 2.42,2.27	γ 33.2			
Thr[114]	120.1	8.91	173.7	5.29	61.7	4.00	71.0	γ 1.16	γ 21.6			
Leu[115]	132.1	8.94	176.3	4.65	54.3	1.68 1.26	44.9	γ 1.35;δ^1 0.47; δ^2 0.66	γ 27.8; $\delta^1$26.0; δ^2 23.1			
Gly[116]	119.7	9.04	174.4	3.93 3.61	47.7							
Asp[117]	128.3	8.64	175.8	4.60	54.3	2.74 2.69	41.2				γ180.8	
Ile[118]	124.5	8.32	174.5	4.07	61.9	2.21	39.2	$\gamma^1$1.71,1.05; $\gamma^2$0.97; δ 0.78	γ^1 27.4;γ^2 18.2; δ 14.0			
Val[119]	129.5	8.34	175.7	4.71	61.5	1.98	32.7	γ^1 0.86; γ^2 0.72	$\gamma^1$20.8;γ^2 21.7			
Tyr[120]	133.0	9.35	174.1	5.46	54.2	2.56 2.05	40.0					H^{δ}6.79 H^{ε} 6.91
Lys[121]	131.8	8.13	174.4	5.10	54.5	1.61 1.49	36.8	γ 1.27,1.11; δ 1.51; ε 2.71	γ 25.5; δ 29.6; ε 42.1			
Arg[122]	126.2	8.72	175.0	4.80	54.8	1.71 1.38	35.6	γ 1.39; δ 3.22	γ 26.9; δ 44.7	86.9;9.80		
Val[123]	128.3	8.82	175.9	4.96	62.0	2.07	33.7	γ^1 0.87; γ^2 0.87	$\gamma^1$21.1; γ^2 21.1			
Ser[124]	125.6	9.35	172.1	5.36	58.0	3.52 3.35	66.2					
Lys[125]	123.6	8.57	175.5	5.53	54.0	1.87 1.75	36.9	γ 1.55,1.47; δ 1.68; ε 2.96	γ 25.0; δ 29.4; ε 42.4			
Arg[126]	128.3	8.74	175.9	4.28	57.4	1.75	31.9	γ 1.60,1.42; δ 3.35,3.13	γ 27.4; δ 43.7	85.0;7.43		
Ile[127]	131.9	8.50	180.8	4.20	63.0	1.85	40.5	$\gamma^1$1.21,0.79; $\gamma^2$0.90; δ 0.79	γ^1 27.5;γ^2 18.8; δ 14.5			

Table 5.6 Intermolecular NOE assignments from two data sets (see text). The carbon chemical shifts for both protein and ligand are shown after their respective attached proton shifts.

Table 5.6

OLA128 (assignment: $^{1}H/^{13}C$ ppm)	LFABP (assignment: $^{1}H/^{13}C$ ppm)
CH12-15: 1.220 / 32.44	L24 HD11/CD1: 0.855 / 25.68
CH12-15: 1.221	L24 HD21/CD2: 0.759 / 25.09
CH5: 0.999 /32.31	L28 HD21/CD2: 0.896 / 23.85
CH7: 1.214	L28 HD21/CD2: 0.895 / 23.86
CH7: 1.231	L28 HD11/CD1: 0.963 / 25.66
CH8: 1.604 / 29.31	L28 HD21: 0.859
CH8: 1.640 / 29.67	L28 HB1: 1.494
CH9,10: 5.259	I29 HG21/CG2: 0.894 / 16.13
CH15: 1.135 / 32.38	I29 HG12: 1.621
CH7: 1.217	G32 HA1/CA: 3.643 / 46.88
CH4: 1.154 / 32.27	I35 HB/CB: 1.932 / 39.48
CH4: 1.194	I35 HD11/CD1: 0.909 / 14.70
CH6: 1.056 / 33.89	I35 HB: 1.952
CH12-15: 1.162 / 32.46	Y54 HE: 6.871 / 117.97
CH15: 1.148 / 32.65	I59 HB/CB: 1.700 / 41.69
CH17: 1.146 / 25.30	I59 HD11/CD1: 0.826 / 14.79
CH18: 0.767 / 16.78	I59 HD11/CD1: 0.819 / 14.71
CH18: 0.771 / 17.20	I59 HG21: 0.715
OLA129 (assignment: $^{1}H/^{13}C$ ppm)	**LFABP (assignment: $^{1}H/^{13}C$ ppm)**
CH4: 1.229	I41 HG12/CG1: 1.767 / 28.81
CH5: 1.196	I41 HG21/CG2: 0.798 / 18.49
CH6: 1.235	V48 HG21/CG2: 0.437 / 22.55
CH6: 1.219	L50 HD11/CD1: 0.974 / 27.54
CH4: 1.223	L50 HD21/CD2: 0.959 / 24.16
CH12: 1.132 / 31.80	F63 HD: 6.636
CH12: 1.140 / 32.44	L71 HD21/CD2: 0.507 / 23.61
CH12: 1.149	L71 HD11/CD1: 0.207 / 25.78
CH14: 1.100	L71 HD11/CD1: 0.203 / 25.79
CH17: 1.174	T73 HA/CA: 4.551 / 60.54
CH17: 1.179	T73 HB/CB: 4.589 / 70.29
CH12: 1.156	V83 HG11/CG1: 0.020 / 18.77
CH9: 5.201	V83 HG11/CG1: 0.016 / 18.81
CH7: 1.192	V83 HG21/CG2: 0.663 / 22.20
CH8: 1.639 / 29.24	V83 HG21: 0.661
CH9: 5.205	V83 HG21/CG2: 0.668 / 22.18
CH12: 1.216	T93 HB/CB: 4.036 / 68.68
CH12: 1.186	T93 HG21/CG2: 0.960 / 19.05
CH13: 1.145	T93 HG21/CG2: 0.958 / 18.94
CH15: 1.149 / 32.83	F95 HE: 6.956
CH16: 1.059 / 34.99	I98 HD11: 0.825
CH17: 1.175	I98 HG21/CG2: 0.765 / 18.47
CH18: 0.788 / 16.82	I98 HG21/CG2: 0.780 / 18.47
CH18: 0.791 / 16.82	I98 HD11/CD1: 0.820 / 14.76
CH7: 1.230	T102 HG21/CG2: 0.591 / 23.87
CH4: 1.229	I109 HG21/CG2: 0.127 / 18.90
CH5: 1.206	I109 HG21/CG2: 0.120 / 18.86
CH10: 5.217	M113 HB2/CB: 1.777 / 38.48
CH17: 1.171	Y120 HE/CE: 6.561 / 116.57
CH16: 1.121 / 32.31	Y120 HB1/CB: 2.062 / 40.07
CH17: 1.204	Y120 HB1/CB: 2.062 / 40.05
CH181: 0.783	Y120 HB1/CB: 2.062 / 40.10
CH182: 0.808	Y120 HB1/CB: 2.106 / 40.03
CH3: 1.194	S124 HB1/CB: 3.263 / 66.54

CHAPTER 6

DYNAMICS OF APO- AND HOLO-LFABP

6.1 Introduction

Multidimensional NMR methods (combined with isotope labeling) have been applied not only for the determination of protein structure but also to obtain a complete picture of protein dynamics on time scales from picoseconds up to milliseconds[26]. Molecular dynamics studies by NMR have offered time-dependent structural information on proteins, permitted identification of the binding site through changes in flexibility and order upon ligand binding, and therefore became important for functional understanding.

Two-dimensional NMR relaxation studies have permitted the characterization of backbone dynamics in a variety of proteins. Extraction of information about the dynamics of a protein from heteronuclear (^{15}N or ^{13}C) NMR relaxation studies is typically based on the measurement of heteronuclear longitudinal (R_1) and transverse (R_2) relaxation data and the steady-state ^1H-X (X = ^{15}N or ^{13}C) heteronuclear NOE. These three parameters are sensitive to the motion of the bond connecting the heteronucleus to its attached proton at prescribed frequencies, which are in turn related to the ^1H and X nuclear Larmor frequencies. More specifically, the relaxation parameters are related to the spectral density function, $J(\omega)$, characterizing the motion of the ^1H-X bond at the five frequencies ω=0, ω_X, ω_H, and $\omega_H \pm \omega_X$, where ω_i is the Larmor frequency of spin i. The ***Modelfree*** program, written by Prof. Arthur G. Palmer at Columbia University, is a program designed to fit the extended model free spectral density function (defined below) to NMR spin relaxation data. Four parameters are generated by the *Modelfree* program. S^2, the square of the generalized order parameter, characterizes the

degree of spatial restriction of the internal motions of the ^{1}H-X bond vector on the picosecond-to-nanosecond (ps-ns) time scale and reflects the angular restrictions for motions in various protein sites. τ_m, the rotational correlation time, describes the overall tumbling motion of the entire molecule. τ_e, the effective correlation time at each backbone site, results from internal motion. R_{ex}, the exchange term, measures the contribution to R_2 from motions that cause conformational exchange on a microsecond-to-millisecond time scale.

Amide ^{15}N relaxation measurements on apo- and holo-LFABP were conducted, and the backbone dynamics of both liganded and unliganded LFABP have been characterized. As expected from linewidth trends presented in Chapter 4, the addition of ligand made the protein less flexible.

6.2 Theory and Methods

6.2.1 Spectral density function

Relaxation of protonated heteronuclei is dominated by the dipolar interaction with the directly attached proton spin and by the chemical shift anisotropy interaction. In solution, motions about the N-H bond axis are responsible for the strength of the dipolar interaction and, hence, the relaxation of the amide ^{15}N. The motions are characterized by a set of spectral density functions, $J(\omega)$, evaluated at five distinct frequencies: $J(0)$, $J(\omega_H)$, $J(\omega_N)$, and $J(\omega_H \pm \omega_N)$. The dependence of the measured parameters, ^{15}N R_1, R_2, and NOE, on the spectral density functions is given by following relationships[26].

$$R_1 = (d^2/4)[J(\omega_H-\omega_N) + 3J(\omega_N) + 6J(\omega_H+\omega_N)] + c^2J(\omega_N) \quad (1)$$

$$R_2 = (d^2/8)[4J(0) + J(\omega_H-\omega_N) + 3J(\omega_N) + 6J(\omega_H) + 6J(\omega_H+\omega_N)]$$

$$+ (c^2/6)4[J(0) + 3J(\omega_N)] + R_{ex} \quad (2)$$

$$NOE = 1 + (d^2/4R_1)(\gamma_H/\gamma_N)[6J(\omega_H+\omega_N) - J(\omega_H-\omega_N)] \quad (3)$$

The constants d and c are defined as

$$d = \mu_0 h \gamma_N \gamma_H \langle r_{NH}^{-3} \rangle / (8\pi^2) \quad (4)$$

$$c = \omega_N \Delta\sigma / (3^{1/2}) \quad (5)$$

where μ_0 is the permeability of free space, h is Planck's constant, γ_H and γ_N are the gyromagnetic ratios of the ^1H and ^{15}N nuclei, respectively, ω_H and ω_N are their Larmor precessional frequencies, respectively, $\langle r_{NH} \rangle$ is the mean nitrogen-hydrogen bond length (1.02 Å), and $\Delta\sigma$ is the chemical shift anisotropy measured for ^{15}N nuclei in helical polypeptide chains (-172 ppm)[101].

The model-free formalism, as described by Lipari and Szabo[102,103] and extended by Clore and co-workers[104], determines the amplitudes and time scales of the intramolecular motions by recasting the spectral density function, J(ω). For an isotropic diffusion model, J(ω) is defined as

$$J(\omega) = S^2\tau_m/(1 + \omega^2\tau_m^2) + (1 - S^2)\tau/(1 + \omega^2\tau^2) \quad (6a)$$

in which $\tau = \tau_s\tau_m / (\tau_s + \tau_m)$, τ_m is the isotropic overall rotational correlation time of the molecule, τ_s (or τ_e) is the effective correlation time for internal motions, $S^2 = S_f^2S_s^2$ is the square of the generalized order parameter characterizing the angular excursions of the internal motions, and S_f^2 and S_s^2 are the squares of the order parameters for the internal motions on the fast and slow time scales, respectively. For an axially symmetric rotor, J(ω) is given by[105,106]:

$$J(\omega) = \sum_{k=1}^{3} A_k\{S^2\tau_k/(1 + \omega^2\tau_k^2) + (1 - S^2)\tau_k'/(1 + \omega^2\tau_k'^2)\} \quad (6b)$$

in which $A_1 = (3\cos^2\theta - 1)^2/4$, $A_2 = 3\sin^2\theta\cos^2\theta$, $A_3 = (3/4)\sin^4\theta$, $\tau_1 = (6D_\perp)^{-1}$, $\tau_2 = (D_\parallel + 5D_\perp)^{-1}$, $\tau_3 = (4D_\parallel + 2D_\perp)^{-1}$, $\tau_k' = (\tau_k\tau_e)/(\tau_k + \tau_e)$. τ_e is the effective correlation time for internal motions, $D_\parallel$ and $D_\perp$ are the rotational diffusion constants parallel and perpendicular to the symmetry axis of an axially symmetric rotational diffusion tensor, and θ is the angle between the symmetry axis of the diffusion tensor and the H-N bond vector. Generalized order parameters represent motions that are described by dynamics on the ps-ns time scale, with values ranging from zero for isotropic internal motions to unity for completely restricted motion in a molecular reference frame.

6.2.2 *Modelfree* program

The program *Modelfree* (Version 4.0)[107,108] has been widely used to determine the model free parameters from the three measured quantities R_1, R_2, and NOE. Four parameters, S^2, τ_m, τ_e, and R_{ex}, can be obtained from the output file by running *Modelfree*. The analysis of relaxation data using *Modelfree* involves at least three steps: initial estimation of the rotational correlation time, τ_m, or diffusion tensor, model selection, and final optimization.

6.2.2.1 Input files To run *Modelfree*, five input files are needed.

(1) *Modelfree* parameter file (**mfpar**) designates the nuclear spin (^{15}N), gyromagnetic ratio, N-H bond length, and chemical shift anisotropy for each residue.

(2) *Modelfree* data file (**mfdata**) inputs the measurements of R_1, R_2, and NOE.

(3) *Modelfree* in file (**mfin**) sets the type of weighting function applied to the relaxation data, diffusion tensor (isotropic or axial), parameters for grid search of internal motion, type of Monte Carlo simulations[109], and F-statistics option. The weighting function applied to the relaxation parameters, or total χ^2 variable, is given by

$$\chi^2=\sum_{i=1}^{n}SSE(i)=\sum_{i=1}^{n}\sum_{j=1}^{m}\{(R_{1ij}-\bar{R}_{1ij})^2/\sigma R_{1ij}^2+(R_{2ij}-\bar{R}_{2ij})^2/\sigma R_{2ij}^2+(NOE_{ij}-\overline{NOE_{ij}})^2/\sigma NOE_{ij}^2\} \quad (7)$$

in which R_{1ij}, R_{2ij}, and NOE_{ij} are the relaxation parameters for the ith spin and jth static magnetic field; $\bar{R}_{1ij}$, $\bar{R}_{2ij}$, and $\overline{NOE_{ij}}$ are the corresponding best-fit values; and σR_{1ij}, σR_{2ij}, and σNOE_{ij} are the experimental uncertainties in the relaxation parameters. The total number of spins to be analyzed is n, and the total number of static magnetic fields for which data are available is m. SSE(i), or gamma (Γ_i), is the sum-squared-error residual for the ith spin. The F-option controls whether F-statistics comparing two models should be generated. If we have Γ_1 for a first model with degree of freedom p_1 and Γ_2 for a second model with degree of freedom p_2, then the F-value can be calculated by

$$F = [(\Gamma_1 - \Gamma_2)\, p_2] / [\Gamma_2\, (p_1 - p_2)] \qquad \text{with } p_1 > p_2 \qquad (8).$$

(4) *Modelfree* model file (**mfmodel**) assigns one of five motional models to each spin. The five possible sets of at most three model-free parameters, which can be fit to three experimental data points for each residue, are described as follows (the "binary" short-hand notation given within parentheses below is also used by the *Modelfree* program as input to the –s flag):

Model_1:	(00100)	S_s^2
Model_2:	(00110)	S_s^2, τ_e
Model_3:	(00101)	S_s^2, R_{ex}

Model_4: (00111) S_s^2, τ_e, R_{ex}

Model_5: (01110) S_f^2, S_s^2, τ_e

(5) *Modelfree* structure file (**protein.pdb**) is a standard Protein Data Base (pdb) file containing atomic coordinates for heavy atoms and hydrogen atoms participating in any dipolar interactions for which relaxation data are to be analyzed.

6.2.2.2 Running Modelfree With the five input files prepared, the *Modelfree* program can be executed with the command "modelfree4 –p mfpar –d mfdata –i mfin –m mfmodel –s protein.pdb –o mfout", which generates an output file (**mfout**). The mfout file includes information on τ_m, S_s^2, S_f^2, τ_e, and R_{ex}, depending on the models selected in the mfmodel file.

6.2.2.3 Model selection strategy For each spin of the protein, one of five models (Model_1 to Model_5) could be selected to fit three experimental data (R_1, R_2, and NOE) for that spin. The model selection strategy is based on Monte Carlo numerical simulations [109] that estimate the goodness-of-fit between the dynamical models and the experimental data. The results from the *Modelfree* output file are judged by either Γ_i at 90th percentile (the X percentile corresponds to the (1-X/100) critical value, for example, 90th percentile corresponds to 0.1 critical value) or F_i at 80th percentile. The definitions of Γ (or, SSE) and F are given by Eqs. (7) and (8), respectively. **Fig. 6.1** shows a flowchart of the model selection strategy [108]. First we test whether Model_1 (00100) represents our experimental data sufficiently well: Is $\Gamma_i < \Gamma_i(0.1)$? Since there is one parameter, S_s^2, in Model_1, the degrees of freedom are equal to two (three experimental

parameters, R_1, R_2, and NOE, need be fit) and the theoretical value of $\Gamma_i(0.1)$ is equal to 4.61 [110]. If this condition is true (that is, $\Gamma_i < 4.61$), then we accept Model_1 for this residue without further testing if any of the other models are "even better". If a residue is not well fit by Model_1, we check whether $\Gamma_i < \Gamma_i(0.1)$ for Model_2 (00110) and Model_3 (00101). With two fitting parameters in these cases, the degrees of freedom are one and $\Gamma_i(0.1)$ is equal to 2.71. Also, an F-statistics value needs to be examined to see how Model_2 or Model_3 give an improved result compared with Model_1. If $F_i > F_i(0.2)$, then the answer is affirmative. The values of $\Gamma(0.1)$ and F(0.2) can be obtained from standard statistical tables [110]. With $p_1 = 2$ (Model_1) and $p_2 = 1$ (Model_2 or Model_3), the theoretical value of F(0.2) is equal to 9.5. For the residues fit by neither Model_2 nor Model_3, Γ_i is checked again. If Γ_i is less than 20, Model_1 is used to fit those residues. If not, model selection proceeds to Model_4 (00111) and Model_5 (01110). Because the numbers of degrees of freedom are zero (three parameters fit three experimental data), the theoretical value of Γ is equal to zero at any percentile. The selection of Model_4 and Model_5 is clear from the flowchart. After we have determined which model best fits each residue, we can carry out one single *Modelfree* run that simultaneously fits the global τ_m and the appropriate model-free parameters for each residue. It is also possible to repeat the model selection using the newly generated τ_m until the convergence of either the τ_m value or the choice of models is reached.

6.3 ^{15}N R_1, R_2, and NOE Measurements on Apo- and Holo-LFABP

6.3.1 Sample preparation

^{15}N-labeled apo form of LFABP in pH 6.0 phosphate buffer was provided by Professor Judith Storch's research group at Rutgers University. The holo form of the protein is a complex of ^{15}N-LFABP with eight equivalents of unlabeled oleate in pH 7.0 phosphate buffer (Section 4.2.1). The concentrations of apo- and holo- LFABP are 0.40 mM and 0.20 mM, respectively.

6.3.2 Experimental

^{15}N R_1, R_2, and ^{1}H-^{15}N NOE spectra were recorded at 30 °C on a four-channel Varian INOVA-600 spectrometer (Varian NMR instruments, Palo Alto, CA) equipped with an indirect-detection triple resonance probe and z-axis pulsed field gradients. The pulse sequences used to record R_1, R_2, and NOE data were obtained from Lewis Kay's group at University of Toronto, Canada[111]. These experiments employ minimal saturation of the water resonance and thus avoid any potential complications from hydrogen exchange. Basically, 2D ^{1}H-^{15}N HSQC spectra are generated with different amide ^{15}N signal intensities.

Backbone amide ^{15}N R_1 values for apo- and holo-LFABP were measured from eleven and twelve spectra with the following recovery times: T(apo) = 11.1, 44.4, 88.8, 144.3, 222.0(×2), 321.9, 432.9, 610.5, 854.7, and 1110 ms; T(holo) = 11.1(×2), 44.4, 88.8, 144.3, 222.0, 321.9, 432.9, 610.5(×2), 854.7, and 1110 ms (duplicate acquisitions are indicated by the ×2 notation). Amide ^{15}N R_2 values were obtained similarly: for apo-LFABP, eight spectra were recorded with spin echo delay times T = 14.4, 28.8, 43.2, 57.6, 72.0, 86.4, 100.8, and 129.6 ms; for holo-LFABP, ten spectra were recorded with

spin echo delay times T = 14.4(×2), 43.2, 57.6, 72.0, 86.4, 100.8, 129.6(×2), and 144.0 ms. For R_1 and R_2 measurements, a recycle delay of 1 s was used between transients.

Steady-state ^1H-^{15}N NOE values were obtained by recording spectra with (NOE experiment) and without (NONOE experiment) the use of ^1H saturation during the delay time between successive transients. In the NONOE experiment, a relaxation delay of 5 s was employed between transients, while the NOE experiment employed a 2 s delay plus 3 s of proton presaturation achieved with the use of 120° ^1H pulses applied every 5 ms [112].

For apo-LFABP, the ^{15}N relaxation measurements were performed using a total of 32 transients per t_1 experiment; 320 × 1024 complex data points were acquired in the t_1 × t_2 dimensions. For holo-LFABP, a total of 64 transients were used and 256 × 1024 complex points were acquired. In all experiments, the ^1H carrier frequency was set on the resonance of water and the ^{15}N carrier was set at 120.54 ppm.

6.3.3 Data processing

Relaxation spectra were processed with NMRPipe and converted to NMRView (see Chapter 2 for the details of the programs NMRPipe and NMRView). Peak intensities were measured from the NMR spectra using a custom written tcl script in NMRView. The dependence of amide NH peak intensity on delay time was generated for each residue. Reliable quantitation of peak intensities was possible for 105 of the expected 109 ^{15}N backbone resonances in apo-LFABP (127 residues minus the N-terminal Met, two Pro, and 15 unassigned residues) and 112 of the expected 123 ^{15}N backbone resonances in holo-LFABP (one residue was unassigned). Four resolved

signals for apo (Lys^{47}, Glu^{72}, Val^{83}, and Met^{91}) and three signals for holo (Ser^{56}, Thr^{75}, and Thr^{110}) were too weak to quantify accurately, and the remaining resonances of the holo-protein were heavily overlapped.

R_1 and R_2 values were determined by fitting the measured peak intensities to a two-parameter function of the form

$$I(t) = I(0) \exp(-R_{1,2} * t) \quad (9),$$

where I(t) is the intensity after a delay of time t and I(0) is the intensity at time t = 0. Optimum values for the parameters were determined by the Levenberg-Marquardt non-linear least squares fitting method, using a program, ***jacknife***, written by Arthur Palmer at Columbia University. The input file for *jackknife* included intensity, time, and intensity uncertainty. The uncertainty, σ_I, is the standard deviation of the experimental intensity differences measured from duplicate time points. The output from *jacknife* simulation gave several fitted parameters: I(0), R_1, R_2, and the χ^2 goodness-of-fit parameter. Here,

$$\chi^2 = \Sigma [I_{cal}(t) - I_{exp}(t)]^2 / \sigma_I^2 \quad (10),$$

where $I_{exp}(t)$ are the experimental intensities and $I_{cal}(t)$ are the intensities calculated from the fitted parameters. The summation was performed over the number of time points recorded in each experiment.

The quality of R_1 and R_2 data is judged by comparing the calculated χ^2 value (Eq. 10) to tabulated values of χ^2 at 25th, 50th, and 75th percentiles for the appropriate degrees of freedom. For example, a total of 12 spectra were obtained for the R_1 measurements on holo-LFABP, which gave 10 degrees of freedom because two parameters (I(0), R_1) were fit. For the 116 analyzed residues, χ^2 values from *jacknife* output were sorted by an ascending model. The χ^2 values at lines 28, 56, and 84 then

corresponded to 25th, 50th, and 75th percentiles, respectively. The theoretical χ^2 values with 10 degrees of freedom at those three typical percentiles are 6.74, 9.34, and 12.55, which are larger than the experimental χ^2 values of 5.06, 7.81, and 10.29. Therefore, the quality of R_1 experimental data is judged sufficient for further dynamics calculations. The χ^2 distribution for R_1 with 10 degrees of freedom is displayed in **Fig. 6.2.**

The steady-state NOE values were determined from the ratios of the intensities of the peaks (peak height) with and without proton saturation. That is,

$$NOE = I_{NOE} / I_{NONOE} \quad (11),$$

where I_{NOE} and I_{NONOE} are the measured intensities of a resonance in the presence and absence of proton saturation, respectively. The standard deviation of the NOE value, σNOE, was determined on the basis of measured background noise levels using the following relationship:

$$\sigma NOE / NOE = \text{sqrt}\,[(\sigma I_{NOE} / I_{NOE})^2 + (\sigma I_{NONOE} / I_{NONOE})^2] \quad (12),$$

in which σI_{NOE} and σI_{NONOE} are measured background noise levels obtained from NMRPipe.

6.3.4 Results

The curve fitting of R_1 and R_2 on Gly^{32} and Asn^{61} residues of both apo- and holo-LFABP is displayed in **Fig. 6.3.** The addition of oleate to the protein makes the amide signal of Gly^{32} decay more slowly in the R_1 experiment, but Asn^{61} is almost unchanged.

The ^{15}N R_1, R_2, and NOE values along the protein sequence are plotted in **Fig. 6.4** for both apo- and holo-LFABP. The average values for the R_1, R_2, and NOE relaxation parameters were $2.06 \pm 0.13\ s^{-1}$, $10.41 \pm 0.58\ s^{-1}$, and 0.80 ± 0.10, respectively, for apo-

LFABP and 1.77 ± 0.02 s^{-1}, 9.95 ± 0.24 s^{-1}, and 0.77 ± 0.05, respectively, for holo-LFABP.

6.4 Running *Modelfree*4.0 --- Calculation of τ_m, S^2, τ_e, and R_{ex}

6.4.1 Quadric diffusion program

A quadric diffusion model[113,114], using a program developed by Prof. Arthur Palmer at Columbia University, was used to calculate the diffusion tensor from ^{15}N or ^{13}C relaxation data using the local diffusion approximation. The local rotational correlation time is obtained from a trimmed mean value of the experimental R_2/R_1 data. With this program, the distinction between isotropic and axial diffusion tensors is based on the F-statistic value at 95% confidence limits (that is, at a critical value of 0.05) as follows. For isotropic diffusion, τ_m is a parameter to be fit in the calculation. For axial diffusion, there are four parameters, τ_m, D_{ratio}, theta, and phi that need be fitted. D_{ratio} is the ratio of the parallel component of the diffusion tensor ($D_{||}$) to the perpendicular component ($D_{\perp}$). Theta and phi are the polar angles for the symmetry axis of the diffusion tensor in the coordinate frame of the PDB (Protein Data Base) file. Thus, the degrees of freedom for isotropic diffusion are N-1 and for axial are N-4, where N is the number of residues involved in the calculation. In our case, 105 residues from apo-LFABP and 112 residues from holo-LFABP are involved in the calculation. From Eq. (8), p_1 (isotropic) = 104 for apo and 111 for holo; p_2 (axial) = 101 for apo and 108 for holo; and $p_1 - p_2 = 3$. Thus, F(0.05) at degree of freedom 104/3 or 111/3 will be 2.68 based on standard texts[110]. If the calculated F(0.05) is larger than 2.68, an axial diffusion tensor is preferred for the protein. On the other hand, if the calculated F(0.05) is smaller than 2.68, an isotropic

diffusion tensor is preferred for the protein. In our case, apo-LFABP was fit better with an axial model (F = 7.8) and holo-LFABP showed preference for an isotropic (F = 2.2) diffusion tensors.

6.4.2 Strategy for *Modelfree* calculation

The procedure for the dynamic calculation of τ_m, S^2, τ_e, and R_{ex} is described in **Fig. 6.5**. In the absence of more definitive information, the simplest theoretical approach to calculate the isotropic rotational correlation time is from Stokes' law [93]:

$$\tau_m = 4\pi\eta_w r_H^3 / (3k_B T) \qquad (13)$$

in which η_w is the viscosity of the solvent, r_H is the effective hydrodynamic radius of the protein, k_B is Boltzmann's constant, and T is the absolute temperature. The hydrodynamic radius is roughly estimated from the molecular mass of the protein (M_r) by assuming that the specific volume of the protein is $\bar{V}$ = 0.73 cm^3/g, a value found for ubiquitin [33]:

$$r_H = [3\ \bar{V}\ M_r / (4\pi\ N_A)]^{1/3} + r_w \qquad (14).$$

The hydration layer that surrounds the protein, r_w, is about 1.6 to 3.2 Å. With the information for the protein ubiquitin: M_r = 8,565 Da, r_H = 16.5 Å, and τ_m = 3.8 ns at 300 K[93], a τ_m value for LFABP (M_r = 14,000 Da) at 303 K is 5.9 ns when calculated by combining Eqs. (13) and (14). This value was used as an initial guess in the *Modelfree* calculation for LFABP.

With τ_m (5.9 ns) estimated for LFABP, Model_1 (00100) was selected to search for the real initial τ_m. With the τ_m values obtained from initial *Modelfree* run (6.58 ns for holo and 6.48 ns for apo), the quadric diffusion program was run to determine the

diffusion tensor for the protein. Since we obtained F-statistic values of 2.2 for holo and 7.8 for apo, respectively, comparing the theoretical F(0.05) value of 2.68 showed that an isotropic diffusion model was suitable for holo and an axial diffusion model was suitable for apo.

Using the new values of τ_m (isotropic) and τ_m, D_{ratio}, theta, and phi (axial) obtained from the output file of the quadric diffusion run, we performed model selection (from Model_1 to Model_5) based on **Fig. 6.1**. The remainder of the flowchart in **Fig. 6.5** was followed straightforwardly.

6.4.3 Results

For backbone amide nitrogen spins, optimized values of the *Modelfree* parameters for holo-LFABP are given in **Table 6.1** (Results for apo-LFABP appear seperately in Section 6.5). The optimized value of τ_m is 6.35 ns for holo-LFABP. The generalized order parameters (S^2), the effective correlation time (τ_e), and the chemical exchange terms (R_{ex}) for the backbone nuclear spins of holo-LFABP are plotted as a function of sequence in **Fig. 6.6**. Order parameters and chemical exchange terms for holo-LFABP are mapped onto the three-dimensional structure using an X-ray model (oleate-bound holo-LFABP)[25] and presented in **Fig. 6.7**. The results are also sorted according to which model gave the best fit in **Table 6.2**. Finally, mean values of the generalized order parameters of the backbone ^{15}N nuclear spins for each secondary structural element are given in **Table 6.3**.

6.5 Discussion

To elucidate protein-ligand binding site(s), functional properties, and conformational exchange, it is essential to have dynamic information for both apo and holo forms of the protein. Unfortunately, at the time of this writing, the dynamics results for the apo-LFABP are incomplete. After running *Modelfree*, there were 30 residues with generalized order parameters $S^2 = 1.00$, an unreasonable result because the range for S^2 is from 0 to 1 and it is unlikely that so many residues are fully ordered. "S^2=1" represents the most ordered state and we know independently that apo-LFABP is much less ordered than holo. The cause of this unexpected result is the quality of the original R_1, R_2, and NOE data. As shown in **Fig. 6.4**, 23 residues (F3, Q10, K20, G32, G37, I41, T51, G55, S56, I59, E62, C69, T75, G76, V83, T93, V101, D107, T108, N111, T114, D117, and K121) have anomalously large error bars on values of R_1 ($\delta R_1 > 10\%$), and most of them yield "S^2=1" after *Modelfree* calculations. Many of these residues exhibit very weak intensities in the ^1H-^{15}N HSQC spectra, and some of their resonances are poorly resolved. Thus, even the significant number of low order parameters obtained for apo-LFABP (data not shown) is suspect, since that result may be biased by the 23 poorly behaved residues.

In an alternative approach, the R_1 data were reprocessed using a Lorentz-to-Gauss window function plus line broadening (GMB) instead of the sine-bell window function (SP). With the GMB window function, the exponential term is specified as a Lorentzian line sharpening in Hz (gb), and the Gaussian term is specified as a Gaussian line broadening in Hz (lb). By adjusting gb and lb values, the cross-peaks in the HSQC spectrum were optimized to become as sharp (and well resolved) as possible. Nevertheless, the R_1 curves remained poorly fit for those 23 apo-LFABP peaks with

weak intensities. In the absence of additional ^{15}N relaxation experiments on a new apo-LFABP sample, only a qualitative comparison of backbone dynamics is possible for apo and holo forms of the protein.

Examining ^{15}N R_1, R_2, and NOE data for apo- and holo-LFABP (**Fig. 6.4**), it is clear that upon addition of ligand to the protein, the R_1 and R_2 values of certain residues were dramatically decreased and NOE values became more uniform, suggesting that ligand addition locks the protein into a less flexible conformation. For example, residues Q8, V9, I29, Q30, G32, T51, and K125 had smaller R_1 and R_2 values in the holo-protein; those residues also exhibited larger chemical shift changes between apo- and holo-LFABP ($\Delta\delta$ > 100 Hz, see Chapter 4). Viewed in conjunction with H/D exchange results presented in Chapter 3, residues G32, I41, and T93 were found to have smaller R_1 and R_2 values and also became less solvent accessible. Since we do not have a satisfactory *Modelfree* dynamic analysis for apo-LFABP, more rigorous protein-ligand interaction properties could not be established. The following discussion is based on holo-LFABP only.

The high generalized order parameters throughout the protein sequence (**Table 6.1** and **Fig. 6.7**) suggest that holo-LFABP adopts a relatively rigid conformation compared with palmitate-bound holo-IFABP and HFABP. It should be pointed out that there are eight equivalents of oleate in the protein sample that we used to study ^{15}N dynamics. Five residues had relatively low order parameters (S^2 < 0.75): F3, K36, E68, G87, and D88. They are all located in loop regions and far away from the two bound oleates, so this result is reasonable. The S^2 value for K20 (located at the end of αI) was 1.00, which is unexpected. It should be noted, however, that K20 was the only residue

that had a negative ^{1}H-^{15}N NOE value in the apo form of the protein. Since a negative NOE indicates that the residue is either extremely flexible or that the peak originates from a small fragment, two interpretations are possible for the K20 result. NOE results attributed to K20 may actually originate from an unidentified protein fragment, because the amide proton of K20 resonates at 8.27 ppm, a region where extraneous signals were observed in apo-LFABP spectra. Nevertheless, this hypothesis fails to explain why the signal had S^2=1 in the holo-protein. Secondly, the negative NOE could come from K20. Since K20 is located at the end of the first α-helix (not in the "portal" region), it is plausible that the addition of eight equivalents of oleate makes K20 unusually ordered.

The residues requiring conformational exchange terms generally coincided with those having low order parameters. In the case of holo-LFABP, the correlation between low order parameters and significant R_{ex} contributions was not so strong (**Figs 6.6** and **6.7**). However, the R_{ex} results themselves were quite interesting. About half of the residues that were investigated have R_{ex} terms (Model_3 and Model_4, see **Table 6.2**). Large R_{ex} terms are found mainly in the regions of αII-βB, βC-βD, βE-βF, and βG-βH loops (**Fig. 6.6**), although the N-terminus, βA-αI loop and βG-strand also exhibit substantial R_{ex} terms. The αII-βB, βC-βD, and βE-βF are well known "portal" regions for iLBPs in general. The βG-βH loop and perhaps part of the βG and βH strands, which are two residues each shorter than in other iLBPs, have been speculated to comprise a second "portal" region that is unique to LFABP [25]. The present results suggest that even at a saturating oleate concentration (8 eq. per LFABP), these portal regions exhibit substantial exchange behavior. This observation lends strong support to the lignad-exchange hypothesis, i.e., the two oleates in the cavity exchange with those in the

solution (see Chapter 7). Because the exchange may proceed through the portal regions, the corresponding residues should therefore display large R_{ex} terms.

Figure 6.1 Flowchart of the model selection strategy[108]. The details are provided in the text.

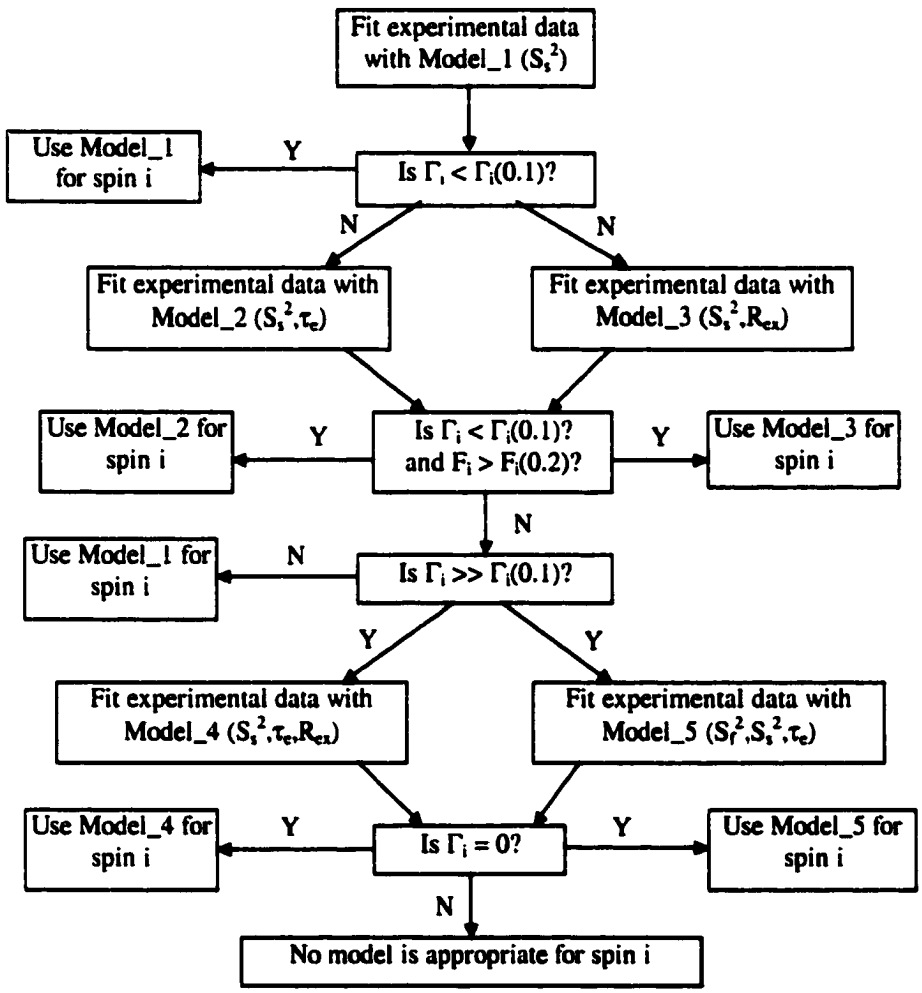

Figure 6.1

Figure 6.2 Statistic histogram of chi-squared distribution (χ^2) of R_I values in holo-LFABP. The R_I data were obtained by *jacknife* simulation. Details are described in the text.

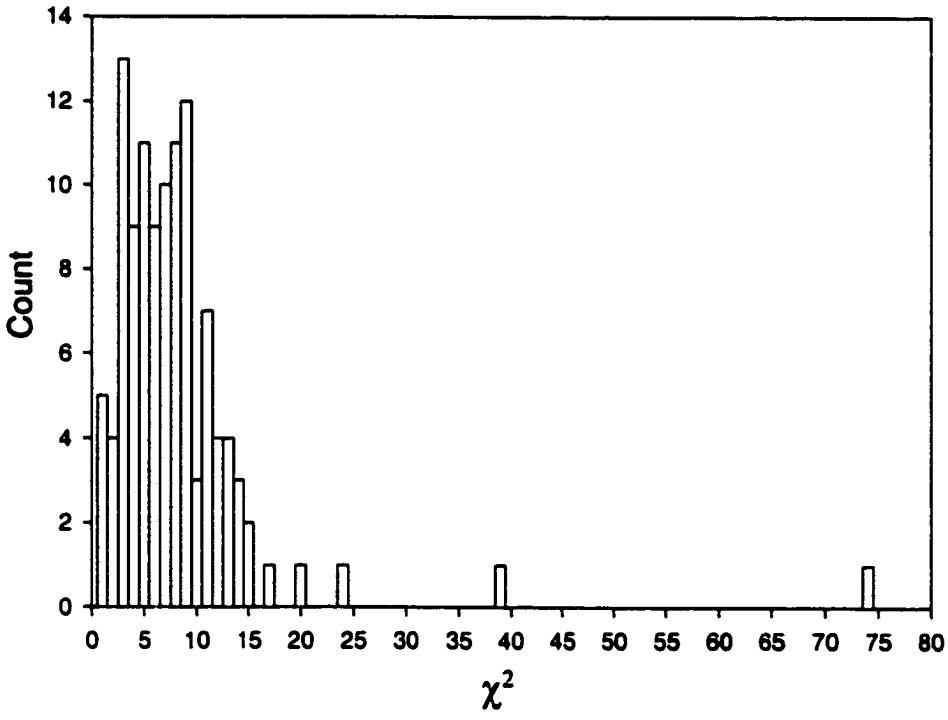

Figure 6.2

Figure 6.3 *Jacknife* R_1 (top panel) and R_2 (bottom panel) curve fitting for residue N61 and G32 in apo-LFABP (open) and holo-LFABP (solid).

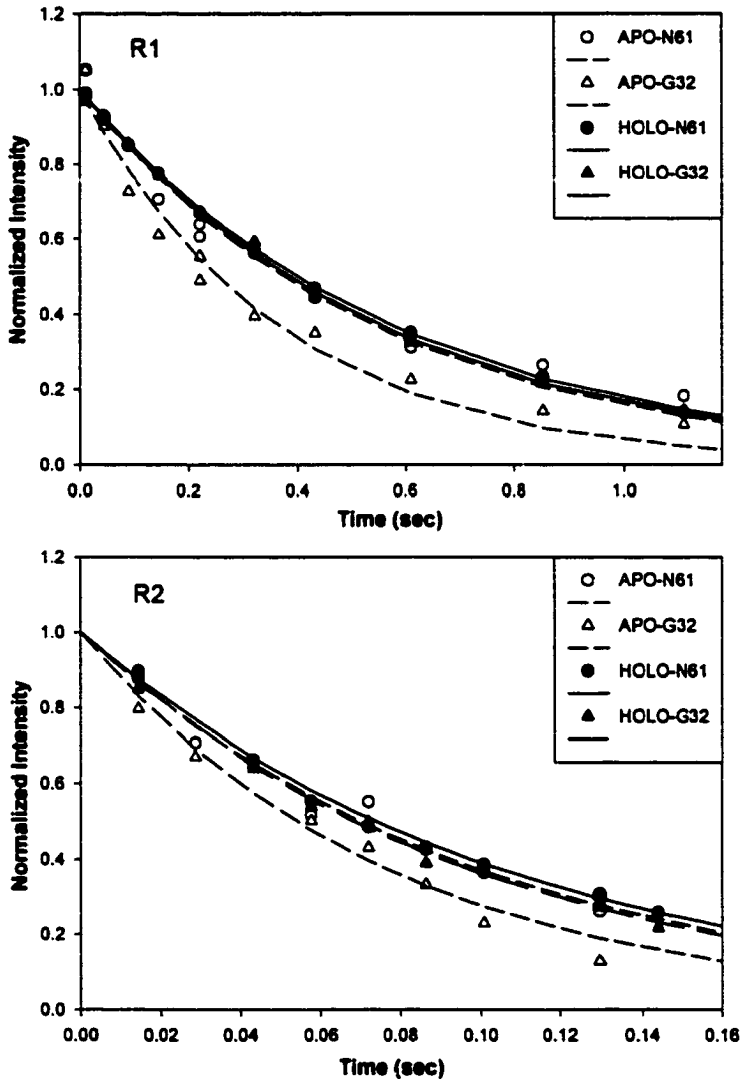

Figure 6.3

Figure 6.4 ^{15}N R_1, R_2, and NOE data for both apo-LFABP (filled circles) and holo-LFABP (open circles). The mean values of R_1 are 2.06 ± 0.13 s^{-1} for apo and 1.77 ± 0.02 s^{-1} for holo. R_2 averages are 10.41 ± 0.58 s^{-1} for apo and 9.95 ± 0.10 s^{-1} for holo. Mean NOEs are 0.80 ± 0.10 for apo and 0.77 ± 0.05 for holo. Mean values excluding poorly behaved residues in the apo protein are tabulated as R_1', R_2', and NOE'. The secondary structure shown is derived from sequential assignments of the protein and chemical shift indices (Chapter 2 for apo and Chapter 5 for holo).

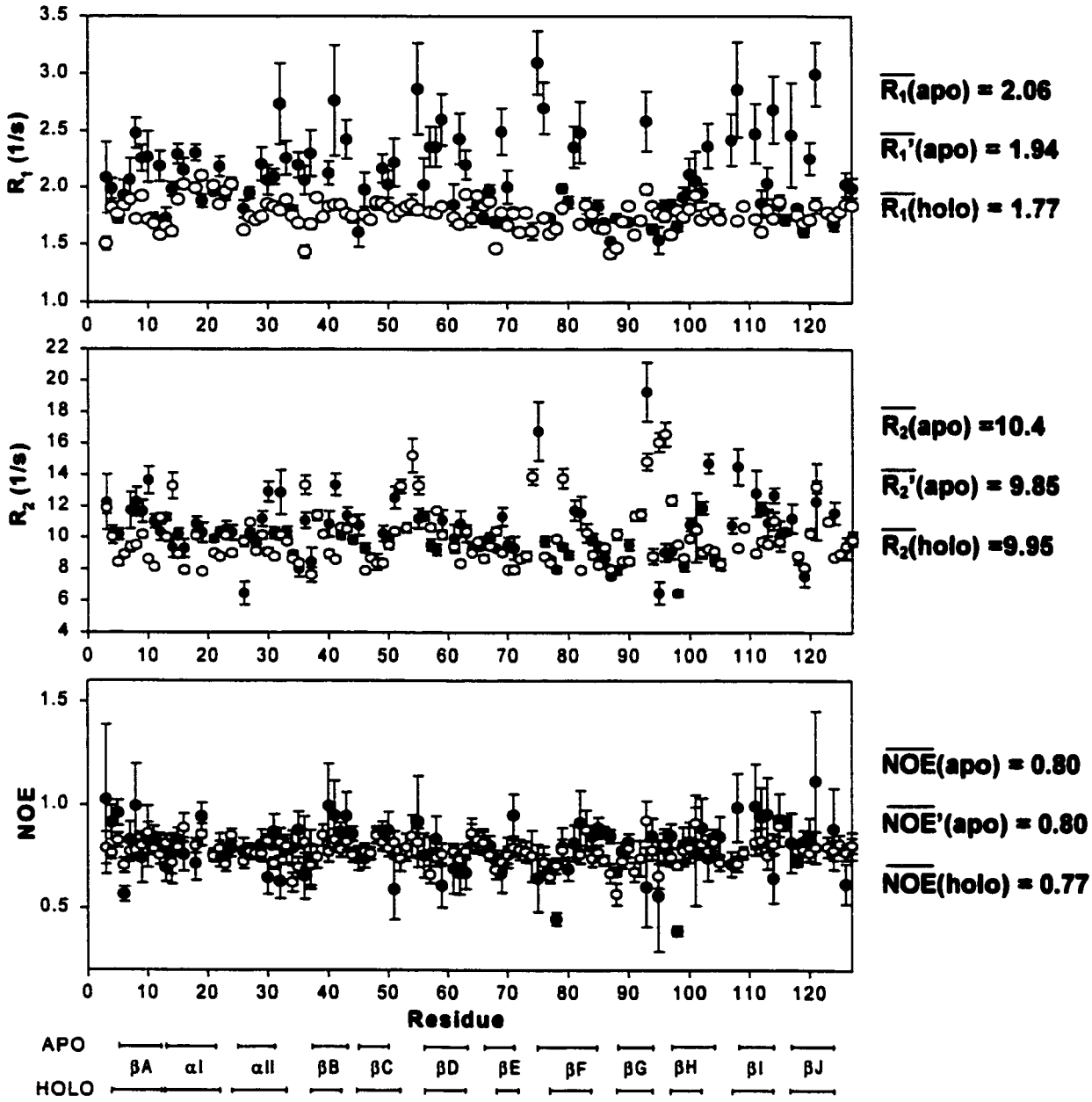

Figure 6.4

Figure 6.5 Flowchart of running *Modelfree* for the calculation of τ_m, S^2, τ_e, and R_{ex}. Additional details are described in the text.

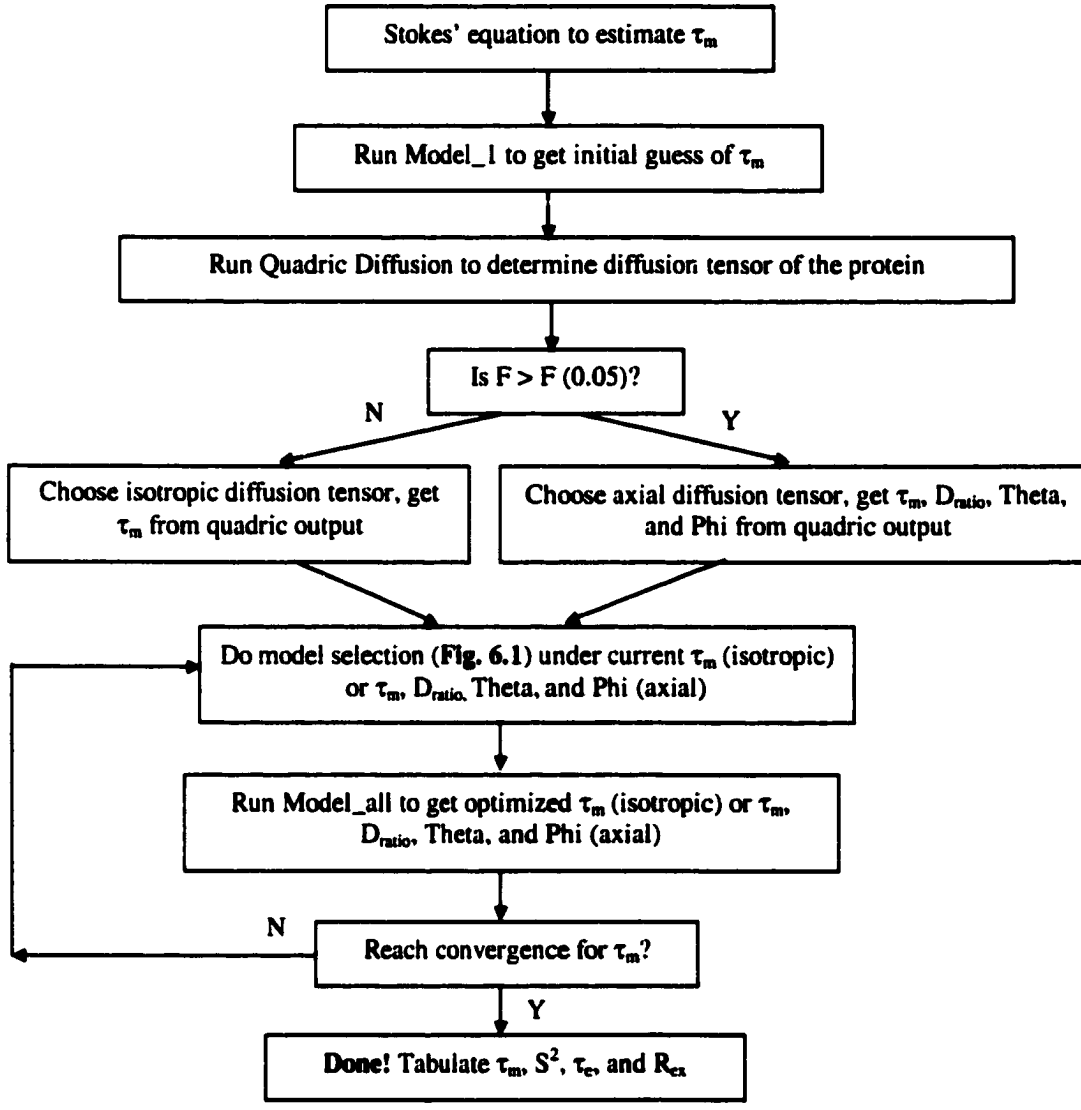

Figure 6.5

Figure 6.6 Results of dynamic calculations for holo-LFABP. The secondary structure derived from sequential assignments by CSI is shown below the corresponding amino acid residues. The τ_e value for residues Ile41 is 6300 ps (noted as *).

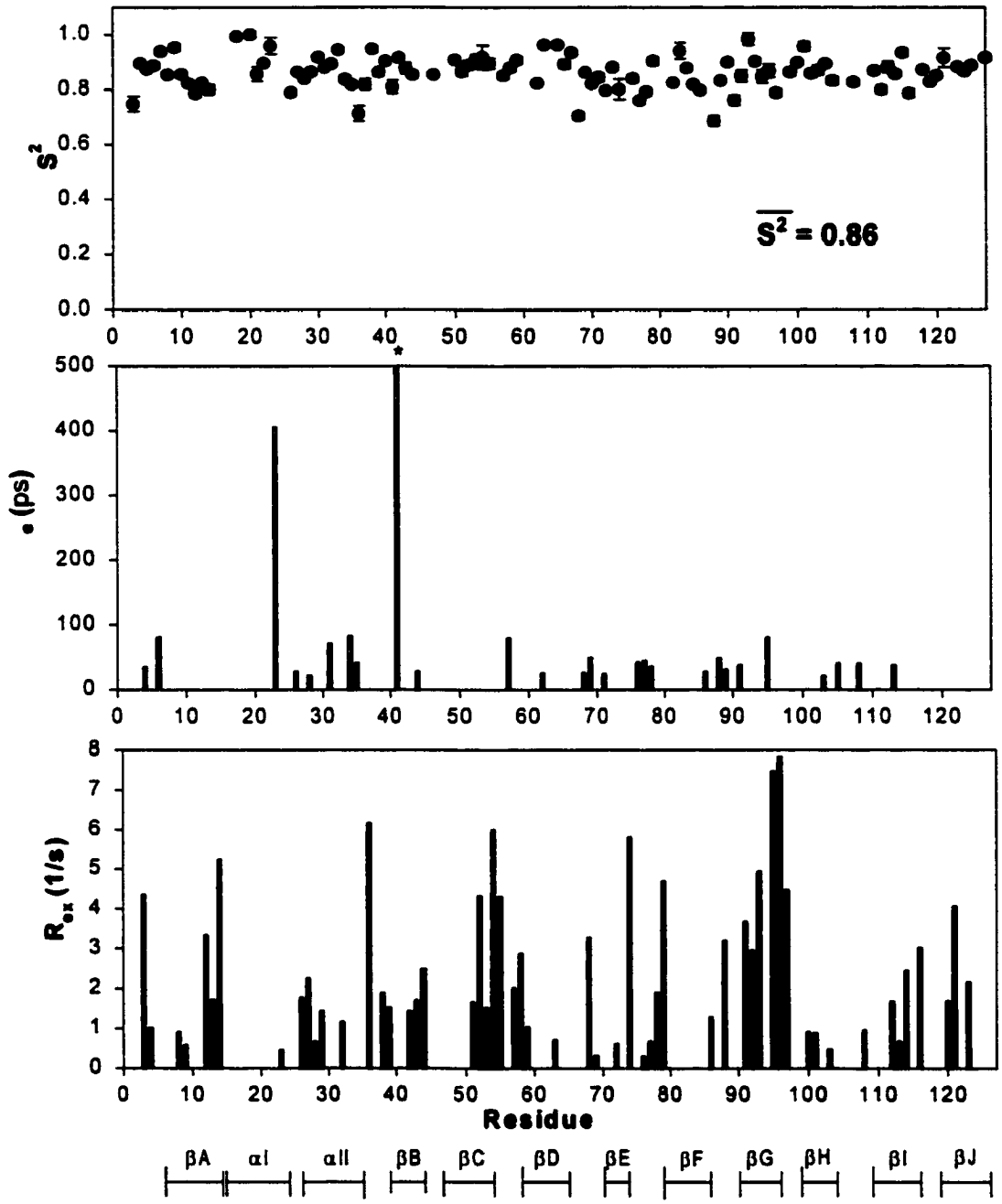

Figure 6.6

Figure 6.7 Backbone chain traces coded by generalized order parameter (S^2) and chemical exchange term (R_{ex}) for holo-LFABP displayed by X-ray model. The code scheme for S^2: "1", $S^2 \geq 0.90$; "2", $S^2 = 0.75\text{-}0.90$; "3", $S^2 = 0.60\text{-}0.75$; and "4", $S^2 \leq 0.60$. The code scheme for R_{ex}: "1", $R_{ex} = 0$; "2", $R_{ex} = 0\text{-}1.5$; "3", $R_{ex} = 1.5\text{-}3.5$; and "4", $R_{ex} \geq 3.5$. Residues for which no data was available are labeled as "5".

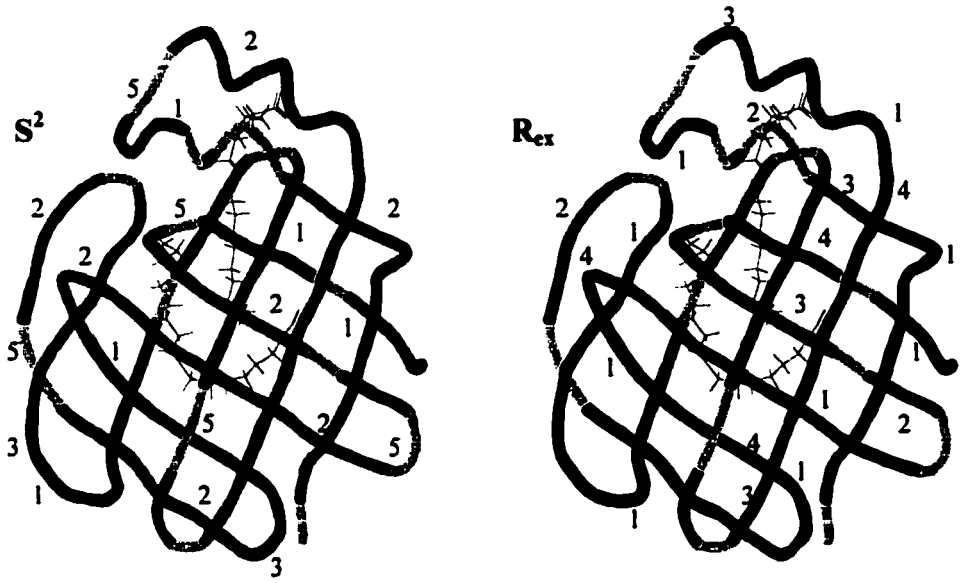

Figure 6.7

Table 6.1 Backbone dynamic parameters for holo-LFABP at 30 °C.

Table 6.1

HOLO-LFABP (τ_m = 6.35 ns)							
Residue	2°[a]	Model[b]	$S^2=S_s^2S_f^2$	S_f^2	τ_e (ps)	R_{ex} (1/s)	Γ_i^c
[d] Met[1]							
[d] Asn[2]							
Phe[3]		3	0.748±0.027			4.36±0.46	0.10
Ser[4]		4	0.895±0.011		35±20	1.01±0.14	0.00
Gly[5]	βA	1	0.873±0.006				3.44
Lys[6]	βA	2	0.887±0.011		81±25		0.18
Tyr[7]	βA	1	0.939±0.009				0.80
Gln[8]	βA	3	0.854±0.009			0.91±0.18	0.57
Val[9]	βA	3	0.953±0.011			0.58±0.21	0.05
Gln[10]	βA	1	0.855±0.007				0.88
Ser[11]	βA	1	0.822±0.007				4.70
Gln[12]	βA	3	0.786±0.011			3.33±0.29	1.58
Glu[13]	βA	3	0.824±0.007			1.71±0.18	0.00
Asn[14]	αI	3	0.800±0.016			5.24±0.84	0.86
[e] Phe[15]	αI						
[e] Glu[16]	αI						
[d] Pro[17]	αI						
Phe[18]	αI	1	0.994±0.008				1.18
[e] Met[19]	αI						
Lys[20]	αI	1	1.000±0.009				4.13
Ala[21]	αI	5	0.856±0.025	0.969±0.016	1844±598		0.00
Met[22]	αI	1	0.896±0.011				4.51
Gly[23]	αI	4	0.959±0.030		405±628	0.46±0.25	2.03
[e] Leu[24]							
[d] Pro[25]	αII						
Glu[26]	αII	4	0.789±0.009		28±10	1.77±0.33	0.00
Asp[27]	αII	3	0.863±0.010			2.27±0.17	1.32
Leu[28]	αII	4	0.839±0.009		22±11	0.67±0.20	0.00
Ile[29]	αII	3	0.864±0.008			1.44±0.25	2.19
Gln[30]	αII	1	0.917±0.009				0.49
Lys[31]	αII	2	0.880±0.007		71±16		1.39
Gly[32]	αII	3	0.893±0.010			1.16±0.32	0.00
Lys[33]	αII	1	0.944±0.008				3.42
Asp[34]	αII	2	0.837±0.012		83±21		1.03
Ile[35]		2	0.818±0.011		42±17		0.33
Lys[36]		3	0.713±0.027			6.17±0.65	0.00
Gly[37]		1	0.819±0.018				3.38
Val[38]	βB	3	0.947±0.009			1.89±0.32	1.51
Ser[39]	βB	3	0.863±0.012			1.52±0.22	0.58
Glu[40]	βB	1	0.904±0.009				1.25
Ile[41]	βB	5	0.810±0.023	0.885±0.008	6300±6253		0.21
[f] Val[42]	βB	3	0.915±0.010			1.44±0.17	0.65
His[43]	βB	3	0.877±0.019			1.71±0.27	0.04
Glu[44]		4	0.854±0.010		28±16	2.48±0.21	0.00
[f] Gly[45]							
[f] Lys[46]	βC	5	0.751±0.023	0.839±0.018	2449±1702		0.00

Table 6.1 — *Continued*

HOLO-LFABP (τ_m = 6.35 ns)							
Residue	2°[a]	Model[b]	$S^2=S_s^2S_f^2$	S_f^2	τ_e (ps)	R_{ex} (1/s)	Γ_i^c
Lys^{47}	βC	1	0.854±0.005				3.41
[e] Val^{48}	βC						
[e] Lys^{49}	βC						
Leu^{50}	βC	1	0.908±0.009				2.71
Thr^{51}	βC	3	0.866±0.015			1.66±0.25	0.00
Ile^{52}	βC	3	0.889±0.015			4.32±0.44	1.52
Thr^{53}	βC	3	0.906±0.021			1.51±0.36	0.09
Tyr^{54}		3	0.917±0.043			6.00±1.15	0.11
Gly^{55}		3	0.895±0.018			4.30±0.59	0.00
[g] Ser^{56}							
Lys^{57}	βD	4	0.851±0.012		80±20	2.01±0.25	0.00
Val^{58}	βD	3	0.879±0.013			2.87±0.17	2.63
Ile^{59}	βD	3	0.907±0.011			1.03±0.28	1.00
[f] His^{60}	βD						
Asn^{61}	βD	4	0.854±0.010		19±13	0.81±0.24	0.00
Glu^{62}	βD	2	0.823±0.006		25±11		0.62
Phe^{63}	βD	3	0.962±0.010			0.71±0.24	1.20
[f] Thr^{64}	βD	1	0.865±0.006				6.74
Leu^{65}		1	0.962±0.009				0.38
Gly^{66}		1	0.892±0.014				3.11
Glu^{67}		1	0.935±0.004				5.46
Glu^{68}		4	0.705±0.012		26±8	3.27±0.29	0.00
Cys^{69}	βE	4	0.862±0.011		49±19	0.31±0.19	0.00
Glu^{70}	βE	1	0.821±0.005				10.23
Leu^{71}	βE	2	0.845±0.013		24±18		9.90
Glu^{72}	βE	3	0.797±0.006			0.61±0.17	0.41
Thr^{73}	βE	1	0.881±0.011				0.68
Met^{74}		3	0.801±0.036			5.82±0.61	0.25
[g] Thr^{75}							
Gly^{76}		4	0.840±0.013		43±17	0.30±0.23	0.00
Glu^{77}		4	0.760±0.008		45±8	0.68±0.15	0.00
Lys^{78}	βF	4	0.792±0.012		35±11	1.90±0.14	0.00
Val^{79}	βF	3	0.904±0.014			4.70±0.64	0.37
[f] Lys^{80}	βF						
[f] Ala^{81}	βF						
Val^{82}	βF	1	0.825±0.006				9.52
Val^{83}	βF	1	0.941±0.029				3.03
Lys^{84}	βF	1	0.878±0.011				3.60
Met^{85}	βF	1	0.819±0.009				1.72
[f] Glu^{86}		4	0.798±0.007		28±7	1.29±0.19	0.00
[f] Gly^{87}		4	0.681±0.019		27±8	1.08±0.24	0.00
Asp^{88}		4	0.688±0.018		49±10	3.20±0.36	0.00
Asn^{89}	βG	2	0.833±0.007		31±13		1.02
Lys^{90}	βG	1	0.899±0.009				8.28
Met^{91}	βG	4	0.761±0.017		38±12	3.67±0.33	0.00
Val^{92}	βG	3	0.849±0.020			2.95±0.40	0.69

Table 6.1 — *Continued*

HOLO-LFABP (τ_m = 6.35 ns)							
Residue	2°[a]	Model[b]	$S^2=S_s^2S_f^2$	S_f^2	τ_e (ps)	R_{ex} (1/s)	Γ_i^c
Thr^{93}	βG	3	0.984±0.021			4.94±0.57	1.31
Thr^{94}	βG	1	0.903±0.010				2.24
Phe^{95}	βG	4	0.847±0.023		81±31	7.48±0.64	0.00
Lys^{96}		3	0.868±0.023			7.84±0.79	0.01
Gly^{97}		3	0.788±0.013			4.47±0.34	2.53
[f] Ile^{98}	βH	4	0.870±0.012		63±12	0.74±0.19	0.00
Lys^{99}	βH	1	0.863±0.011				0.54
Ser^{100}	βH	3	0.898±0.008			0.91±0.19	0.21
Val^{101}	βH	3	0.957±0.015			0.88±0.20	1.53
Thr^{102}	βH	1	0.858±0.012				1.73
Glu^{103}	βH	4	0.871±0.016		22±23	0.48±0.17	0.00
Phe^{104}		1	0.894±0.006				0.85
Asn^{105}		2	0.832±0.013		41±15		0.06
[f] Gly^{106}							
[f] Asp^{107}							
Thr^{108}	βI	4	0.827±0.011		41±14	0.96±0.13	0.00
[f] Ile^{109}	βI	3	0.908±0.008			1.50±0.16	2.53
[g] Thr^{110}	βI						
Asn^{111}	βI	1	0.869±0.012				2.70
Thr^{112}	βI	3	0.800±0.013			1.68±0.31	0.04
Met^{113}	βI	4	0.882±0.019		38±38	0.67±0.26	0.00
Thr^{114}	βI	3	0.857±0.008			2.44±0.57	0.01
Leu^{115}	βI	1	0.935±0.012				4.25
Gly^{116}		3	0.787±0.014			3.01±0.25	2.51
[f] Asp^{117}							
Ile^{118}	βJ	1	0.872±0.004				2.53
Val^{119}	βJ	1	0.828±0.007				4.83
Tyr^{120}	βJ	3	0.852±0.005			1.69±0.19	1.38
Lys^{121}	βJ	3	0.915±0.034			4.06±0.50	0.06
[f] Arg^{122}	βJ						
Val^{123}	βJ	3	0.882±0.006			2.17±0.19	0.12
Ser^{124}	βJ	1	0.867±0.007				0.59
Lys^{125}	βJ	1	0.889±0.008				0.02
[f] Arg^{126}		1	0.930±0.009				2.73
Ile^{127}		1	0.916±0.008				3.49

[a] Secondary structure (2°) was derived from sequential assignments and chemical shift indices[66].

[b] Dynamic models employed to fit the relaxation data for each nuclear spin, as described in the text (Model_1 to Model_5).

[c] The definition of Γ_i appears in Eq. (7).

[d] Residues with either missing amide ^1H and ^{15}N assignments or Proline.

[e] Residues not fit by any model.

[f] There are eight pairs of residues with serious overlap: (Val42, His60), (Gly45, Thr64), (Lys46, Ala81), (Lys80, Ile98), (Glu86, Asp117), (Gly87, Gly106), (Asp107, Arg126), and (Ile109, Arg122). One residue from each pair was selected for the dynamics calculation.

[g] Resolved resonances that were too weak to measure accurate intensities.

Table 6.2 Mean order parameters for various dynamical models in LFABPs.

Table 6.3 Mean order parameters for various secondary structural elements in LFABPs.

Table 6.2

HOLO-LFABP		
Model	Number of spin[a]	Mean S^{2}[b]
Model_1	36	0.891±0.009
Model_2	8	0.844±0.010
Model_3	38	0.868±0.015
Model_4	21	0.820±0.014
Model_5	3	0.806±0.024

[a] A total spins used for calculation are 105 for apo-LFABP and 112 for holo-LFABP.
[b] $S^2 = S_s^2 S_f^2$, as described in the text.

Table 6.3

HOLO-LFABP			
2°[a]	Sequence	Number[b]	Mean S^2
βA	5-13	9	0.866±0.009
αI	14-23	6	0.918±0.017
αII	25-34	9	0.870±0.009
βB	38-43	6	0.886±0.014
βC	46-53	6	0.862±0.015
βD	57-64	7	0.877±0.010
βE	69-73	5	0.841±0.009
βF	78-85	6	0.860±0.014
βG	89-95	7	0.868±0.015
βH	98-103	6	0.886±0.012
βI	108-115	7	0.868±0.012
βJ	118-125	7	0.872±0.010

[a] Secondary structure (2°) for both apo- and holo-LFABP was derived from sequential assignments by CSI[66].
[b] Number of spins in each element of secondary structure for which relaxation results were obtained.

CHAPTER 7

OVERALL DISCUSSION AND CONCLUSIONS

- *Secondary structures*

The observation of 10 β-strands (βA-βJ) and two α-helices inserted between βA and βB is a common feature that is preserved in the following comparisons: (1) oleate-bound holo-LFABP: solution state vs. solid state; (2) LFABP in solution state: apo vs. holo; and (3) FABPs in solution and solid state: LFABP vs. other FABPs. The details are discussed in the following paragraphs. Although the comparisons below rely on chemical shift indices (CSI)[66], the elements of the secondary structure agree well with those determined by NOEs except at the ends of the secondary structural elements. Uncertainties of this nature[70] are a common feature of secondary structure determination and may reflect a current lack of consensus on the precise location of these structural elements, rather than an error in the determination or a real difference between the CSI and NOEs.

(1) Comparing the secondary structural elements of oleate-bound holo-LFABP determined by NMR (CSI) and X-ray[25] methods (**Table 5.5**), βA, βD, and βI strands show good consistency. Each of the elements αI, αII, βE, and βG is 1-3 residues longer than found by X-ray methods; βB, βF, βH, and βJ are one or two residues shorter, and βC is one residue ahead in the protein sequence. Thus, the results from both methods are in substantial agreement. Moreover, the X-ray results suggest that there is a loop within the βF strand, which is a unique property of LFABP within the FABP family. The fact that

βF consists of two β-strand segments may reflect the constraints of its hydrogen-bonding interactions with βE and βG. Our H_2O/D_2O exchange results (**Fig. 3.7 (b)**) show that some residues within the βF strand (coded in red) experience fast exchange with solvent, supporting the X-ray data and indicating that the additional βF strand is also characteristic of the solution state of holo-LFABP.

(2) Comparing the secondary structural elements of apo-[72] and holo-LFABP derived from the consensus $^{1}H/^{13}C$ chemical shift indices (CSI, see **Table 5.5**), βD, βG, and βJ strands show good consistency. The βB, βF, and βH strands in the apo-protein are 1-2 residues longer than in the holo form; βA, αI, αII, βC, and βI in the apo-protein are 1-3 residues shorter than in the holo form; and βE of the apo is two residues ahead. Thus, based on the similarities of the secondary structures on both apo and holo forms of the protein and the fact that residues Lys^{78}, Lys^{80}, and Val^{82} of the βF-strand exhibit fast exchange with solvent (**Fig. 3.4**), it is reasonable to conclude that apo-LFABP also contains a loop within the βF-strand.

(3) Comparing the secondary structural elements of rat LFABP with rat IFABP[22,70] and bovine HFABP[24] derived from chemical shift indices, the βF-strand is the longest and βE-strand is the shortest among the 10 β-strands for both proteins. However, only LFABP is reported to have a loop within the βF-strand[25], which is supported by our H_2O/D_2O NMR study since Lys^{78}, Lys^{80}, and Val^{82} have fast exchange with solvent although they are located within the βF-strand (residues 76-86) (Section 3.4.1).

By looking at the hydrogen-bonding network (**Fig. 5.9**), it is possible to see a gap between β-strands D and E, which is also a common feature in the iLBP (intracellular

lipid-binding protein) family. It is believed[115] that the separation between βD and βE is not large enough to provide access to the ligand-binding cavity in spite of its lack of interstrand hydrogen bonds. There are several water molecules forming bridges between backbone atoms in βD and βE strands, and the remainder of the space between these two strands is filled with amino acid side-chains. Even though the amino acid sequences of the βD-βE turn compared for all family members are identified as the consensus sequence –Phe-Xxx-Xxx-Gly-Xxx-Xxx-Phe/Cys- (in the case of LFABP, this corresponds to the sequence –Phe^{63}-Thr-Leu-Gly^{66}-Glu-Glu-Cys^{69}), it is not clear how this structural feature pushes βD and βE apart. Hence neither the structural nor functional bases of the gap are known despite the fact that it is present in all of the iLBPs. Other than the loop in the βF-strand, considerations of secondary structure provide no clues to the functional anomalies exhibited by LFABP.

- *Solvent accessibility and stability of the secondary structural elements.*

H_2O/D_2O exchange results show the unusual solvent accessibility of apo-LFABP within the FABP family. There are fewer than 20% remaining amide proton signals 47 min after D_2O addition. The observation of 33 doubled amide backbone resonances (HN) on apo-LFABP indicates its multiple conformations, and its incomplete resonance assignments compared with holo-LFABP suggest its high flexibility in the absence of ligands. The hydrogen bonding network comprised by the secondary structural elements is strengthened by the presence of the fatty acid ligand, as evidenced by two observations: (1) most proton amide signals disappear rapidly in the apo-protein but not

in the holo-protein; (2) amide signals remain for 24 hours after the addition of D_2O exclusively for the holo-protein (Section 3.4.4).

It should be noted that there are 15 missing amide resonances at 30 °C in H_2O for the apo-protein (but not for the holo form, see Section 4.5.3). In general, these residues are located either at the termini of LFABP's secondary structural elements (V38, S39, I109, and T110) or in loops (βC-βD turn: I52, T53, and Y54; βE-βF turn: T73 and M74; and βH-βI turn: G106). Thus, these amide protons are more likely to be solvent-exposed and not involved in intramolecular hydrogen bonds, i.e., their locations are consistent with the hypothesis that they are unobservable because of fast exchange with solvent. Similarly, amide hydrogen exchange measurements by saturation transfer on apo-IFABP and palmitate-bound holo-IFABP[27] decreased protection from hydrogen exchange in the absence of fatty acid, especially in the region of α-helix II, the α-II/β-B linker, and the βC-βD and βE-βF turns. Among these regions of high solvent accessibility are the α-II/β-B linker, βC-βD and βE-βF turns, considered to be a "portal" region that facilitates the entry and exit of the ligand from all iLBPs. LFABP appears to be unique in exhibiting substantial solvent accessibility at the βH–βI turn.

- *Tertiary structures*

The overall structures of the FABPs display a striking similarity[17,21-25]: 10 antiparallel β-strands that form two nearly orthogonal β-sheets of five strands each (a β-clam or β-barrel), and two short α-helices that connect β-strands A and B. However, the LFABP structure in solid state may exhibit a second portal at the βG-βH turn,[25] possibly

because both βG and βH in LFABP are two residues shorter than the average for the iLBP family.

The three-dimensional solution-state structure of oleate-bound holo-LFABP is well determined by NMR and exhibits the expected β-clam structural motif (**Fig. 5.14**). However, some regions show unusually high backbone RMS deviations (**Fig. 5.13** (b)): the C- and N- termini, αI helix, and turns βC-βD, βE-βF, βF-βG, βG-βH, βH-βI, and βI-βJ. Compared with the tertiary structure of holo-LFABP derived from X-ray data[25], the disordered regions at turns βF-βG, βH-βI, and βI-βJ are unique characteristics of holo-LFABP in the solution state. A recent NMR structure for palmitate-bound holo-IFABP[81] shows high backbone RMSD located at αI helix, and turns βB-βC, βE-βF, βF-βG, βG-βH, and βI-βJ. Comparing the two holo forms of LFABP and IFABP in solution, LFABP uniquely exhibits high disorder at βH-βI, where high solvent accessibility was noted above.

A structural comparison of apo- and holo-LFABP is as yet unavailable, since neither crystal nor solution structures of the apo form have been determined. However, an apo-LFABP structure is essential to provide a sound molecular basis for the nature of its ligand-protein recognition phenomena.

- *Ligand binding cavity*

The β-barrel structural feature of the iLBP family makes possible a large interior cavity suitable for binding hydrophobic ligands.[115] The bottom of the cavity is close to the center of the protein molecule and the top is near helix αII and the turns between βC and βD, βE and βF. The cavity is more or less solvent inaccessible (as verified by our

H_2O/D_2O exchange data, see **Fig. 3.7**) and considered to be the ligand-binding site in the iLBPs.

However, prior ^{13}C NMR results on oleate bound to LFABP[16] show that the carboxylate group (^{13}COO) of the fatty acid has a normal pK and is therefore believed to be exposed to the solvent. More recent X-ray results[25] demonstrate that at least two fatty acid molecules are bound within the central cavity. At the primary binding site, one FA has its carboxylate group interacting with R122 (shielded from free solvent) and a U-shaped hydrocarbon chain. At the secondary binding site, the FA has a more solvent-exposed carboxylate group located near the helix-turn-helix that caps one end of the β-barrel and its acyl chain lying in the interior.

Based on our NMR titration studies, the analyses of amide chemical shifts and HN linewidths in the protein show there are at least two fatty acid molecules bound to LFABP, with the additional possibility of a third bound FA (Section 4.2). Moreover, the analyses of α-CH_2, ω-CH_3, and ^{13}COO chemical shifts for palmitate and oleate confirm that there are at least two fatty acid molecules bound to LFABP (Sections 4.3 and 4.4).

Since the X-ray results[25] show that the two carboxylate groups are oriented in quite different environments in the holo-protein, why should their ^{13}COO chemical shifts be so similar? One explanation is that structured water molecules surround both carboxylate groups. Those structured water molecules could create similar local hydrophilic environments in the protein. Even though the whole ligand-binding cavity is very hydrophobic, the structured water molecules could create a partially hydrophilic environment in the vicinity of the carboxylate group. As mentioned above, structured water molecules also form a bridge between β-strands D and E. Based on the X-ray

study[25], the two oleate molecules do not completely fill the binding cavity of LFABP. This leaves room for six bound solvent molecules. The waters are involved in hydrogen-bond networks with the interior hydrophilic residues and the carboxyl oxygen atoms of the oleate molecules. Therefore, these waters may play an additional structural role for LFABP.

The interactions of structured water with fatty acids bound to FABPs also have precedent based on an NMR study of bovine HFABP[117]. A total of 23 contacts were detected between internal bound water molecules and the backbone amide protons of holo-HFABP. The fatty acid ligand is bound in a U-shaped conformation, and 13 water molecules are found within the binding cavity. Two of these water molecules interact with the carboxylate group of the fatty acid (only one palmitate molecule is bound to HFABP). The lifetime of these water molecules is thought to be > 1 ns, because otherwise they could not be detected by NMR.

Another explanation for the observation of a nearly unique ^{13}COO shift, which need not conflict with the first one, invokes chemical exchange between the two bound oleate molecules. Consider two bound oleates, one with its ^{13}COO on the surface (hydrophilic, OLA 128) and the other with its ^{13}COO buried in the binding cavity (hydrophobic, OLA 129). The ^{13}C chemical shift differences ($\Delta\delta$) between OLA128 and OLA129 are 0.2 ppm for the $^{13}\underline{C}OO$ group, 0.6 ppm for α-$\underline{C}H_2$, and 0.3 ppm for ω-$\underline{C}H_3$, respectively (**Fig. 4.8**). If there is exchange between the two bound oleates, the upper limit of this rate can be estimated from the observable chemical shift differences ($\Delta\delta$ * resonance frequency of ^{13}C * (2π)), i.e. 188, 565, and 283 s^{-1}, respectively for the above 3 resonances. Using proton-detected ^{13}C exchange spectroscopy on [U-^{13}C]-oleate bound

to ^{15}N-LFABP, ligand exchange between the two distinct binding environments has been found to occur at a rate of 30-40 s^{-1} at 27 °C in solution (Kroenke et al., unpublished). Thus two sets of resonances are expected and found for oleate-bound holo-LFABP. For palmitate-bound holo-LFABP (**Fig. 4.6**), only a single ^{13}COO resonance at 185.0 ppm is observed. In this latter case, either the exchange rate must be several times larger than for oleate or the chemical shifts are comparable due to the effect of structured water.

It is important to note that the side-chain ^{13}COO shifts in amino acids (there are 13 Glu and 5 Asp in LFABP) are 182.8-184.0 ppm for Glu (-CH_2CH_2COO) and 179.7-180.8 ppm for Asp (-CH_2COO) in oleate-bound holo-LFABP (**Table 5.2**). This narrow range of ^{13}COO shifts makes it plausible that two bound oleates have very similar ^{13}COO shifts (184.1 and 184.3 ppm) and two bound palmitates have a single ^{13}COO shift (185.0 ppm).

- *Protein-ligand binding site (s)*

Comparing the apo- and holo-proteins, there are several types of NMR-based evidence for the protein-ligand binding site(s) as viewed by the protein: location of residues with largest chemical shift changes, missing amide resonances in the apo form, highly solvent accessible residues in apo, disordered regions in apo, and intermolecular NOEs between protein and ligand.

Our chemical shift comparison between apo- and holo-LFABP (Section 5.5.3) shows that residues with the largest chemical shift changes are located at the end of the second α-helix (G32), the αII-βB turn (G37), the βC-βD turn (K57), and the βE-βF turn (T75). H_2O/D_2O exchange results suggest that the hydrogen-bonding network is

strengthened upon ligation at residues G32, I59 (located at the βC-βD turn), and T102 (located at the βG-βH turn) (**Table 3.1**). Moreover, 15 missing backbone amide resonances in apo-LFABP (but not in the holo form) involve turns βC-βD (I52, T53, the Y54), βE-βF (T73 and M74), and βH-βI (G106). A recent review of FABP X-ray structures[118] notes that for oleate-bound holo-LFABP, 7 of these 15 residues form the binding cavity with their sidechains, and the others interact with amino acids within the cavity. One notable residue is R122, which interacts with the carboxylate of the fatty acid in the primary binding site (OLA129). Notably, 13 of these 15 amino acids are residues with low B-factors in the holo protein crystal structure, which means that many of these residues are sufficiently buried in holo-LFABP. Thus, it seems that a significant stabilization of the protein structure occurs upon ligand binding, which supports our H_2O/D_2O exchange results on both apo- and holo- proteins (Chapter 3) and the LFABP titration study (Chapter 4). Provisional analysis of backbone dynamics indicates that the most disordered region in apo-LFABP involves residue I59 (located near the beginning of the βD-strand): it has the lowest S^2 value in the apo-protein ($S^2 = 0.260$) and a high S^2 value in the holo form ($S^2 = 0.907$). Finally, the intermolecular NOE assignments (**Table 5.6**) show that some residues with interaction to either bound oleate are located at turns αII-βB (L24), βC-βD (Y54), βE-βF (T73, V83), and βG-βH (F95, I98). Taken together, these NMR observations suggest that the LFABP-oleate binding cavity involves not only turns αII-βB, βC-βD, and βE-βF as for other FABPs, but also the βG-βH turn, supporting the X-ray results[25] which suggests a second portal may exist in LFABP. For instance, palmitate interacts with HFABP at the αI and αII helices and strands βB, βC,

and βI[24]. Palmitate binding to rat IFABP involves αII and both βC-βD and βE-βF turns[81].

- *Significance of structural and dynamic results for LFABP function*

It is appropriate to return to the questions we addressed in Section 1.3: how might the structural and dynamic information on LFABP account for its unusual binding attributes and unique transfer properties? At the end of the story, the answers to the question lie in our NMR evidence presented in Chapters 2 to 6.

Our NMR-based study supports the conclusion that LFABP binds diverse ligands relative to other FABPs and has more than one binding site. From our titration study (Chapter 4), we concluded that LFABP binds both palmitate and oleate. Not only that, LFABP also binds EPA (eicosapentaenoic acid, Liu et al., unpublished). In all three cases, large chemical shift perturbations at the αII-helix (G32), βC- βD turn (K57), and βE-βF turn (T75) suggest the high-affinity binding of all three FA ligands at similar protein sites. The titration study for palmitate and oleate also shows that LFABP binds at least two fatty acid molecules. The intermolecular NOE analysis directly shows the presence of two interaction sites on the protein (see **Fig. 5.17**): one involves a U-shaped bound oleate (OLA129, see residues in red) and the other involves an extended OLA128 molecule (see residues in blue).

What structural features account for these unusual binding characteristics? The observation that all of the iLBPs have the same general supersecondary structure emphasizes the idea that the diverse binding properties of these proteins are attributable to subtle differences in their molecular structures. In summary, although the identity of

the primary structure throughout the iLBP family varies from 20-70%, the β-barrel framework of LFABP is very similar to the other iLBP family members. However, using the crystallographic coordinates[119], the solvent accessible volume of the ligand inding cavity in LFABP is estimated to be 610 $Å^3$, as compared to 353 $Å^3$ in IFABP. In fact, the LFABP cavity is the largest of 10 family members whose structures are known. Because the cavity is larger, two oleate molecules can bind rather than one. A significant increase in cavity volume results from just a few amino acid changes that occur for residues lining the binding site. Here, both βG and βH in LFABP are two residues shorter than the average for the iLBP family. On the other hand, large chemical exchange terms (R_{ex}, Chapter 6) and significant backbone variability (Chapter 6) in the βG-βH region indicate that the possibility of a second, dynamic portal that regulates the entry and exit of fatty acid.

LFABP also has unique FA transport properties compared with other FABPs. Transfer of FA from LFABP occurs via aqueous diffusion rather than direct collisional interactions. Several types of NMR results can help to understand this phenomenon. First, our H_2O/D_2O exchange results show the extremely high solvent accessibility of apo-LFABP within the FABP family (Chapter 3). Secondly, a comparison of our dynamics results on oleate-bound holo-LFABP with palmitate-bound holo-IFABP[27] shows 59 of 112 LFABP residues with significant exchange terms but 28 of 106 IFABP residues with R_{ex} terms. These observations are consistent with the fact that transfer of FA may not need direct collisional interaction, but instead the transfer may rely on the aqueous solution as a transfer medium. Even with the addition of eight equivalents of oleate, the portal regions in LFABP exhibit substantial exchange behavior (Section 6.5).

A possible explanation is that the larger binding cavity in LFABP facilitates exchange between the two bound ligands, and between the bound and unbound ligands. The larger binding cavity and the possible second portal region (turn βG-βH) could contribute to the protein's unique FA transport functions within the FABP family.

Additional structural information on apo-LFABP is needed to fully understand the protein-ligand interaction and fatty acid targeting. This crucial piece of the LFABP puzzle is left to future investigators in our laboratory.

Reference

1) Burnett, D.A.; Lysenko, N.; Manning, J.A.; Ockner, R.K. *Gastroenterology* **1979**, *77*, 241-249.

2) Sacchettini, J.C.; Gordon, J.I.; Banaszak, L. *J .Mol.Biol.* **1989**, *208*, 327-339.

3) Sacchettini, J.C.; Gordon, J.I.; Banaszak, L. *Proc Natl Acad Sci USA* **1989**, *86*, 7736-7740.

4) Roberts, G.C.K. *NMR of Macromolecules, A Practical Approach* **1993**.

5) Wuthrich, K. *NMR of Proteins and Nucleic Acids* **1986**.

6) Markley, J.L.; Opella, S.J. *Biological NMR Spectroscopy* **1997**.

7) Reid, D.G. *Protein NMR Techniques* **1997**.

8) Saunders, M.; Wishnia, A.; Kirkwood, J.G. *J.Am.Chem Soc.* **1957**, *79*, 3289-3295.

9) Jardetzky, O.; Jardetzky, C.D. *J.Am.Chem Soc.* **1957**, *79*, 5322-5329.

10) Jardetzky, O.; Jardetzky, C.D. *J.Biol.Chem* **1958**, *233*, 383-388.

11) Bass, N.M. *Intl.Review Cytol.* **1988**, *3*, 143-184.

12) Storch, J. *Mol.Cell.Biochem.* **1993**, *123*, 45-53.

13) Lowe, J.B.; Sacchettini, J.C.; Laposata, M.; McQuillan, J.J.; Gordon, J.I. *J.Biol.Chem* **1987**, *262*, 5931-5937.

14) Storch, J.; Bass, N.M.; Kleinfeld, A.M. *J.Biol.Chem* **1989**, *264*, 8708-8713.

15) Nemecz, G.; Jefferson, J.R.; Schroeder, F. *J.Biol.Chem* **1991**, *266*, 17112-17123.

16) Cistola, D.P.; Sacchettini, J.C.; Banaszak, L.J.; Walsh, M.T.; Gordon, J.I. *J Biol Chem* **1989**, *264*, 2700-2710.

17) Sacchettini, J.C.; Gordon, J.I.; Banaszak, L. *J Mol Biol* **1989**, *208*, 327-339.

18) Hsu, K.T.; Storch, J. *J Biol Chem* **1996**, *271*, 13317-13323.

19) Kim, K.; Storch, J. *J.Biol.Chem* **1992**, *267*, 20051-20056.

20) Kim, H.K.; Storch, J. *J.Biol.Chem* **1992**, *267*, 77-82.

21) Scapin, G.; Gordon, J.I.; Sacchettini, J.C. *J.Biol.Chem* **1992**, *267*, 4253-4269.

22) Hodsdon, M.E.; Cistola, D.P. *Biochem* **1997**, *36*, 1450-1460.

23) Winter, N.S.; Bratt, J.M.; Banaszak, L.J. *J.Mol.Biol* **1993**, *230*, 1247-1259.

24) Lassen, D.; Lucke, C.; Kveder, M.; Mesgarzadeh, A.; Schmidt, J.M.; Specht, B.; Lezius, A.; Spener, F.; Ruterjans, H. *Eur J Biochem* **1995**, *230*, 266-280.

25) Thompson, J.; Winters, N.; Terwey, D.; Bratt, J.; Banaszak, L. *J Biol Chem* **1997**, *272*, 7140-7150.

26) Abragam, A. *Principles of Nuclear Magnetism* **1961**.

27) Hodsdon, M.E.; Cistola, D.P. *Biochem* **1997**, *36*, 2278-2290.

28) Zhu, L.; Kurian, E.; Prendergast, F.G.; Kemple, M.D. *Biochem* **1999**, *38*, 1554-1561.

29) Herr, F.M.; Matarese, V.; Bernlohr, D.A.; Storch, J. *Biochem* **1995**, *34*, 11840-11845.

30) Lowry, O.H.; Rosenbrough, N.J.; Farr, A.L.; Randall, R.J. *J.Biol.Chem* **1951**, *193*, 265-278.

31) Ohnishi, S.T.; Barr, J.K. *Anal.Biochem.* **1978**, *86*, 193-200.

32) Wishart, D.S.; Bigam, C.G.; Yao, J.; Abildgaard, F.; Dyson, H.J.; Oldfield, E.; Markley, J.L.; Sykes, B.D. *J.Biomolec.NMR* **1995**, *6*, 135-140.

33) Cavanagh, J.; Fairbrother, W.J.; Palmer, A.G.; Skelton, N.J.*Protein NMR* **1996**.

34) Kay, L.E.; Keifer, P.; Saarinen, T. *J.Am.Chem Soc.* **1992**, *114*, 10663-10665.

35) Cavanagh, J.; Rance, M. *Annu.Rep.NMR Spectrosc.* **1993**, *27*, 1-58.

36) Marion, D.; Ikura, M.; Tschudin, R.; Bax, A. *J.Magn.Reson.* **1989**, *85*, 393-399.

37) Bax, A.; Ikura, M.; Kay, L.E.; Zhu, G. *J.Magn.Reson.* **1991**, *91*, 174-178.

38) Patt, S.L. *J.Magn.Reson.* **1992**, *96*, 94-102.

39) McCoy, M.A.; Mueller, L. *J.Magn.Reson.A* **1993**, *101*, 122-130.

40) Shaka, A.J.; Lee, C.J.; Pines, A. *J.Magn.Reson.* **1988**, *77*, 274-293.

41) Shaka, A.J.; Barker, P.B.; Freeman, R. *J.Magn.Reson.* **1985**, *64*, 547-552.

42) Kupce, E.; Freeman, R. *J.Magn.Reson.* **1995**, *115*, 273-276.

43) Kuboniwa, H.; Grzesiek, S.; Delaglio, F.; Bax, A. *J.Biomolec.NMR* **1994**, *4*, 871-878.

44) Kay, L.E.; Xu, G.Y.; Yamazaki, T. *J.Magn.Reson.A* **1994**, *109*, 129-133.

45) Grzesiek, S.; Bax, A. *J.Am.Chem.Soc.* **1992**, *114*, 6291-6293.

46) Muhandiram, D.R.; Kay, L.E. *J.Magn.Reson.B* **1994**, *103*, 203-216.

47) Wittekind, M.; Mueller, L. *J.Magn.Reson.B* **1993**, *101*, 201-205.

48) Kay, L.E.; Ikura, M.; Tschudin, R.; Bax, A. *J.Magn.Reson.* **1990**, *89*, 496-514.

49) Kay, L.E. *J.Am.Chem.Soc.* **1993**, *115*, 2055-2057.

50) Grzesiek, S.; Anglister, J.; Bax, A. *J.Magn.Reson.B* **1993**, *101*, 114-119.

51) Bax, A.; Clore, G.M.; Gronenborn, A.M. *J.Magn.Reson.* **1990**, *88*, 425-431.

52) Zhang, O.; Kay, L.E.; Olivier, J.P.; Forman-Kay, J.D. *J.Biomolec.NMR* **1994**, *4*, 845-858.

53) Kay, L.E.; Xu, G.Y.; Singer, A.U.; Muhandiram, D.R.; Forman-Kay, J.D. *J.Magn.Reson.B* **1993**, *101*, 333-337.

54) Palmer III, A.G.; Cavanagh, J.; Wright, P.E.; Rance, M. *J Magn Reson* **1991**, *93*, 151-170.

55) Kay, L.E.; Keifer, P.; Saarinen, T. *J.Am.Chem Soc.* **1992**, *114*, 10663-10665.

56) Grzesiek, S.; Bax, A. *J.Magn.Reson.* **1992**, *96*, 432-440.

57) Bax, A.; Freeman, R. *J.Magn.Reson.* **1981**, *44*, 542-561.

58) Logan, T.M.; Olejniczak, E.T.; Xu, R.X.; Fesik, S.W. *J Biomolec NMR* **1993**, *3*, 225-231.

59) Grzesiek, S.; Bax, A. *J.Biomolec.NMR* **1993**, *3*, 185-204.

60) Messerle, B.A.; Wider, G.; Otting, G.; Weber, C.; Wuthrich, K. *J.Magn.Reson.* **1989**, *85*, 608-613.

61) Yamazaki, T.; Forman-Kay, J.D.; Kay, L.E. *J.Am.Chem Soc.* **1993**, *115*, 11054-11055.

62) Delaglio, F.; Grzesiek, S.; Vuister, G.W.; Zhu, G.; Pfeifer, J.; Bax, A. *J.Biomolec.NMR* **1995**, *6*, 277-293.

63) Johnson, B.A.; Blevins, R.A. *J Biomolec NMR* **1994**, *4*, 603-614.

64) Ousterhout, J.K. *TCL and the TK Toolkit* **1993**.

65) Kraulis, P.J. *J.Mol.Biol* **1994**, *243*, 696-718.

66) Wishart, D.S.; Sykes, B.D. *J Biomolec NMR* **1994**, *4*, 171-180.

67) Saito, H. *Magn.Res.Chem.* **1986**, *24*, 835-845.

68) Wishart, D.S.; Richards, F.M.; Sykes, B.D. *J.Mol.Biol* **1991**, *222*, 311-333.

69) Spera, S.; Bax, A. *J.Am.Chem Soc.* **1991**, *113*, 5490-5492.

70) Hodsdon, M.E.; Toner, J.J.; Cistola, D.P. *J.Biomolec.NMR* **1995**, *6*, 198-210.

71) Rizo, J.L.Z.-P.G.L.M. *J Biomolec NMR* **1994**, *4*, 741-760.

72) Wang, H.; He, Y.; Hsu, K.T.; Magliocca, J.F.; Storch, J.; Stark, R.E. *J.Biomolec.NMR* **1998**, *12*, 197-199.

73) Andrec, M.; Hill, R.B.; Prestegard, J.H. *Protein Science* **1995**, *4*, 983-993.

74) Mori, S.; Abeygunawardana, C.; Johnson, M.O.; Zijl, P.C.M. *J Magn Res B* **1995**, *108*, 94-98.

75) Kriwacki, R.W.; Hill, R.B.; Flanagan, J.M.; Caradonna, J.P.; Prestegard, J.H. *J.Amer.Chem.Soc.* **1993**, *115*, 8907-8911.

76) Fesik, S.W.; Zuiderweg, E.R.P. *J Magn Reson* **1988**, *78*, 588-593.

77) Marion, D.; Kay, L.E.; Sparks, S.W.; Torchia, D.A.; Bax, A. *J.Am.Chem.Soc.* **1989**, *111*, 1515-1517.

78) Kay, L.E.; Marion, D.; Bax, A. *J Magn Reson* **1989**, *84*, 72-84.

79) Shinnar, M.; Elff, S.; Subramanian, H.; Leigh, J.S. *Magn.Reson.Med* **1989**, *12*, 75-80.

80) Tolman, J.R.; Chung, J.; Prestegard, J.H. *J Magn Reson* **1992**, *98*, 462-467.

81) Hodsdon, M.E.; Ponder, J.W.; Cistola, D.P. *J.Mol.Biol.* **1996**, *264*, 585-602.

82) Cistola, D.P.; Walsh, M.T.; Corey, R.P.; Hamilton, J.A.; Brecher, P. *Biochem* **1988**, *27*, 711-717.

83) Grzesiek, S.; Bax, A. *J Magn Reson* **1993**, *102B*, 103-106.

84) Smallcombe, S.H.; Patt, S.L.; Keifer, P.A. *J Magn Reson* **1995**, *A117*, 295-303.

85) Solomon, I. *Physiol Rev* **1955**, *99*, 559-565.

86) Karplus, M. *J.Am.Chem.Soc.* **1963**, *85*, 2870-2871.

87) Storch, J.; Schachter, D. *Biochem* **1984**, *23*, 1165-1169.

88) Richieri, G.V.; Ogata, R.T.; Kleinfeld, A.M. *J.Biol.Chem* **1994**, *269*, 23918-23930.

89) Rolf, B.; Oudenampsen-Krür, E.; Böhers, T.; Faergeman, N.J.; Knudsen, J.; Lezius, A.; Spener, F. *Biochim.Biophys.Acta.* **1995**, *1259*, 245-253.

90) Miller, K.R.; Cistola, D.P. *Mol.Cell.Biochem* **1993**, *123*, 29-37.

91) Ockner R.K.; Manning, J.A.; Kane, J.P. *J.Biol.Chem* **1982**, *257*, 7872-7879.

92) Zhang, F.; Lucke, C.; Baier, L.J.; Sacchettini, J.C.; Hamilton, J.A. *J.Biomolec.NMR* **1997**, *9*, 213-228.

93) Cavanagh, J.; Fairbrother, W. J.; Palmer, A. G.; Skelton, N. J. *Protein NMR Spectroscopy: Principles and Practice* **1996**.

94) Muhandiram, D.R.; Xu, G.Y.; Kay, L.E. *J Biomolec NMR* **1993**, *3*, 463-470.

95) Pascal, S.M.; Muhandiram, D.R.; Yamazaki, T.; Forman-Kay, J.D.; Kay, L.E. *J Magn Reson B* **1994**, *103*, 197-201.

96) Vuister, G.W.; Clore, G.M.; Gronenborn, A.M.; Powers, R. *J Magn Res B* **1993**, *101*, 210-213.

97) Guntert, P.; Mumenthaler, C.; Wuthrich, K. *J .Mol.Biol.* **1997**, *273*, 283-298.

98) Guntert, P.; Qian, Y.Q.; Otting, G.; Mür, M.; Gehring, W.; Wuthrich, K. *J.Mol.Biol* **1991**, *217*, 531-540.

99) Guntert, P.; Braun, W.; Wuthrich, K. *J.Mol.Biol.* **1991**, *217*, 517-530.

100) Koradi, R.; Billeter, M.; Wuthrich, K. *J.Mol.Graph* **1996**, *14*, 51-55.

101) Hiyama, Y.; Niu, C.-H.; Silverton, J.V.; Bavoso, A.; Torchia, D.A. *J.Am.Chem.Soc.* **1988** , *110*, 2378-2383.

102) Lipari, G.; Szabo, A. *J.Am.Chem.Soc* **1982**, *104*, 4559-4570.

103) Lipari, G.; Szabo, A. *J.Am.Chem.Soc* **1982**, *104*, 4546-4559.

104) Clore, G.M.; Szabo, A.; Bax, A.; Kay, L.E.; Driscoll, P.C.; Gronenborn, A.M. *J.Am.Chem.Soc.* **1990**, *112*, 4989-4991.

105) Kroenke, C.D.; Loria, J.P.; Lee, L.K.; Rance, M.; Palmer, A.G. *J.Am.Chem.Soc.* **1998**, *120*, 7905-7915.

106) Freedberg, D.I.; Wang, Y.; Stahl, S.J.; Kaufman, J.D.; Wingfield, P.T.; Kiso, Y.; Torchia, D.A. *J.Am.Chem.Soc.* **1998**, *120*, 7916-7923.

107) Palmer, A.G.; Rance, M.; Wright, P.E. *J.Am.Chem.Soc.* **1991**, *113* , 4371-4380.

108) Mandel, A.M.; Akke, M.; Palmer, A.G. *J.Mol.Biol.* **1995**, *246*, 144-163.

109) Press, W.H.; Flannery, B.P.; Teukolsky, S.A.; Vetterling, W.T. *Numerical Recipes The Art of Scientific Computing* **1986**.

110) Devore, J.L. *Probability and Statistics for Engineering and the Sciences* **1982**.

111) Farrow, N.A.; Muhandiram, R.; Singer, A.U.; Pascal, S.M.; Kay, C.M.; Gish, G.; Shoelson, S.E.; Pawson, T.; Forman-Kay, J.D.; Kay, L.E. *Biochem* **1994**, *33*, 5984-6003.

112) Markley, J.L.; Horsley, W.J.; Klein, M.P. *J.Chem.Phys* **1971**, *55*, 3604-3609.

113) Bruschweiler, R.; Liao, X.; Wright, P.E. *Science* **1995**, *268*, 886-889.

114) Tjandra, N.; Feller, S.E.; Pastor, R.W.; Bax, A. *J.Am.Chem.Soc* **1995**, *117*, 12562-12566.

115) Banaszak, L.; Winter, N.; Xu, Z.; Bernlohr, D. A.; Cowan, S.; Jones, T. A. *Advances in Protein Chemistry* **1994**, 90-151.

116) Herr, F. M.; Aronson, J.; Storch, J. *Biochem* **1996**, *35*, 1296-1303.

117) Mesgarzadeh, A.; Pferffer, S.; Engelke, J.; Lassen, D.; Ruterjans, H. *Eur Biophys J.* **1998**, *251*, 781-786.

118) Thompson, J.; Reese-Wagoner, A.; Banaszak, L. *Biochi Biophy Acta* **1999**, *1441*, 117-130.

119) Thompson, J.; Ory, J.; Reese-Wagoner, A.; Banaszak, L. *Molecular and Cellular Biochemistry* **1999**, *192*, 9-16.